Journal of Volcanology and Geothermal Research 432 (2022) 107701

Contents lists available at ScienceDirect

Journal of Volcanology and Geothermal Research

journal homepage: www.journals.elsevier.com/journal-of-volcanology-and-geothermal-research

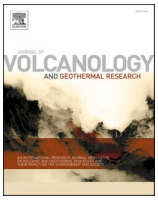

Emplacement and impacts of lava flows and intrusions on the sediment-buried Escanaba Segment of the Gorda mid-ocean ridge

David A. Clague [a,*], Robert A. Zierenberg [b], Jennifer B. Paduan [a], David W. Caress [a], Brian L. Cousens [c], Brian M. Dreyer [d], Alice S. Davis [a], James McClain [b], Stephanie L. Ross [e]

[a] Monterey Bay Aquarium Research Institute, Moss Landing, CA 95039, United States of America
[b] Department of Earth and Planetary Sciences, University of California Davis, Davis, CA 95616, United States of America
[c] Ottawa-Carleton Geoscience Centre, Earth Sciences, Carlton University, Ottawa, Ontario K1S 5B6, Canada
[d] Earth and Marine Sciences, University of California at Santa Cruz, Santa Cruz, CA 95064, United States of America
[e] U.S. Geological Survey, Moffett Field, CA 94035, United States of America

ARTICLE INFO

Keywords:
Sills
Laccoliths
Lava flows
Hydrothermal deposits
Pockmarks
Gorda Ridge

ABSTRACT

The Escanaba Segment, the southernmost of the Gorda mid-ocean ridge segments, contains thick sandy to silty turbidite deposits that are Pleistocene to Recent in age. Dozens of deep laccoliths and shallower sills intrude into these sediments. The intrusions uplifted hills of the unconsolidated turbidites and some fed surface lava flows supplied along steeply dipping reverse faults that surround some of the tallest uplifted hills. Multibeam bathymetric mapping at 1-m resolution and chirp subbottom profile (SBP) lines at ~150 m spacing show that the uplifted sediment hills have complex patterns of surface deformation and experienced debris avalanche landslides on over-steepened slopes formed by uplift along reverse faults. The uplifted hills are spatially associated with 262 hydrothermal chimneys that are several-m-tall and abundant at two main areas named NESCA and SESCA (for northern and southern Escanaba). Chimneys are more abundant and widespread than previously mapped. The uplifted hills are also spatially associated with over 600 previously unrecognized pockmarks that range from a few to over 100 m in diameter and are up to 24 m deep. The hydrothermal deposits and pockmarks are associated with oily sediment, oily sulfide deposits, and tar mounds on the seafloor. The intrusions provide the heat to mature hydrocarbons from organic carbon in the sediment and to drive hydrothermal circulation that deposits sulfides and sulfates on the seafloor, mostly surrounding the tallest hills overlying thick laccoliths. The frequency sweep (chirp) subbottom profiles show that most sills and all the laccoliths are deeper than the ~60 m penetration of the system. However, the thicknesses and depths of numerous shallow sills are mapped from the bathymetry and SBP data. The deepest intrusions are all domed or punched laccoliths, those of intermediate depth are thick inflated sills, and the shallowest are the thinnest sills, as determined from the height of the uplifted hills. For most intrusions, depth to the top of the intrusion is roughly 3 times the thickness of the intrusion. The dome laccolith under Central Hill, in the NESCA vent field, is the only laccolith with well-constrained thickness (from the height of the uplifted Central Hill) and depth (from ODP drill 1038H through the hill that bottomed in the upper part of the laccolith. Sediment thicknesses on top of lava flows that pre- and postdate emplacement of the laccolith that uplifted Central Hill, coupled with an average sediment accumulation rate of 17.8 cm/kyr over the past almost 8800 years indicated that active hydrothermal venting on Central Hill began before ~225 years ago (the inferred age of the NESCA Young lava flow) but after ~1685 years ago (the average inferred age of NESCA #1 lava flow).

Abbreviations: AUV, autonomous underwater vehicle; MESCA, middle Escanaba Trough; NESCA, northern Escanaba Trough; ODP, Ocean Drilling Program; ROV, remotely operated vehicle; SESCA, southern Escanaba Trough; SBP, subbottom profile; TWTT, two-way-travel-time; MORB, mid-ocean ridge basalt.

* Corresponding author.
E-mail address: clague@mbari.org (D.A. Clague).

https://doi.org/10.1016/j.jvolgeores.2022.107701
Received 2 May 2022; Received in revised form 4 October 2022; Accepted 20 October 2022
Available online 26 October 2022

1. Introduction

Intrusions are common volcanic features in the geologic record and emplacement of sills and laccoliths has been the focus of numerous studies and review articles (e.g., Hunt, 1953; Corry, 1988; Duffield et al., 1986; Galland et al., 2018). Most sills are found in sediment that has been uplifted, deformed, lithified, and exposed by erosion to reveal the sills in cross section (e.g., Hunt, 1953). A few sills have been encountered and sampled by ODP drilling on the mid-ocean ridge system during programs to sample hydrothermal deposits and their buried stockwork (Guaymas Basin in the central Gulf of California; e.g., Einsele et al., 1980; Teske et al., 2019, 2020, 2021; Middle Valley on the Juan de Fuca Ridge, Fouquet et al., 1998a; and Escanaba Segment of the Gorda Ridge; Fouquet et al., 1998a). In the Escanaba Segment, shallow intrusions were recognized as having uplifted sediment hills (Morton et al., 1994). Other deep-sea examples of hills uplifted by shallow intrusions are described in the southern Gulf of California along the Tamayo and Pescadero Transform faults (Clague et al. (2018) and in the Pescadero Basin (Paduan et al., 2018), and at the base of West Mata Volcano in the Lau Basin (Chadwick et al. (2019).

Sills and laccoliths in the Escanaba Segment intruded beneath and uplifted young sediment hills (Denlinger and Holmes, 1994), focused hydrothermal discharge (Zierenberg et al., 1993, 1994), and drove the discharge of thermally mature hydrocarbons (Kvenvolden et al., 1994). These prior studies were mainly completed in the 1980s (Morton et al., 1994) and culminated in Ocean Drilling Program (ODP) drilling in 1996 (Fouquet et al., 1998a; Zierenberg et al., 1998, 2000; Zierenberg and Miller, 2000). The young age of the host sediment, and therefore of the sills, indicates that the observed sediment deformation is caused almost entirely by intrusive processes with only minor extension across the spreading mid-ocean ridge axis, in contrast to more complex tectonic processes that expose sills on land. Sediment hills uplifted by intrusions are observed in map view as variations in topography with extensional crack networks imaged in high-resolution bathymetry, as reflectors imaged in shallow subbottom profiles (SBP), or both. This map view of sediment deformation is analogous to models of sill (e.g., Bunger and Cruden, 2011; Magee et al., 2017) or laccolith emplacement (e.g., Corry, 1988; Currier et al., 2017). Intrusion results in uplift of still largely unlithified sediment hills triggering landslides on the flanks of the taller hills that modify their shape and disrupt the sediment stratigraphy and form overlying extensional crack networks and summit grabens.

In this paper, we examine the morphology and deformation of the sediment hills during and after uplift from sill and laccolith intrusions; the distribution, emplacement, and composition of associated lava flows; the distribution of hydrothermal chimneys; the depths, thicknesses, and distribution of sills imaged in SBP and inferred from uplifted sediment hills; and the distribution of hundreds of previously unknown pockmarks and their association with intrusions. These features were mapped using 1-m resolution bathymetry and a series of mainly parallel near-bottom frequency sweep (chirp) sonar SBP spaced about 150–170 m apart that image the upper 50–75 m of the sedimentary section. These new coregistered bathymetric and SBP data were collected from autonomous underwater vehicles (AUVs) and supplemented by observations and sampling during 16 remotely operated vehicle (ROV) dives. Sediment uplift and deformation, hydrothermal activity, and formation of pockmarks are integral components of shallow magma intrusion that are mostly obscured when studies are conducted on exhumed sills on land.

2. Geologic setting and previous work

The Escanaba Segment is the southernmost of five segments of the Gorda mid-ocean ridge (Chadwick Jr. et al., 1998), and is located ~275 km offshore northern California. The Gorda Ridge is bounded to the north by the Blanco Transform and to the south by the Mendocino Fracture Zone (Fig. 1A). The Segment has a full spreading rate of 24 mm/yr (Wilson, 1989). The axial graben widens from north to south from ~5 to ~15 km, is roughly at a depth of 3300 m, and is buried with up to 900 m of late Pleistocene to early Holocene sediment (Clague and Holmes, 1987; Morton and Fox, 1994) north of the Mendocino Transform. The maximum sediment thickness is ~507 m at ODP site 1037B (Zuffa et al., 2000) in the surveyed region into which sills and laccoliths described here were intruded. The sedimentary section consists of a series of turbidites (Morton et al., 1994; Fouquet et al., 1998c).

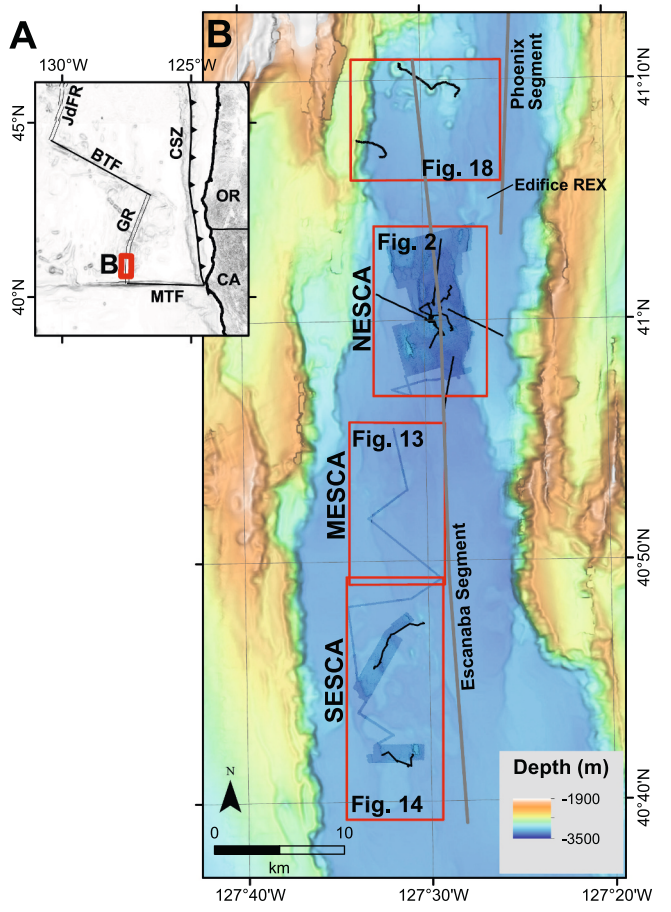

Fig. 1. A) The location of study area as red box on general location map. OR is Oregon State, CA is California State, CSZ is the Cascadia Subduction Zone, JdFR is Juan de Fuca Ridge, BTF is the Blanco Transform Fault, GR is the Gorda Ridge, and MTF is the Mendocino Transform Fault. B) Bathymetric map of Escanaba Trough with 1-m resolution AUV data on top of faded 60-m resolution EM300 data for the floor of the trough on top of regional data from NCEI. Labeled red boxes show the extent and locations of the northern Escanaba (NESCA) region (Fig. 2), the southern Escanaba (SESCA) region (Fig. 14), the middle Escanaba or MESCA region between NESCA and SESCA (Fig. 13), and of the northernmost Escanaba Segment (Fig. 18). Edifice REX (Zierenberg et al., 1998) . Dive tracks for ROV dives conducted between 2000 and 2009 are shown as black lines and the axes of the Escanaba and Phoenix Segments are gray lines. (For interpretation of the references to colour in this figure legend, the reader is referred to the web version of this article.)

The southern third of the Phoenix Segment to the north (Chadwick Jr. et al., 1998) is also sediment buried (Morton et al., 1994), whereas the northern 2/3 of the segment is a more typical bare-rock axis. The Escanaba Segment and southern third of the Phoenix Segment comprise what was collectively termed the Escanaba Trough in Morton et al. (1994). Work in the 1980s and 1990s used a wide range of techniques to study an inactive hydrothermal site named SESCA (Southern Escanaba) (Fig. 1 and Morton et al., 1994) and a nearby active hydrothermal vent field named NESCA (Northern Escanaba) (Fig. 1 and Morton et al., 1994) where fluids rise through and react (Bohlke and Shanks III, 1994;

Magenheim and Geiskes, 1994; Zierenberg and Shanks III, 1994) with sediment that partially fills the axial graben (Zuffa et al., 1997, 2000; Normark and Serra, 2001). Intrusions uplift the turbidite sediment to form hills up to 140–150 m tall (Morton et al., 1994). A deep-towed survey, executed 100–200 m above bottom, collected simultaneous 60 kHz sidescan and 4.5 kHz SBP in 1996 (Ross and Zierenberg, 2009) over the NESCA region, with partial coverage of SESCA and a third hydrothermal site called MESCA (Middle Escanaba) located on a low hill between NESCA and SESCA (Koski et al., 1994).

Magma rose through the sediment section and was emplaced as lava flows (Ross and Zierenberg, 1994, 2009) and sampled at five locations (NESCA, SESCA, Edifice REX on Fig. 1B; Davis et al., 1994) on Escanaba Segment. At NESCA, sidescan mapped an extensive, young, high-backscatter flow of T-MORB (Davis et al., 1994) and an apparently older, more sediment covered, but unsampled, lava flow. At SESCA two chemically similar T-MORB lava flows with similar sediment-cover were mapped and sampled. Ross and Zierenberg (1994, 2009) described these flows based on camera tows and observations from submersible dives and Davis et al. (1994, 1998) presented geochemistry of the lavas. Immediately north of the mapped NESCA Young flow, imagery from 4.5 kHz profiles mapped an unsampled shallow sill or flow buried by thin sediment cover (Ross and Zierenberg, 2009). The sediment surface was not recognized as being uplifted to form hills above this sill or flow. On the adjacent Phoenix Segment, 17 analyzed samples from four rock dredges included primitive N-MORB (with $K_2O/TiO_2 < 0.10$) and MgO between 8 and 9 wt%, to evolved T-MORB with $K_2O/TiO_2 > 0.135$ and MgO of ~7.1 wt% (Davis et al., 1994). An HOV *Alvin* dive sampled a flow of E-MORB with $K_2O/TiO_2 > 0.20$ (Davis et al., 1994, 1998) from Edifice REX (labeled on Fig. 1B) just north of the AUV survey area.

In 1996, the Ocean Drilling Program drilled one active, and several

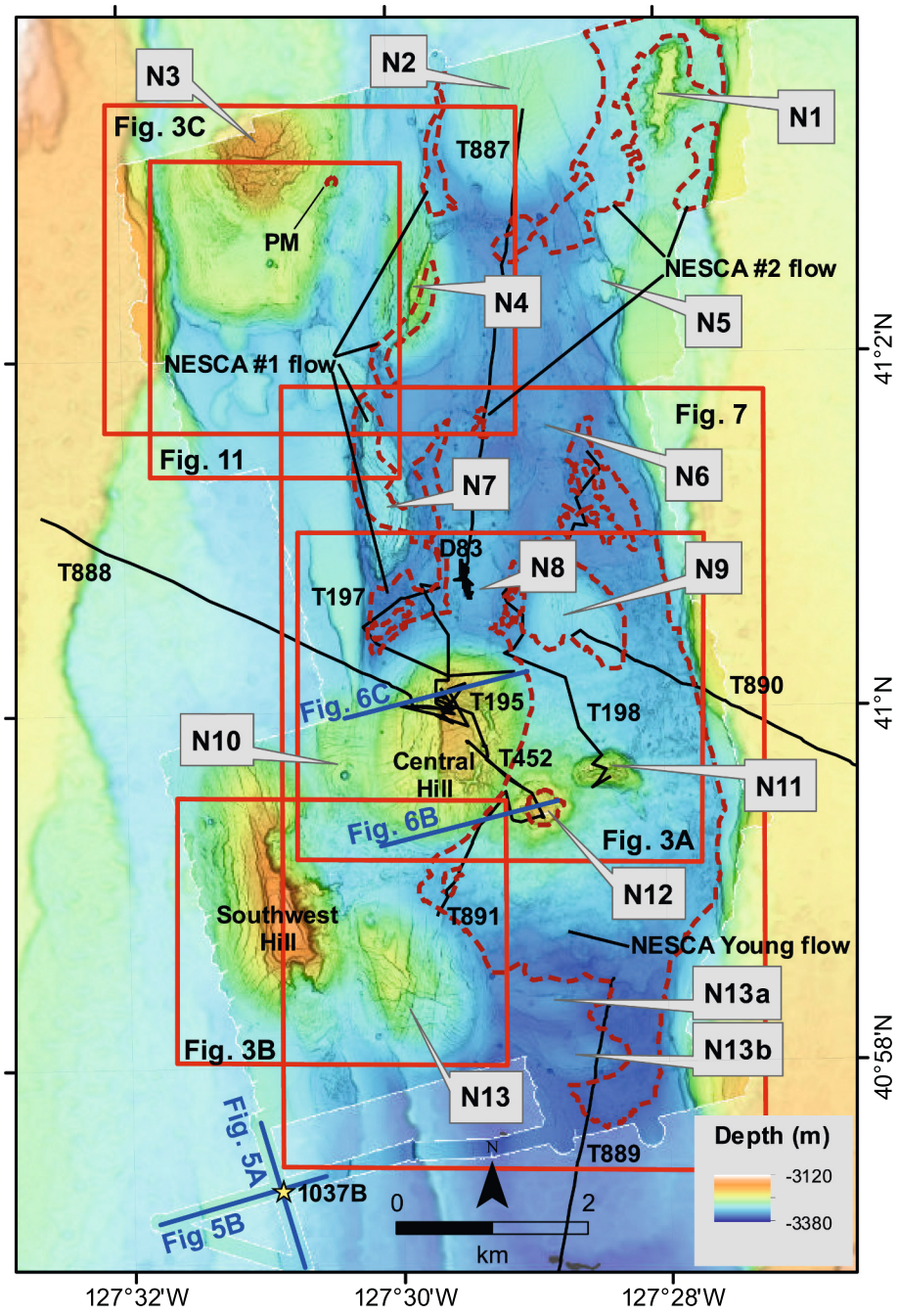

Fig. 2. NESCA AUV map on top of faded EM300 ship bathymetry showing ROV *Tiburon* labeled dive tracks T195, T197 and T198 in 2000, T449 and T452 in 2002, T897 to T891 in 2005, and ROV *Doc Ricketts* dive D83 in 2009. Dives T889 and T890 extend beyond the map to south and east, respectively (for full extent of those dives see Fig. 12 in Clague et al., 2009). Red boxes show extents of close-ups of Central Hill (Fig. 3A), Southwest Hill (Fig. 3B), and Hill N3 (Fig. 3C). ODP reference site 1037B is labeled 1037B. Chirp subbottom profiles (SBP) crossing through the ODP reference site (Fig. 5A and B) and lines crossing Central Hill (Fig. 6B and C) are shown in bold dark blue and labeled. Hills N1 to N13 (and their later lobes labeled, e.g., N13a or N13b) and Southwest and Central Hill names are used in Table 1 and the text. Red dashed lines outline labeled NESCA Young, NESCA #1, NESCA #2 lava flows and a pillow mound (PM) on Hill N3a. Red boxes show extents of Figs. 3A, B, C, 7 and 11. (For interpretation of the references to colour in this figure legend, the reader is referred to the web version of this article.)

inactive, sulfide mounds at Site 1038 on Central Hill at NESCA (Fouquet et al., 1998b) and sediment reference at Site 1037 through the fill in the axial graben south of NESCA (Fouquet et al., 1998c, and Fig. 2). Volcanic rocks were encountered and recovered in holes 1038G, 1038H, and 1038I at 135–161 m below sea floor (mbsf) and at 403 mbsf at the bottom of hole 1038I (Fig. 3A). The mid-section and basal volcanic units were interpreted as either sills or surface flows subsequently buried by sediment (Fouquet et al., 1998b) and whole-rock analyses of the volcanic rocks were sufficiently altered to make identification of the lava types uncertain. Five of the ODP drill holes were subsequently observed during ROV dives on Central Hill (Fig. 4A and B).

Reflectors, named A to I from shallowest to deepest (Fig. 5A and B), were correlated to radiocarbon-dated sediment in the upper part of ODP Site 1037B (Zuffa et al., 2000; Normark and Serra, 2001). These reflectors thin as a function of water depth, and therefore from south to north in the Escanaba axial graben (Normark and Serra, 2001). For simplicity, reflector depths reported here are the depth in meters below sea floor (mbsf) of each reflector at site 1037B with reflector A at 4 m mbsf, B at 8.5 mbsf, C at 13 mbsf, D at 19 mbsf, E at 23 mbsf, F at 32 mbsf, G at 38.5 mbsf, H at 48.5 mbsf, and I at 59 mbsf. Calibrated radiocarbon dates indicate that reflectors A to I were deposited between ~12.6 and ~8.1 calibrated kyr ago. Shallow sills intruded into these sediments must be younger than the age of the corresponding reflector.

Hydrothermal fluids sampled in 2000–2005 (von Damm et al., 2005), as part of post-drilling fieldwork (Clague et al., 2001), showed only minor changes in the hydrothermal system since pre-drilling fluid sampling in 1988 (Campbell et al., 1994).

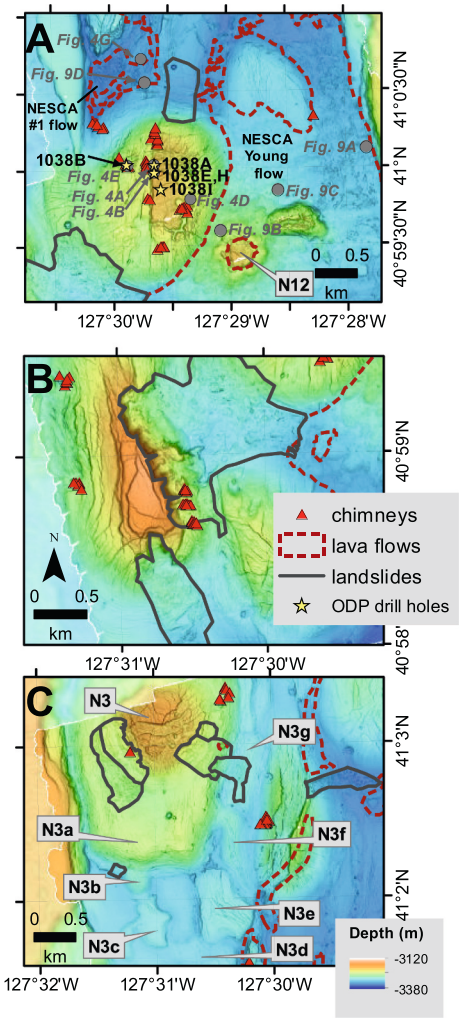

Fig. 3. NESCA AUV map enlargements of: A) Central Hill, with ODP drill sites 1038A to 1038I shown as yellow stars. Gray dots and labels locate bottom images in Figs. 4 and 9. B) Southwest Hill with two secondary landslides (outlined with solid line). The western portion of NESCA Young lava flow is outlined with dashed red lines. C) Hill N3 with distinct adjacent lobes labeled as discussed in the text and listed in Table 1. Red triangles are sulfide chimneys identified in the AUV bathymetry. (For interpretation of the references to colour in this figure legend, the reader is referred to the web version of this article.)

3. Methods

The primary data are regional-scale ship multibeam data and high-resolution (~1-m lateral and 10-cm vertical resolution) multibeam bathymetric and backscatter data and chirp SBP data collected by AUVs. Observations and sampling during 16 ROV dives complement the geophysical data.

3.1. Shipboard multibeam surveys

Escanaba Trough was mapped using SeaBeam (Morton and Fox, 1994; Chadwick Jr. et al., 1998) as part of a NOAA effort to map the entire Gorda plate (Dziak et al., 2002). In 1998, the axial graben of Escanaba and Phoenix Segments were remapped at higher resolution using a Simrad EM300 system (MBARI Mapping Team, 2001), although the >3200 m depth of the segments approached the signal/noise limits of the 30 kHz system, as configured at that time. Depths were calculated using water column sound velocities determined from CTD (conductivity, temperature, depth) casts and the survey was navigated using differential GPS, resulting in improved resolution, more accurate depths, and improved location compared with earlier survey data. Despite its collection in 1998, the Simrad EM300 survey, with resolution at the depth of the Escanaba Segment of ~100 m, remains the best regional-scale bathymetric data for most of the Gorda Ridge axis.

3.2. Acquisition of AUV multibeam and chirp subbottom surveys

The EM300 bathymetric data were used to identify uplifted hills to guide the design of AUV high-resolution surveys. High-resolution mapping within the Escanaba Trough axis occurred in 2014 and 2016 (Clague et al., 2021) using two Dorado class AUVs (Caress et al., 2008) that survey in tandem at 1.5 m/s (3 knots), with an endurance of about 17.5 h. A total of eight successful missions provide coverage of the NESCA and SESCA sites, and along a zig-zag survey line over a series of five of the six uplifted hills that comprise the middle Escanaba (MESCA) site between NESCA and SESCA, all with spatially coregistered multibeam and SBP data. The AUVs were outfitted with Reson 7125 multibeam sonar (operated at 200 kHz in 2014 and 400 kHz in 2016), Edgetech sonar package with 110 kHz chirp 1-6 kHz subbottom profiler, an Edgetech chirp subbottom profiler, a SeaBird SBE-49 fastCat CTD, and a Paroscientific pressure sensor. The SBP data were collected using a 12 millisecond 1–5 kHz swept-frequency (chirp) source pulse. The subbottom was synchronized with the multibeam, pinging at a rate of 3 Hz and collecting 300-millisecond sweep time series. The 7125 multibeam sonar generated 256 0.94° by 0.94° beams across a 135° swath, producing soundings with beam footprints with widths of 0.82 m at nadir and 1.67 m at 45° for the 50 m altitude surveys. The average lateral resolution is therefore ~1.25 m and repeatable vertical precision is 0.1 m following tidal correction. The realtime AUV navigation sensor is a Kearfott SeaDevil inertial navigation system (INS) which integrates a 24 cm ring laser gyro, accelerometers, and a 300 kHz Doppler Velocity Log (DVL) through an embedded Kalman filter. The INS is initialized by GPS at the surface and aided during descent by an ultrashort baseline (USBL) Sonardyne SM-7707 acoustic tracking system, with position fixes transmitted to the vehicle by acoustic modem. The INS has position accuracy of 0.05% distance traveled if DVL bottom lock is maintained.

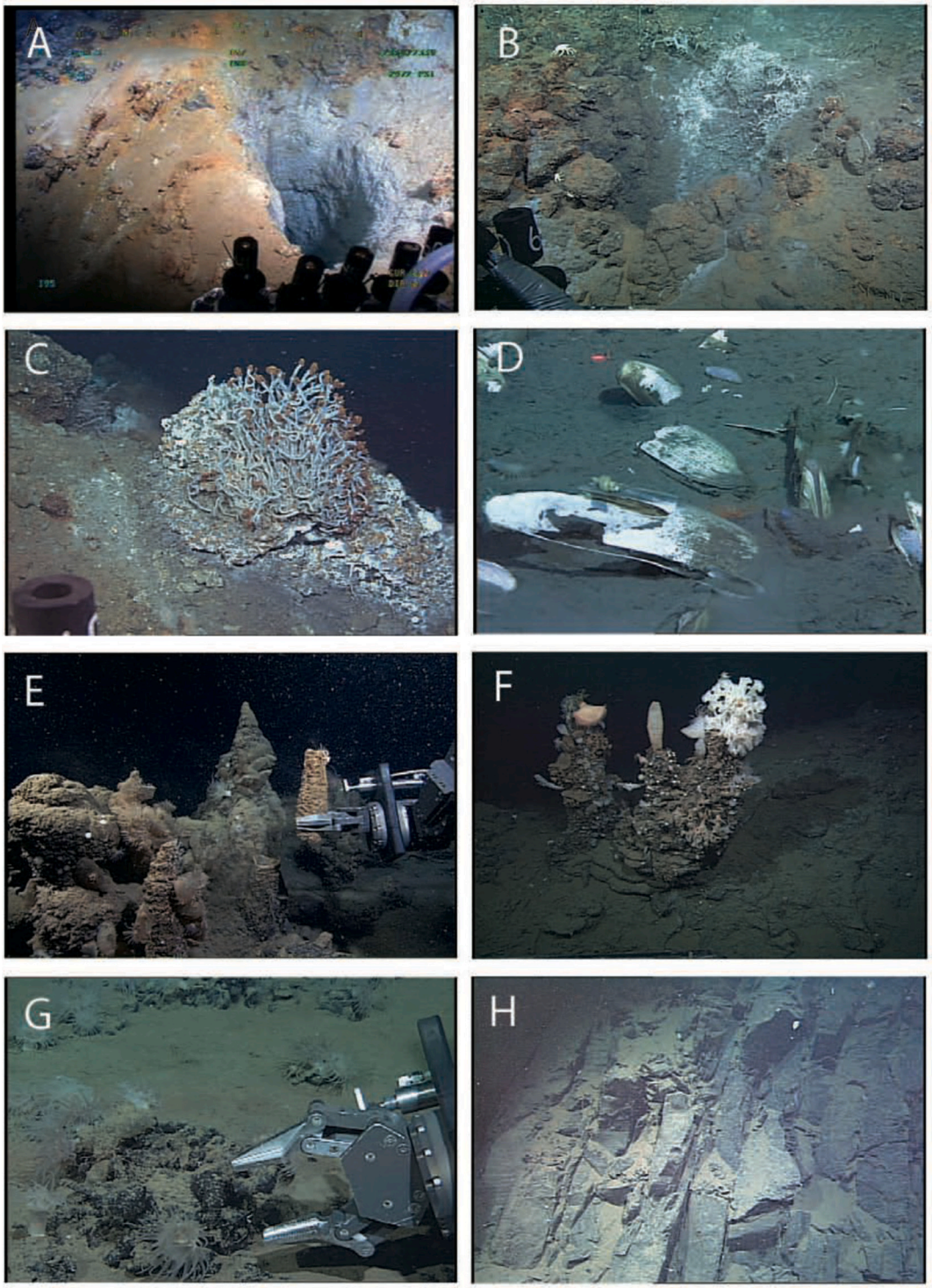

Fig. 4. Framegrabs of hydrothermal sulfide deposits, hydrothermal hydrocarbons and silica-cemented turbidites. A) ODP drill hole 1038A at NESCA in sulfide mound. Hole has minimal fluid venting. Image T195_02_19_48_24 at 3226 m depth. B) ODP drill hole 1038H at NESCA showing no venting. Hole is in sulfide. Image T195_04_37_27_04 at 3226 m depth. C) Active hydrothermal vent at NESCA with *Ridgea* tubeworms. Image T195_00_12_48_12 at 3222 m depth. D) Chemosynthetic clams indicative of diffuse hydrothermal discharge at NESCA on SE side of Central Hill. Most are dead shells, although those jutting out of the sediment are alive. Image T452_09_24_53_03 at 3236 m depth. E) Inactive sulfide and barite chimneys at NESCA near ODP drill hole 1038B. Image T195_03_18_14_23 at 3261 m depth. F) Inactive chimneys at SESCA serving as substrate for non-vent sessile community. Image T199_00_42_27_25 at 3227 m depth. G) Tar mound hosting anemones adjacent to NESCA #1 lava flow. Image T197_06_14_16_19 at site of collection of Rock 8 at 3339 m depth. H). Silica-cemented turbidites with pseudo-columnar jointing exposed in western fault bounding the axial graben north of NESCA. Image T194_03_57_41_29 at 3096 m depth. All images are roughly 5 m across except B and F which are roughly 1 m across. Locations of images are labeled on Figs. 3A, 14, and 18.

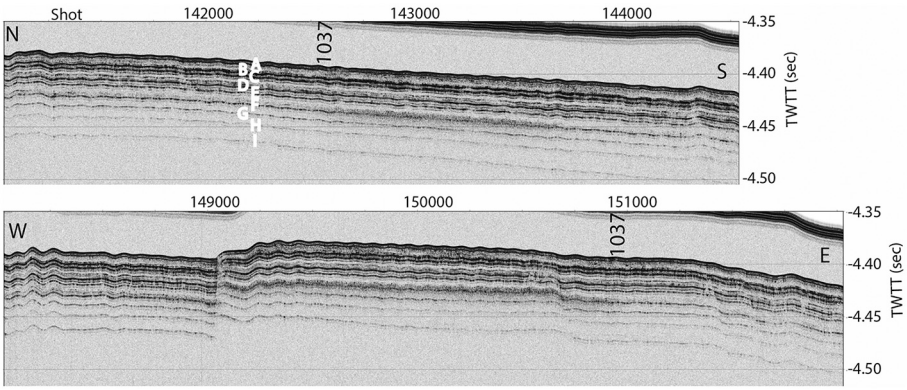

Fig. 5. Undisturbed sediment sequence in Escanaba Trough showing nine reflectors (A to I, after Normark et al., 1994). The two SBP were collected crossing at the location of ODP reference hole 1037B (labeled 1037 on each profile). The horizontal axis is in ping number since the start of the survey and 1000 pings is ~500 m; the N to S and W to E profiles are 1.6 and 1.8 km long, respectively. Reflector I is at a depth of ~60 m and is ~12.6 kyr old (in calibrated radiocarbon years, interpolated between calibrated dated horizons (Zuffa et al., 2000) of 10.69 kyr age at 21.57 mbsf and 16.43 kyr age at 121.50 mbsf). This sediment sequence occurs throughout Escanaba Segment and thins slightly from south to north so reflector depths are slightly underestimated at SESCA (south of the reference site) and overestimated at NESCA (north of the reference site). The depths of the identified reflectors at the reference hole 1037B are used for all the AUV-collected SBP data. Locations of the two lines are shown on Fig. 2 labeled as Fig. 5A and Fig. 5B.

3.3. Processing of AUV data

Multibeam data were processed using the MB-System software package (Caress and Chayes, 2011). The navigation was adjusted to match identifiable features in overlapping swaths using the MB-System tool MBnavadjust, resulting in a navigation model with relative accuracy equivalent to the survey resolution. The AUV survey data were not further adjusted to match the much lower resolution EM300 shipboard bathymetry.

The SBP were displayed for interpretation using the envelope or instantaneous amplitude function, as is common for chirp SBP sonars (Henkart, 2006; Caress, 2010) and have a nominal vertical resolution of about 0.3 m. Penetrations of up to 70 m are observed in these surveys. Reflectors identified in the subbottom profiles are referred to as A-I to correspond to the layer names from Brunner et al. (1999).

3.4. Area and volume estimates for features

The areas of some lava flows and uplifted hills were calculated using GIS from polygons surrounding the features. Volumes are difficult to determine for features older than initial surveys as a difference cannot be calculated from pre- and post-surveys, as done for historical flows (e.g., Caress et al., 2012; Yeo et al., 2013; Clague et al., 2017) and hence have greater uncertainties. Two different approaches are used depending on the type of feature. For lava flows, the average thickness is estimated and multiplied by the area to get a rough volume. For the uplifted hills, a base is estimated from depths along the polygon outlining the hill, in a manner similar to that used in Yeo et al. (2013).

3.5. Physical sampling, direct observations from ROV dives, and lava sample analyses

In 2000, 2002, and 2005, ROV dives using MBARI's ROV *Tiburon* observed and collected lava, hydrothermal chimney samples, hydrothermal fluids (von Damm et al., 2005), and 139 sediment pushcores to map dispersal of pyroclastic glass shards (Clague et al., 2009). In 2009 a single dive utilizing MBARI's ROV *Doc Ricketts* collected vent animals and hydrothermal mound samples from diffuse vents and seeps north of Central Hill and examined a large circular depression. Seven ROV dives were completed in 2000 (Clague et al., 2001), three in 2002, five in 2005, and one in 2009. At NESCA eleven samples of lava flows were also recovered using a wax-tip corer deployed from MBARI's R/V *Western Flyer* in 2000. The glass rinds on the ROV-collected and wax-tip corer basalt samples were analyzed by electron microprobe at the US Geological Survey in Menlo Park, CA, using methods and equipment described in Davis and Clague (2003); Davis et al. (1998). A glass rind on a single sample of basalt from the bottom of Site 1038I was analyzed by electron microprobe at University of California at Davis using methods and equipment described in Clague et al. (2018).

3.6. Isotopic analyses

Isotopic analyses were done at Carlton University and University of California at Santa Cruz. Between 100 and 200 mg of sample powder were weighed into a screw-cap Teflon vial, followed by dissolution in HNO_3-HF, then further attacked with HNO_3 and HCl until no residue is visible. Pb is separated from the residue, dissolved in 1 N HBr, using AG1-X8 anion resin (200–400 mesh) rinsed with 6 N HCl after elution of Sr and Nd in HBr. Sr and the bulk REE are separated sequentially by cation chromatography (Dowex 50-X8) using 2.5 N HCl and 6 N HCl, respectively. The REE-bearing residue is dissolved in 0.26 N HCl and loaded into an Eichrom chromatographic column containing Teflon powder coated with HDEHP [di(2-ethylhexyl) orthophosphoric acid; Richard et al., 1976]. Nd is eluted using 0.26 N HCl.

Sr residues were dissolved in 0.3 N H_3PO_4 and loaded onto a single Ta filament and run at 1350-1400 °C in a 9-cup Thermo-Finnigan Triton T1 thermal ionization mass spectrometer. Sr isotope ratios are normalized to $^{86}Sr/^{88}Sr = 0.11940$. Total procedural blanks are <100 pg Sr. Total procedural blanks are <100 pg Sr. The laboratory average $^{87}Sr/^{86}Sr$ for the NBS 987 Sr standard is 0.710247 $^{\pm}$ 0.000015 ($n = 30$, January 2019–August 2021). The laboratory average for USGS rock standard BCR-2 is 0.704998 +/− 0.000018 ($n = 8$, July 2019–August 2021), which agrees well with accepted values (Weis et al., 2006). All analytical uncertainties are 2-sigma standard deviations of the mean of ~90 scans.

Nd isotope ratios were determined on a Thermo-Finnigan NEPTUNE MC-ICP-MS. Nd residues were dissolved in 2% HNO_3 and an aliquot was added to a 1.5 ml centrifuge tube containing 1 ml of 2% HNO_3 to yield a final concentration of 0.2 ppm. Isotope ratios are normalized to $^{146}Nd/^{144}Nd = 0.72190$. Total procedural blanks for Nd are <100 picograms. The laboratory average $^{143}Nd/^{144}Nd$ for the JNdi-1 standard is 0.512085 +/− 0.000011 ($n = 46$, July 2019–August 2021), and all analyses have been normalized to the accepted value for the JNdi-1 standard of 0.512100 (Garcon et al., 2018). Analyses of the USGS standard BCR-2 yield Nd = 28.41 ppm, Sm = 6.53 ppm, and $^{143}Nd/^{144}Nd = 0.512626 \pm 0.000006$ ($n = 8$). All analytical uncertainties are 2-sigma standard deviations of the mean of ~90 scans.

Pb isotope ratios were determined on a Thermo-Finnigan NEPTUNE MC-ICP-MS at Carlton University. An aliquot of the Pb residue was dissolved in 1.5 ml of 2% HNO_3, and then spiked with a ^{203}Tl—^{205}Tl spike to correct for within-run fractionation. Final ratios were further corrected using values for NBS981 from Todt et al. (1996). Average Tl-

corrected values for NBS981 are: $^{206}Pb/^{204}Pb = 16.9317 +/- 0.0016$, $^{207}Pb/^{204}Pb = 15.4855 +/- 0.0019$, and $^{208}Pb/^{204}Pb = 36.6794 +/- 0.0057$ ($n = 33$; 2-sigma uncertainties). Measured ratios in international standard BCR-2 are $^{206}Pb/^{204}Pb = 18.7566 +/- 0.0009$, $^{207}Pb/^{204}Pb = 15.6128 +/- 0.0006$, and $^{208}Pb/^{204}Pb = 38.6981 +/- 0.0008$ (2-sigma uncertainties), and for BHVO-2 $^{206}Pb/^{204}Pb = 18.6324 +/- 0.0006$, $^{207}Pb/^{204}Pb = 15.5223 +/- 0.0005$, and $^{208}Pb/^{204}Pb = 38.2158 +/- 0.0013$ (2-sigma uncertainties).

4. Results

This section is organized with lava flows first, followed by shallow sills identified in chirp subbottom profile data collected by the AUVs, sediment hills uplifted by intrusions, sediment deformation, distribution of hydrothermal chimneys, distribution of circular to elliptical depressions in the sediment, and landslides, organized by region in the Escanaba Segment starting with the completely mapped NESCA region, then the MESCA and SESCA regions that are only partially mapped at high-resolution, and finally the far northern Escanaba Segment that is unmapped at high resolution.

4.1. Mapping lava flows and intrusions

Basalt occurs as surface or lava flows buried under several cm to tens of cm of sediment and as intrusions within the sediment section. Intrusions are divided into two groups: shallow (<~60 m depth) sills that are mapped using the SBP from the AUVs, and that uplift only low-relief hills, and sediment hills uplifted by >20 m by thicker, deeper unimaged sills and laccoliths (e.g., Central Hill at NESCA, Fig. 3A).

Lava flows are identified by surface textures in the multibeam maps, amplitude of the multibeam data, and signal strength of the SBP (Fig. 6A and B). If the lava surface is beneath thin sediment, there is still a strong reflection in the chirp subbottom data. In areas with surface flows, shallow sills or laccoliths could also be present, but are not imaged since the chirp energy does not penetrate the flows. Sills shallower than ~60 m depth (the depth of reflector I) detected in the chirp data do not underlie the taller uplifted hills, but occur adjacent to some of the tall hills. If deeper reflectors are obscured by a strong reflector, that strong reflector is interpreted as a sill intruded into this sequence (Fig. 6A). Shallow sills are not commonly restricted to a single reflector and generally migrate up section as they advance. The sediment section is deformed and disrupted over all sills and laccoliths.

Sills imaged in the SBPs are shallower than ~60 m, estimated from the drilled sequence of sediment reflectors A to I (Brunner et al., 1999; Zuffa et al., 2000) at ODP site 1037B. New chirp subbottom profiles crossing at site 1037B (labeled Fig. 5A and Fig. 5B on Fig. 2), collected by the AUV, show reflector I at 79 msec two-way-travel-time (TWTT); which corresponds to the 59 mbsf depth of the top of a sand layer interpreted by Normark and Serra (2001) as reflector I. Reflector I is a faint reflector that was not always imaged because the gain on the chirp sonar was not constant from survey to survey or between the two AUVs deployed. Regardless of gain, no reflectors below reflector I were imaged during any survey nor were any identified by Zuffa et al. (2000) or Normark and Serra (2001). Measurements of TWTT to reflector I vary

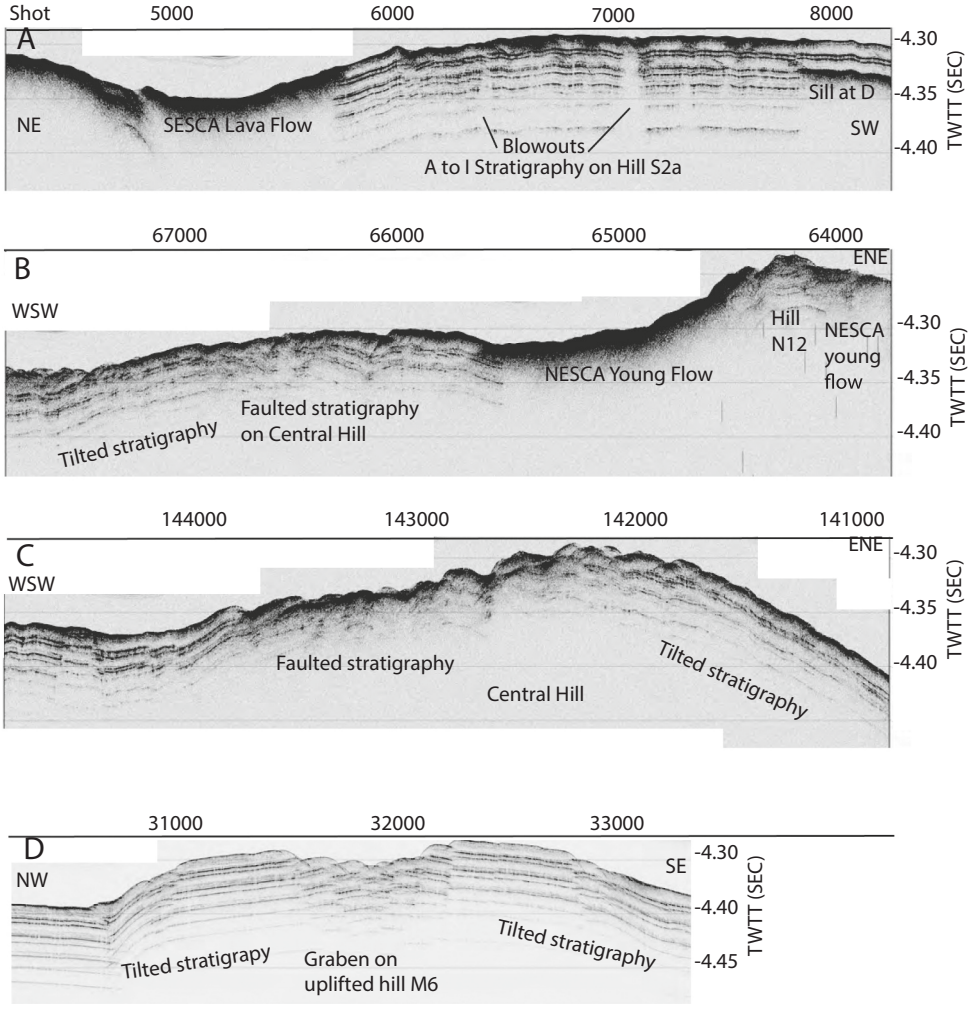

Fig. 6. Examples of AUV-collected SBPs showing: A) SESCA lava flow (shotpoints 4250–5750), full A-I sediment section (ping numbers 5750–7850) with blowouts (near ping numbers 6400, 7100, and 7300) and a sill along reflector D (ping numbers 7850–8250). Location of the SBP line is labeled 6A on Fig. 14. B). Cross section through southern part of Central Hill and Hill N12, the source of the NESCA Young lava flow. The center of Hill N12 is sediment and is surrounded by the NESCA Young lava flow. Central Hill is cut by numerous faults that disrupt the reflector A to I stratigraphy. Locations of the SBP line is labeled 6B on Fig. 2. C) Cross section through the north part of Central Hill at NESCA showing zone of sediment disruption from intense faulting and tilting of the entire sediment section on the east side of the hill. Location of the line is labeled 6C on Fig. 2. D) SBP line crossing Hill M6 at MESCA showing uplifted and tilted stratigraphy with central graben. Location of the line is labeled 6D on Fig. 13. The horizontal axes are in ping number since the start of the survey and 1000 pings is ~500 m; the A, B, C, and D profiles are 2.1, 1.9, 2, and 1.5 km long, respectively.

from 83 msec at the southern SESCA area to 79 msec at drill site 1037B at the southern end of the NESCA region, to 65 msec at Hill N3 in the northern mapped portion of NESCA. These TWTTs corroborate Normark and Serra's (2001) interpretation that the turbidites thin to the north in Escanaba Trough and suggest that the depth to reflector I varies from ~48–62 m below sea floor (mbsf) from north to south in the surveyed region and that the turbidites thin slowly to the north from SESCA to Central Hill at NESCA and more rapidly north of Central Hill. Background noise increased during the northernmost AUV survey (20160810m1) due to a gradual electronic failure and only surface lava flows could be identified with confidence in the northern part of this survey.

The taller uplifted hills are only rarely underlain by intrusions shallow enough to be imaged in the AUV chirp data. Hills at NESCA, SESCA, and MESCA are sediment uplifted by deeper intrusions and are designated with N, S, and M prefixes and number from north to south. The AUV bathymetry provides complete coverage of all hills at NESCA south of 41°04′N and partial maps of some, but not all, hills at SESCA and MESCA. Most hills consist of layered, tilted, uplifted sediment (e.g., Zuffa et al., 2000). The continuity of reflectors in the hills is commonly disrupted by small scale faulting (Fig. 6A, B, and C) and by blowouts that disrupt the sediment stratigraphy (Fig. 6A). In places the sediment disruption is pervasive so the reflector sequence cannot be identified, for example at Central Hill at NESCA (profile 13 in Ross and Zierenberg, 2009; and Fig. 6C). Steeply dipping reflectors are imaged at other hills, for example at Southwest Hill at NESCA (profile 13 in Ross and Zierenberg, 2009). Some hills, such as M6, display tilted stratigraphy on both sides of a summit graben (Fig. 6D).

The hills vary widely in lateral dimensions, height, style of sediment deformation, modification by secondary landslides, presence and abundance of hydrothermal chimneys, and presence, size and abundance of circular to elliptical depressions (Table 1). The hills can be categorized as five types: 1) broad dome-like hills with abundant ridge-parallel, concentric, or radial extensional cracks in the overlying sediment, 2) tall hills, often with landslides that extensively modify their margins, 3) smooth flow-shaped, flat-topped low hills, 4) hills that are partially to completely draped by lava flows, and then split and uplifted, 5) and one tumulus-like hill whose entire surface is lava. Each hill mapped at high-resolution is categorized as one of these five groups in Table 1.

4.1.1. NESCA lava flows

Surface lava flows are more common and extensive than previously mapped (Ross and Zierenberg, 1994) and important details about the distribution, thickness, and morphology are revealed in the new AUV bathymetry. The young, high-backscatter flow at NESCA, identified by Ross and Zierenberg (2009), is referred to here as the "NESCA Young flow" (Fig. 7A). The shallowest portion of the flow surrounds a small uplifted sediment hill, named here as N12 (Fig. 8A). The flow consists of three facies (Fig. 7B), with an early channelized sheet morphology (Figs. 7B and 9A) overlain by inflated and partly drained hummocky flows of pillow lava (Figs. 7B, 8B, and 9B), which in turn are overlain by hummocky pillow flows (Figs. 7B, 8C, and 9C) lacking drainage or molten cores, as described on Axial Seamount by Clague et al. (2017). The most distal part of the flow is an inflated sheet flow with thin pillowed margins. Later intrusions deform and brittlely shatter pre-existing sheet flows (Fig. 9C). Glass rind compositions of 44 new samples (Table 2 and Supplemental Table S1) are similar to the previously analyzed 22 dredged samples, one cored sample, and four submersible-collected samples from ten locations (Davis et al., 1994).

The NESCA Young flow is a transitional MORB (T-MORB with K_2O/TiO_2 of 0.150 ± 0.008, Fig. 10A) and MgO of 7.53 ± 0.18%. The flow covers 9.8 km^2 and has an estimated volume of ~0.28 km^3, which is imprecise because the pre-flow surface is unknown and likely complex. This volume is significantly larger than 0.045 km^3 suggested by Clague et al. (2009) that was subsequently used to model pyroclast dispersal by Pegler and Ferguson (2021). Isotopic and trace element data are presented in Supplemental Tables S2 and S3. The NESCA Young flow is the second most enriched (highest La/Sm and Nb/Y, Fig. 10B), with the most enriched REE pattern (Fig. 10C) and the most radiogenic Pb isotopic ratios (Fig. 10D) of lavas from the Escanaba Segment. The eruption that supplied the NESCA Young flow included a pyroclastic component (Supplemental Table S4) that dispersed glass shards (Davis and Clague, 2003; Clague et al., 2003) at least 6 km from the vent area (Clague et al., 2009; Pegler and Ferguson, 2021). The lava fragmentation that produced the shards was most likely caused by implosion of magmatic CO_2-filled bubbles that rose through the molten lava at the vent (Murch et al., 2022).

Another flow (labeled NESCA #1 on Fig. 2) with lower backscatter than NESCA Young flow is located north and northwest of Central Hill and west of the NESCA Young flow. It was identified as "sediment covered basalt" by Ross and Zierenberg (2009) and no samples were analyzed previously (Davis et al., 1994). The flow has now been observed and sampled along its southern margin where it consists of angular jumbled blocks of pillow lava and fractured pillow lava with moderate sediment cover and open fissures (Figs. 8D and 9D). Glasses from five samples (Table 2 and Supplemental Table S1) are T-MORB strikingly similar in composition to the NESCA Young flow with K_2O/TiO_2 of 0.141 ± 0.005 and MgO of 7.30 ± 0.06% (Table 2, Fig. 10A). The lava is just slightly less enriched than the NESCA Young flow (Fig. 10B and C). At least one of the samples appears to be slightly contaminated by sediment, which shifted its Pb isotopic values closer to that of sediment (Fig. 10D). This flow is interpreted to occur along axis to the north for ~5.5 km where lava crops out on the east side of Hill N4 and west of Hill N2. The northern portion is unsampled, so assignment to NESCA #1 flow is uncertain.

A third flow (labeled NESCA #2 on Fig. 2) was sampled north of the NESCA Young flow. This flow is almost completely buried by sediment, so is inferred to be older than either of the two flows described above. It occurs within an area mapped by Ross and Zierenberg (1994) as lava continuous with and north of the NESCA Young flow. This lava flow may be a rare example of an "invasive" lava flow (Byerly and Swanson, 1978; Beresford and Cas, 2001) that burrows under sediment to become a shallow sill after flowing on the surface, as the lava occurs as a mix of shallow sill and surface flow. Whole-rock analyses of the aphyric lavas confirm that the three widely spaced samples are compositionally alike (Supplemental Table S2). Only one of the three collected samples retained a glass rind, and it is primitive N-MORB with MgO of ~8.8% and K_2O/TiO_2 of 0.072 (Table 2, Fig. 10A), depleted La/Sm and Nb/Y (Fig. 10B), a strongly light-REE depleted pattern (Fig. 10C), and having the least radiogenic Pb isotopic ratios (Fig. 10D) of all lavas sampled from the Escanaba Segment. The two northern samples are near the southern margin of mapped flows that surround Hill N1 (Fig. 2).

Hill N3a has one small mound on its east flank (Figs. 3C and 11) that is reflective in the chirp data. It may be a small hummocky flow that erupted from a fault or from the margin of the central uplifted Hill N3, or it may be a large hydrothermal mound. No dives establish its composition or origin. The distribution of lava flows in the NESCA region is summarized in Fig. 12A.

The final basalt outcrop in the sedimented NESCA axial graben was sampled during *Alvin* dive 2039 to the east of Edifice REX (Fig. 1, Zierenberg et al., 1994), in a small fault scarp as the flow is entirely buried by sediment. The lava is the only E-MORB flow known from the Escanaba Segment (Davis et al., 1998; Fig. 10D). Pyroclasts with compositions overlapping this E-MORB flow are abundant in 30-cm push cores recovered during dive T194 (Supplemental Table S4) about 10 km west of the lava sample, on the western graben-bounding fault near the north end of the Escanaba Segment, indicating that this eruption had a significant pyroclastic component and the pyroclasts were dispersed more widely even than those of the NESCA Young flow (Clague et al., 2009).

Table 1
Dimensions and characteristics of uplifted hills.

Hill Name	Along axis length (km)	Across axis width (km)	Height of hill (m)	Depth to top of sill (m)	Type	Shape	Landslides[#]	Surface Cracking[*]	Chimneys[#]	Pockmarks[#]	Lava flow source[#]
NESCA											
N1	1.25	0.8	45	>60	2	scalloped plateau	many	p	N	Y	Y
N1a	irregular		12–23	9–49	3	low N-S ridges	N	N	N	Y	N
N2	2	1.8	29–61	>60	1	low dome	N	pr	N	Y	N
N3	1	1	124	>60	2	central punched hill	several	co	Y	Y	N
N3a	5	2	47–59	>60	3	lobate	1 to east	co	N	Y	Y?
N3b	0.3	0.3	22	>60	3	lobate	N	cr	N	Y	N
N3c	0.6	0.4	12	39–49	3	lobate	N	c	N	Y	N
N3d	0.4	0.4	5	13–19	3	lobate	N	N	N	Y	N
N3e	1	0.7	25	>60	3	lobate	N	rc	N	Y	N
N3f	1	0.3	28	>60	4	plunging ridge	N	p	N	Y, margins	N
N3g	0.9	0.3	20?	32–49	3	lobate	N	p	N	Y	N
N4	2.4	1	85	>60	4	uptilted split ridge	0.9 km to east	pr	Y	Y, west margin	Y
N4a	2.7	0.5	10	8–49	3	lobate	N	c	N	Y	N
N5	0.8	0.5	29	>60	2	punched hill	Y	p	N	Y	N
N5a	1.3	0.3	13	>60	3	lobate	Y	p	N	Y	N
N6	1.9	0.6	41–46	9–39	1	low dome, N-S fissure	N	p	N	Y	Y
N7	1.9	0.6	41–46	>60	3	punched hill	N	p	N	Y	N
N7a	0.4	0.4	9	9–23	3	lobate	N	c	N	Y	N
N8	2.2	0.9	0–35	8–49	3	lobate	N	r	N	Y	N
N9	1.4	1.3	37	>60	4	faulted dome	N	po	D, Y	N	N
Central Hill	2.4	1.6	125	404	1	faulted dome	one to north	pcr	D, Y	Y	N
N10	1.2	0.7	28	>60	1	low faulted dome	N	c	N	Y	N
N11	0.4	0.7	76	>60	5	tumulus	N	p	D, Y	Y-3	N
N12	0.3	0.3	129–144	>60	2	circular plug	N	N	D	N	Y
Southwest Hill	3.1	1.6	141–150	>60	2	scalloped tilted plateau	1.6 km to south and 1.7 km to east	cp	D	Y	N
N13	2.1	1.5	104–113	>60	1	low faulted dome	N	pr	N	Y	N
N13a	1.2	0.4	24	>60	3	lobe to E	N	p	N	Y, margins	N
N13b	1.4	0.5	22	>60	3	lobe to E	N	po	N	Y	N
MESCA											
M1	1.2	0.7	35	>60	1	low dome	N	p	N	margins/top	N
M2 (no AUV)	1.6	0.9		U	1	low dome					N
MC	1.6	1	61	>60	1	low dome	N	o	D, buried	N	N
M3 (no AUV)	2.3	2.7		U	1	four low domes					N
M4	0.8	1.2	47	>60	1	low dome	N	oc	N	NE and SW margins	N
M5	1.3	1	51	>60	1	low dome	N	rc	N	N	N
M6	1.2	1	46	>60	1	low dome	N	oc	N	N	N
SESCA											
North Hill (no AUV)	0.5	0.5	110	U	2	steep hill	U	U	S, at base	U	Y
S1	0.5	0.5	45	>60	2	tilted plateau	N		N	Y	N
S2a	5.7	3.8	81–82	*19* to >60	3	hill in north SESCA, see text	U	cr	S, Y	Y	N
S2b	0.9	1	56–64	*19*	3	sill southwest of S2a	N	r	N	Y	N
S2c	1	0.5	5–9	9–23	3	sill southwest of S2b	N		N	Y	N
S2d	1.2	0.3	44	>60	3	sill to west of S2a	N	c	N	Y	N
S2e	2.5	0.4	21	>60	3	sill to north of S2d	N		N	Y	N
S2f	1	0.6	24	>60	3	broad sill north of S2e	N		N	Y	N
S2g	1.3	0.8	24	>60	3	EW sill north of S2f	N	c	N	Y	N

(*continued on next page*)

Table 1 (*continued*)

Hill Name	Along axis length (km)	Across axis width (km)	Height of hill (m)	Depth to top of sill (m)	Type	Shape	Landslides[#]	Surface Cracking[*]	Chimneys[#]	Pockmarks[#]	Lava flow source[#]
S2h (no Auv)	1.1	1.3	34–46	U	3	distal lobe to NW	U	U	U	U	N
Hill 3170 (no AUV)	0.7	0.3	101	U	2	steep hill	U	U	S, at base	U	N
East Hill (no AUV)	>1.5	0.3	66	U	2	steep hill	U	U	U	U	N
S3 (no AUV)	~1.0	~1.0	75	U	1	steep hill	U	U	U	U	N
S3a	1.2	1.7	33–36	>60	3	inflated lobes to NW	Y	c	Y	Y	N
S3b	1.7	1.7	33–43	*48*	3	thinner lobe to NW	Y	c	Y	Y	N
S3c	0.6	0.3	10–16	*9–32*	3	irregular thin lobe to NW	U	c	U	U	N
S4	1.5	1	110–153	>60	2	steep hill	Y		N	N	N
S4a	5	2.5	45–58	>60	3	lobe to S	Y	c	Y	Y	N
S4b	0.7	0.8	35	>60	3	lobate	N		Y	Y	N

PM = possible hummocky pillow mound depths in italics are shallower than estimated using sill depth = 3*sill thickness.
U indicates unknown due to lack of high-resolution surveys depths to top of sill <60 m indicates imaged by subbottom chirp system.
[*] p = ridge parallel, o = oblique, c = concentric, r = radial.
[#] Y = mapped chimneys, N = no mapped chimneys, S = sulfides observed and collected.

4.1.2. NESCA hills uplifted by intrusions

Sills shallower than ~60 m depth were imaged in the SSBPs adjacent to some of the taller uplifted hills northeast of Central Hill (Fig. 12B. These underlie low uplifted hills (labeled N6 and N8 on Fig. 12), although their low height makes them less obvious than the taller hills. Three thin (5, 9, and 12 m thick) but still uplifted lobes, extend to the south (N3b), then southeast (N3c), and finally east (N3d, Figs. 11 and 12B) from Hill N3a (where the underlying sill is too deep to be imaged in SBPs) that extends around the central uplifted Hill N3 (where the underlying sill is also too deep to be imaged in SBPs). Sills N3b, N3C, and N3d shoal from reflector G (38.5 m depth) to reflector D (19 m depth) as they advanced to the south and southeast. The top of the uplifted hill deepens by ~23 to ~6 m as the underlying sill shoals to the south. Hill N9 is bounded on the east by shallow sills at variable depths (Fig. 12B) and in the central part by a sill at reflector D that extends to the west and under the eastern flank of low uplifted Hill N7 (Fig. 2). Between the northern flow and a small patch of flow NESCA #2 sampled 1.5 km farther south, the sill deepens from reflector B (8.5 m depth) to reflector E (23 m depth). The distribution of sills shallower than ~60 m depth is shown in Fig. 12B. These shallow sills are limited to the southern part of Hill N1a, small areas east and south of N3, and the area between the three surface flows and east of Hills N4 and N7.

All five types of uplifted hills occur at NESCA (Table 1, Fig. 12C). Low dome-like Type 1 hills are common and range from Hill N8 (Fig. 2) to the prominent Central Hill (Fig. 3A) with Hills N2, N10, and N13 in between in size and height. Most of the fractures are ridge-parallel. Central Hill (Fig. 3A) is an oval hill about 2.2 km along-axis and 1.4 km cross-axis and has an area of 3.25 km^2 and an estimated volume of 0.09 km^3. Central Hill is bisected by a roughly N-S axis parallel normal fault with the east side uplifted more than the west side. The eastern side has a series of radial fractures and a discontinuous concentric depression about half way from the summit to the eastern margin of the hill. The western half also has a series of radial fractures, but rather than a concentric depression, roughly N-S fractures parallel the central normal fault. A 400-m wide shallow slump indents the north-northeast margin of the hill. Hill N10 (Fig. 2), to the west of Central Hill, is 0.7 km E-W and ~1.2 km N-S. It is cut by a series of E-W fractures, with the southernmost fracture concentric around a circular depression in the sediment.

A single sample of basalt with a glass rind quenched against baked sediment was recovered at the base of ODP hole 1038I on Central Hill. This sample is from the top of the laccolith that uplifted Central Hill. The analysis of this glass (Table 2 and Supplemental Table S1) has 8.21% MgO and K_2O/TiO_2 of 0.19, making it a moderately primitive T-MORB that has characteristics similar, but not identical, to the NESCA Young and NESCA #1 lava flows. The glass contains sparse plagioclase and olivine microphenocrysts.

Five tall Type 2 hills, often with landslides that extensively modify their margins are identified at NESCA (Table 1). Southwest Hill is the largest (Figs. 2 and 3B). Most of the landslides apparent in the bathymetry have emanated from just three of them (Figs. 3A, B, C, and 12F). with Southwest Hill being the largest in the region. Hill N1 (Fig. 2) is so deeply embayed by landslide scars in all directions that there is little original sediment surface on the uplifted hill. This hill is surrounded by lava flows that trace uphill and indicate the eruptive fissures were along faults bounding the hill. Hill N5 (Fig. 2) on the eastern margin of the axial graben, was uplifted prior to faulting that formed the axial graben as the hill is broken up by ridge-parallel normal faults. Margins of the sill can be identified by an arcuate arrangement of circular depressions to the southwest of the hill. Southwest Hill (Fig. 3B) is also heavily scalloped by landslides. One advanced east, depositing blocks on the lower southwestern slope of Hill N10 and Central Hill that were then uplifted with Central Hill, and another produced a debris avalanche deposit that extends ~1.5 km from a small amphitheater on the south margin of the flat summit. Hill N3 (Fig. 3C) is cut by numerous fractures, some of which are radial and some are perpendicular to the ridge axis. The E-W fractures form a shallow graben cutting across the central part of the hill, and landslides emanate to the SW and SE. Hill N12 (Figs. 3A and 8A) is relatively tall like other Type 2 hills, but it lacks secondary landslides that scallop the summit. The circular ~0.4 km-diameter sediment plug in the center of Hill N12 (Figs. 3A and 8A) is ~20 m shallower than the surrounding NESCA Young hummocky lava flows. As observed at Hill N1, the ring faults surrounding the circular hill N12 were eruptive fissures (Fig. 6B) that fed the NESCA Young flow. These accumulating flows buttressed the margins of the central sediment hill as it was uplifted and may have minimized subsequent landslide activity.

Type 3 (smooth, flow-shaped, flat-topped) hills are lower in profile, and have sedimented surfaces with cracks that can be ridge-parallel, concentric, or radial, sometimes with several styles on the same hill. The largest Type 3 hill mapped at NESCA is N3a (Figs. 3C and 11) which has an area of 9.54 km^2 and an estimated volume of 0.24 km^3. Only the southern half is mapped with 1-m bathymetric data, and its underlying sill is not shallow enough to be imaged in the SBP data. Its broad, rectangular-shaped, flat-topped plateau is 3.3 km along axis and 2.1 km across axis and ~45 m tall, and surrounds the 120-m tall, 1-km diameter,

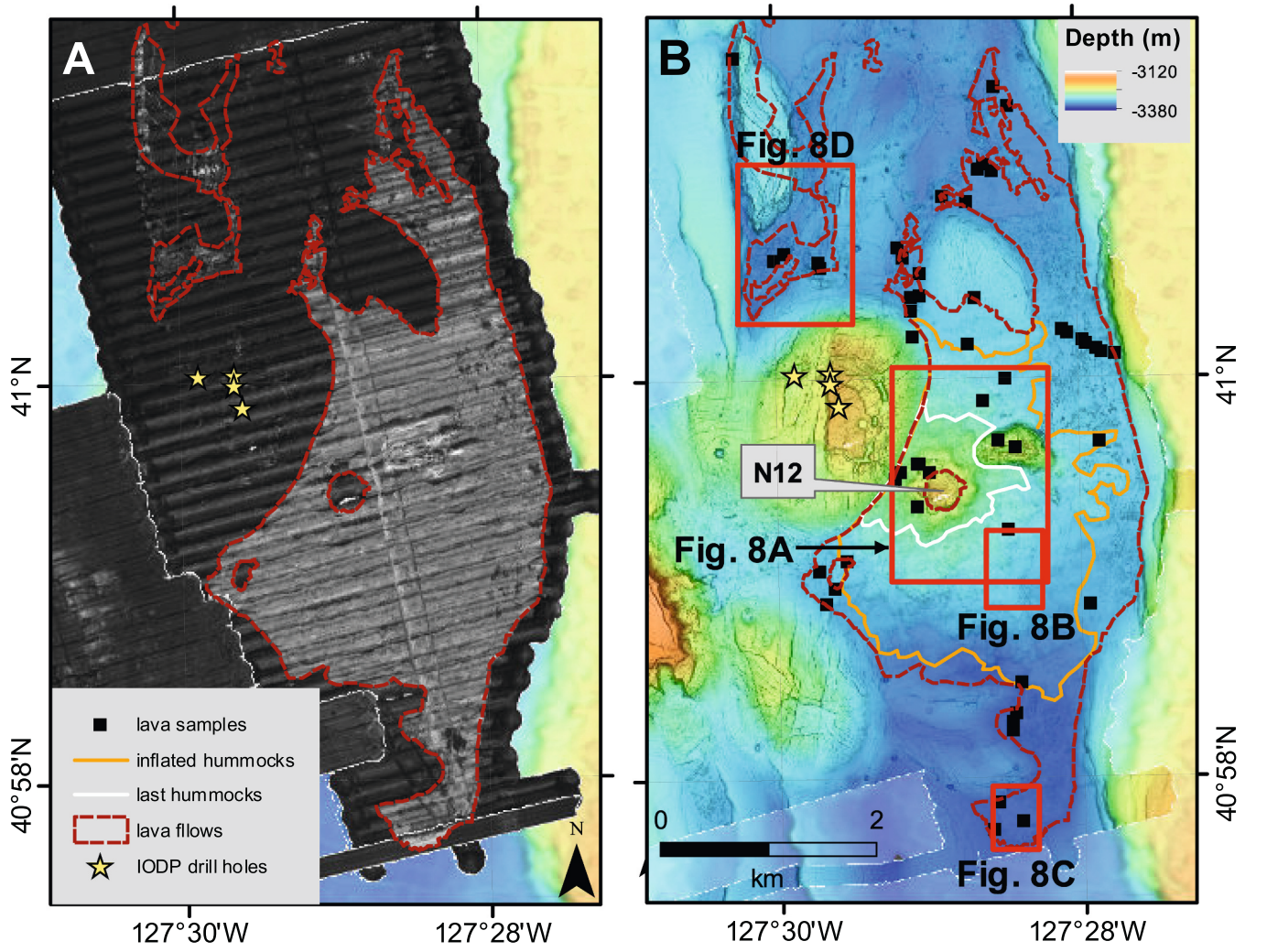

Fig. 7. A) Backscatter of NESCA Young lava flow derived from AUV multibeam backscatter. The NESCA Young flow has high backscatter and the chemically similar flow NESCA #1 (NNW of Central Hill) has uneven backscatter. Hill N12 is the source of the NESCA Young flow. Sediment has low backscatter. ODP drill sites are shown as yellow stars. B) Lava flow outlines with NESCA Young flow divided into an early channelized flow facies (red outline), a later inflated hummocky flow facies (yellow-orange outline), and a youngest hummocky flow facies (white outline). Red boxes outline enlarged maps shown in Fig. 8. Black squares are new lava sample locations. (For interpretation of the references to colour in this figure legend, the reader is referred to the web version of this article.)

Type 1 Hill N3. Type 3 Hills N3b-g radiate from Hill N3a, and all are lower expressions of the same form. Type 3 Hills N5, N6, and N8 (Fig. 2) are low hills that are located northeast of Central Hill, in an arc of complex bathymetry; they could be parts of the same hill, or two separate hills, as we have shown them. Type 3 Hills N13a and N13b extend to the east from Type 1 Hill N13 (Figs. 2 and 12C).

Type 4 hills N4 and N7 (Figs. 2 and 12C) consist of uplifted and tilted layered sediment that is partially covered by surface lava flows. The AUV bathymetry and backscatter data suggest the flows are a surface veneer of lava erupted from fissures that parallel the axis. Eruption of the lava flows occurred prior to uplift of the hills. This relationship has not been confirmed or sampled by ROV.

The single Type 5 hill N11 (Figs. 2 and 12C), a 0.7 (E-W) by 0.4 km tumulus, is the only hill consisting entirely of lava; it is located in the east-central part of the NESCA Young lava flow. There is a central irregular depression and several radial cracks on the east end formed as the lava crust buckled upwards. Observations during an ROV dive show the outer steep slopes consist mostly of steeply tipped sheet flows.

4.1.3. *MESCA hills uplifted by intrusions*

There are no lava flows or shallow sills imaged by the AUV SBP system at MESCA. The seven uplifted hills (M1 to M6 and MC) (Fig. 13) are all Type 1 hills (Table 1), but with just a single swath of high-resolution bathymetry each is still largely unknown. Hills M3 are a complex of three or four adjacent hills near the fault bounding the axial graben on the west side. The SBP data at Hill MC (Hill C in Zierenberg et al., 1994) show hard but chaotic near-surface reflectors and no sub-bottom reflectors. Coring on this hill (Zierenberg et al., 1994) recovered sulfide veining in turbidite sand.

4.1.4. *SESCA lava flow*

A lava flow located in the northern half of SESCA (Fig. 14) is a channelized sheet flow (Fig. 9E) with lobes that advanced southwest and northwest on top of thick turbidite sediment (Figs. 15B and 16A). The southwestern margin of the flow has margin-parallel clefts (Fig. 9E and F) similar to those observed on thick inflated flows, such as the one in the center of the caldera at Axial Seamount (Appelgate and Embley, 1992; Clague et al., 2013). The interior surface of the flow is complex with sediment-draped leveed channels and lava ponds (Fig. 15C), drapery folds (Fig. 9G), and is cut by occasional open fissures (Fig. 9H). The flow has an area of 7.9 km^2 and an estimated volume of 0.08 km^3 assuming an average thickness of ~10 m.

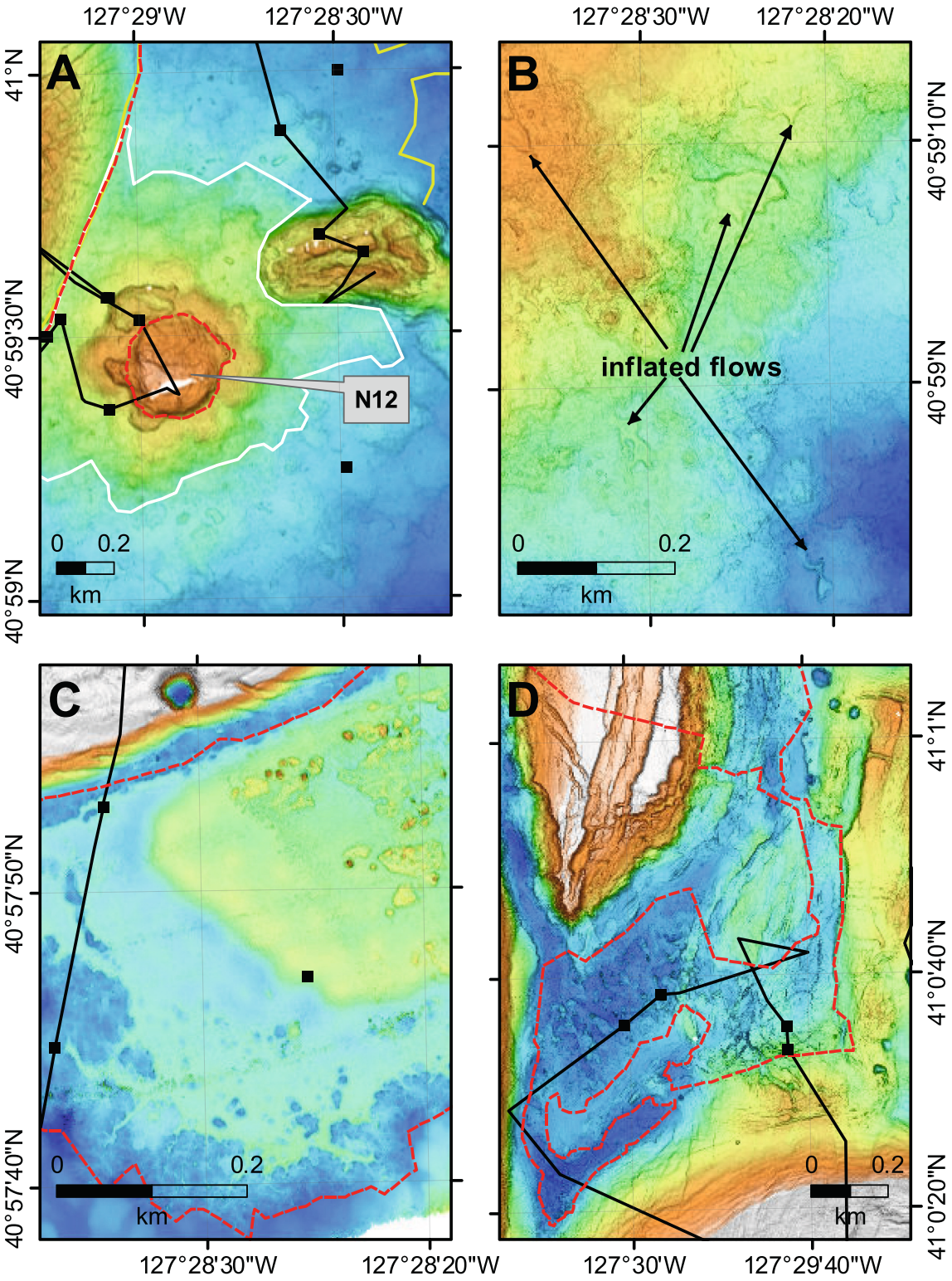

Fig. 8. Detailed bathymetric maps of NESCA flow morphologies. A) The source vent for the NESCA Young flow is along a ring fault around labeled Hill N12 and flows proximal to vent have hummocky morphology (white outline). B) Hummocky flow morphology transitions into inflated hummocky flow morphology with collapse depressions (examples indicated by arrows) at intermediate distances from vent. C) Distal southern end of early channelized flow facies, showing inflated flow interior (green and yellow-green) and individual m-scale pillow lobes on margin of flow. D) Bathymetry of tectonically disrupted hummocky NESCA #1 flow located NNW of Central Hill. The flow has intermediate backscatter (Fig. 7A) and is compositionally similar to the NESCA Young flow (Figs. 2 and 10A). Small black squares are locations of lava samples (Supplemental Table 1). (For interpretation of the references to colour in this figure legend, the reader is referred to the web version of this article.)

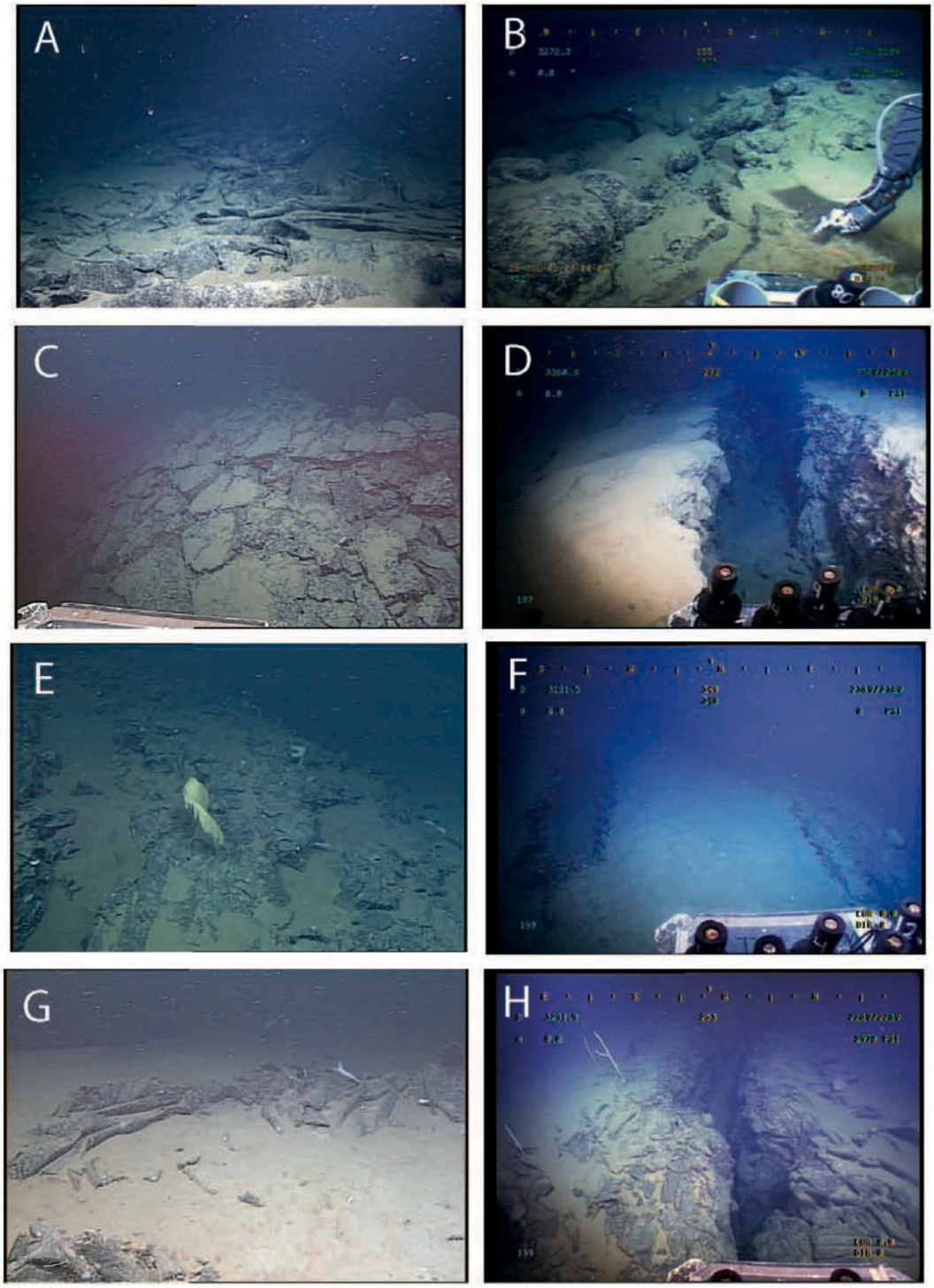

Fig. 9. Framegrabs from ROV video of lava flows. A) Folded sheet flow in channelized flow facies of NESCA Young flow, NE of Central Hill. Image T890_06_34_27_00 at 3325 m depth. B) Pillow lava in hummocky flow facies between Central Hill and Hill N12, NESCA Young flow. Image T452_10_23_21_10 at 3274 m depth. C) Lobate flow in hummocky flow facies of NESCA Young flow, deformed and fractured by subsequent uplift. Image T198_01_25_51_12 at 3301 m depth. D) Fissure cutting sediment-covered lobate flows in NESCA #1 flow. Image T197_05_26_09_17 at 3336 m depth. E) SESCA sheet flow on top of Hill S3. Concentric cracks due to uplift that raised Hill S3 with the already emplaced SESCA flow. Image T199_01_40_48_01 at 3281 m depth. F) SESCA sheet flow with sediment cover on top of Hill S3. Another view of concentric cracks in the SESCA flow formed due to subsequent uplift. Image T199_01_04_23_16 at 3259 m depth. G) Folded sheet flow in channelized flow facies of SESCA flow. Image T199-02_36-37_00 at 3236 m depth. H) Open fissure cutting the SESCA sheet flow of channelized flow facies. Image T199_06_42_05_19 at 3292 m depth. All images are roughly 5 m across and locations of A to D and E to H are shown on Figs. 3A and 14, respectively.

The southern portion of the flow is now atop the northern part of uplifted Type 3 Hill S2a (Figs. 14 and 15A). Previous mapping (Ross and Zierenberg, 1994) interpreted this flow as two separate flows, but subsequent sidescan data (Fig. 15B, Ross and Zierenberg, 2009) and the new SBP data show that they are continuous, but vertically offset by uplifted Hill S2a. The detailed bathymetry shows sharp-edged slope-parallel fractures on the steep NE slope of Hill S2a (Fig. 15D). Observations during dive T199 also show the continuity of lava on the steep slope but

Table 2
Average normalized electron microprobe analyses of glass rinds for identified flow units.

Flow Unit	#	Type	SiO_2	TiO_2	Al_2O_3	FeO*	MnO	MgO	CaO	Na_2O	K_2O	P_2O_5	S	Cl	Mg#	K_2O/TiO_2
Average SESCA flow	15	T-MORB	51.08	1.06	15.37	8.54	0.16	8.46	12.81	2.22	0.12	0.09	0.081	0.005	67.5	0.118
1σ			0.09	0.05	0.17	0.19	0.01	0.12	0.10	0.03	0.01	0.01	0.002	0.002	0.8	0.012
Average NESCA Young flow	46	T-MORB	50.79	1.68	15.22	10.06	0.17	7.53	11.40	2.59	0.25	0.18	0.104	0.009	61.1	0.150
1σ			0.13	0.07	0.18	0.19	0.01	0.18	0.13	0.06	0.02	0.01	0.008	0.003	0.9	0.008
ODP1038I-43X-3	1	T-MORB	49.79	1.41	16.06	9.15	0.17	8.25	11.95	2.67	0.27	0.17	0.106	0.016	65.4	0.193
Average NESCA #1 flow	5	T-MORB	50.88	1.76	14.87	10.41	0.19	7.30	11.41	2.65	0.25	0.19	0.106	0.007	59.5	0.141
1σ			0.04	0.02	0.09	0.09	0.01	0.06	0.03	0.02	0.01	0.01	0.010	0.002	0.3	0.005
NESCA #2 flow sample T887-R1*	1	N-MORB	49.76	1.06	16.39	8.60	0.15	8.79	12.62	2.39	0.08	0.06	0.089	0.004	68.2	0.072
Average of flows in west axial graben wall	4	T-MORB	50.68	1.50	15.12	9.76	0.18	7.90	11.93	2.50	0.18	0.15	0.095	0.007	62.9	0.117
1σ			0.21	0.06	0.09	0.08	0.01	0.33	0.06	0.03	0.01	0.01	0.003	0.003	1.1	0.002
Average all northern cone samples	32	N-MORB	50.14	1.44	15.90	9.40	0.17	8.34	11.76	2.53	0.09	0.13	0.092	0.005	65.0	0.066
1σ			0.19	0.08	0.24	0.37	0.01	0.23	0.20	0.04	0.02	0.01	0.011	0.006	1.2	0.008

# Indicates number of samples used in average. Complete data are in Supplemental Table S1.

absent the elongate pillows expected if the lava flowed down the slope towards the NE. This distal part of the flow formed numerous low-relief lava shields (Fig. 15D) that were observed and sampled during ROV dive T199. Some of these shields have small leveed ponds at their summit. Shields similar to these have not been mapped elsewhere in Escanaba Trough.

This flow appears to be related to the intrusion that uplifted North Hill (Fig. 14). The flow can be traced to the first large offset normal fault that bounds the SW edge of North Hill (Fig. 15A and B). The flow is cut by meter-scale faults approaching the hill, but is both cut by and overflows one small fault near the margin of North Hill (Ross and Zierenberg, 1994), suggesting the flow was contemporaneous with uplift of that hill.

The 15 new lava samples (Fig. 10A and B) include 6 from on top of Hill S2a and the rest between Hill S2a and North Hill). They have nearly identical compositions that are similar to four dredged, and therefore poorly located, samples analyzed previously (Davis et al., 1994). The new samples are T-MORB, more primitive than the NESCA Young flow, with MgO of 8.45 ± 0.12 wt% and K_2O/TiO_2 of 0.118 ± 0.012 (Table 2 and Supplemental Table S1).

4.1.5. SESCA hills uplifted by intrusion

Shallow sills were mapped with the AUV SBP system in just four areas, all under or adjacent to Hills S2a and S3c (Fig. 16B). The most extensive area is under Hill S2a and Hill S3a where sills were mapped at depths between 48 and 19 m (stratigraphic reflectors H to D, Fig. 6A). It is not clear where the shallow sills extending SW from Hill S2b and those extending NW from Hill S3b intersect or overlap as sill depths in that region are highly variable. There are small areas of shallow sills mapped on the NE margin of Hill S2a along reflector G or H and a larger zone adjacent to the western margin of Hill S2b, mostly along reflector G or H. The entire Hill S3b is underlain by a sill at ~48 m depth. No sills are within ~60 m of the surface under Hills S3 or S4.

Uplifted hills at SESCA (Figs. 14 and 16C) are more restricted in type as there are no identified Type 4 or Type 5 hills, although this may reflect incomplete high-resolution map coverage. Hill S3 is the only Type 1 hill, but it is only mapped at coarse resolution. Hills North, S1, 3170, and East in the northern portion (Zierenberg et al., 1994) and S4 in the southern portion are Type 2 hills (Table 1, Fig. 14). Of these, only Hills S1 and S4 were partially mapped at high-resolution. Most uplifted hills are only mapped with ship-based EM300 multibeam.

Hill S1 is a low, tilted Type 2 sediment hill that is nearly surrounded by the SESCA lava flow. It is shallowest to the NE. Hill S4 (Fig. 14), a taller Type 2 hill heavily scalloped by landslides (Fig. 17C), is also tilted but with the shallowest portion of the summit to the SW. The A to I sediment reflectors are evident in SBPs of the tilted sediments on both (Fig. 16B).

Three series of extensive Type 3 Hills that superficially resemble thick flows (Hills S2a to2h, S3a to 3c and S4a) occur at SESCA. Individual lobes are between 25 and 60 m thick, 5 or more km long, and several km wide (Table 1, Fig. 14). The sill S4 is 11.4 km^2 in area and has a volume estimated at 0.26 km^3. Numerous other smaller and lower hills occur in the region; they were not mapped at high resolution; and will not be described nor discussed further. Several lobate hills with similar Type 3 characteristics extend out from the margins of Type 2 hills at NESCA.

4.2. Secondary impacts of intrusions

4.2.1. Sediment deformation on uplifted hills

There are five main styles of sediment cracks or fractures on the surfaces of uplifted hills: concentric, radial from the summit, parallel to the margin of the uplifted hill, and parallel and perpendicular to the ridge-axis. The sediment deformation style for each hill is listed in Table 1. Some styles are indicative of specific types of uplifted hill. For example, concentric fractures are limited to Type 2 dome-like hills such as Central Hill, whereas margin-parallel fractures are especially common on Type 3 low lobe-shaped hills (e.g., Fig. 16D). The other types commonly occur together on the same hill, such as Hill N3 (Fig. 3C). In some examples, such as Central Hill, the concentric fractures are decorated with circular depressions and occur among ridge-axis parallel fractures and faults (Fig. 3A). As seen in the SBP, surface fractures have offset the sediment reflectors (Figs. 6A-D), but the sloped surfaces of Type 1 and 2 hills often exhibit uniformly tilted reflectors (Fig. 6C, D). Where landslides have scalloped the margins, the reflectors are abruptly truncated.

4.2.2. Hydrothermal chimneys

The AUV bathymetry and backscatter show chimneys and clusters of chimneys not previously mapped or observed. On Central Hill at NESCA, most of the chimneys mapped on the north and east flanks were previously identified from camera tows or dive observations (Zierenberg et al., 1994), but others are revealed near the summit and on the south and northwest flank of the hill (Fig. 3A). Deposits at some of these may have been sampled by dredges (Koski et al., 1994), but the provenance of those samples is poorly known. Likewise, chimneys on the southeast flank of Southwest Hill were previously known (Zierenberg et al., 1994),

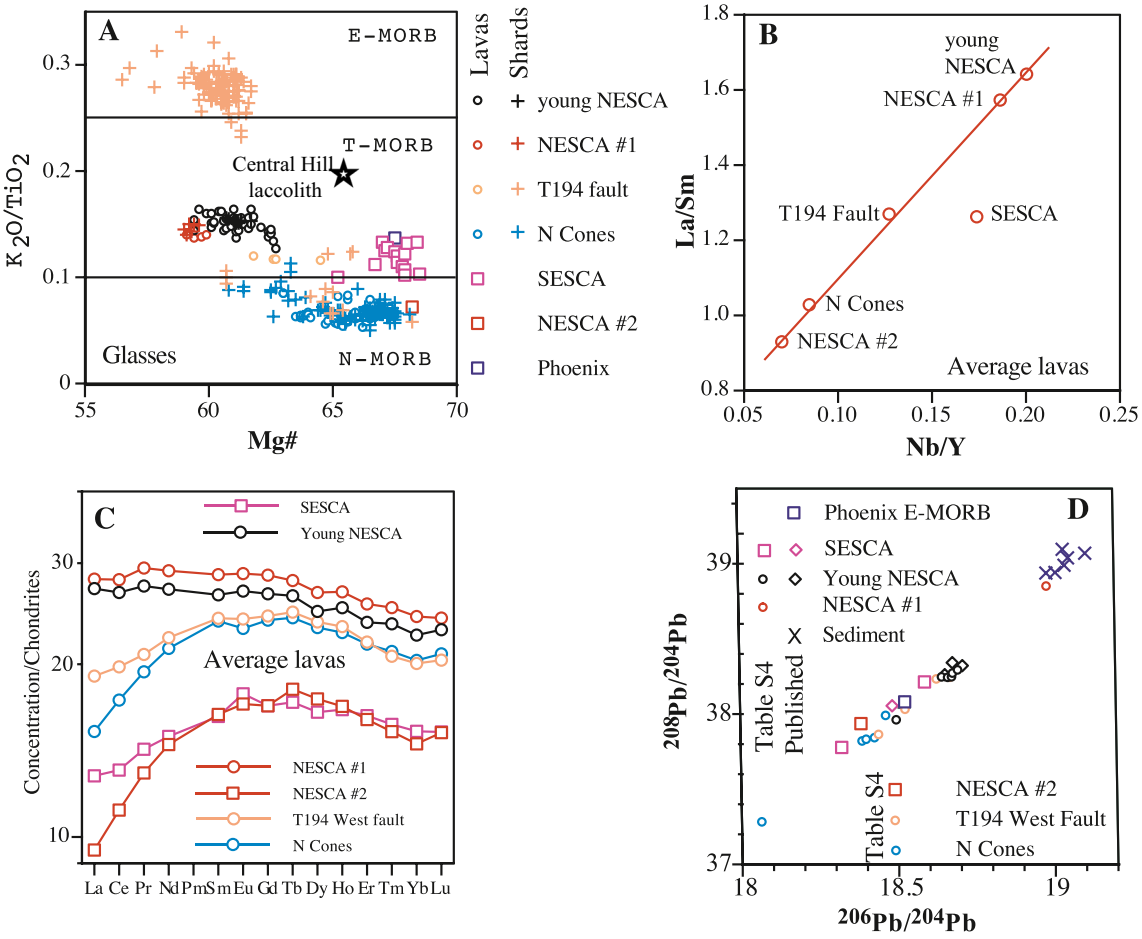

Fig. 10. Chemical plots of Escanaba lava flows. A) K_2O/TiO_2 as a function of Mg# (=100 Mg/(Mg + 0.85Fe) for glass rinds on lava flows (Supplemental Table S1) and glass shards recovered in push cores (Supplemental Table S4). Escanaba Segment has a wide range of MORB compositions ranging from N-MORBs such as NESCA #2 and the northern cones, to E-MORB glass shards that are chemically similar to a flow (sample *Alvin* 2039–2; Davis et al., 1994, 1999) from the northern end of the segment. The glass analysis of the top of the laccolith under Central Hill drilled at ODP site 1038I (Table 2) is shown as a star and labeled. B) La/Sm plotted vs Nb/Y for averages of samples from each flow unit (Supplemental Table 2, only new internally consistent data are plotted). All samples plot along a mixing line from enriched (high La/Sm, high Nb/Y) to depleted compositions (low La/Sm and low Nb/Y) except SESCA flow. C) Chondrite-normalized REE plots of average compositions of samples from each flow unit. The patterns range from strongly light-REE depleted (flow NESCA #2 flow) to moderately LREE depleted (SESCA, northern cones, and T194 west fault) to slightly LREE enriched (NESCA Young and NESCA #1 flows). All except NESCA Young and NESCA #1 flows have highest normalized values in the middle-REE range. D) Pb isotope diagram showing $^{208}Pb/^{204}Pb$ as a function of $^{206}Pb/^{204Pb}$. Samples include lava analyses (diamond symbols) and sediment analyses (X symbol) from Davis et al. (1998 and references cited therein) and new analyses (Supplemental Table S3). All the samples plot on a mixing line with local sediment as the radiogenic end-member.

but those mapped by the AUV surveys on the northwest and west flank of the hill were unknown. Other previously unmapped chimneys at NESCA, all on uplifted hills, occur on Hills N3 (Fig. 3C), N4, N6, and N8 at NESCA (Fig. 12D). The AUV mapping located 106 chimneys in the NESCA mapped area and detected small positive temperature anomalies indicative of active hydrothermal discharge at the north margin of Central Hill, the summit of hill N3, the southern end of Southwest Hill, and the north margin of hill N13 (Fig. 2). The presence of the small temperature anomaly at Central Hill indicates that active venting continued in the NESCA region until at least 2016. None of the other water column anomalies are near known vents. The ones at N3 and N13 are also not near mapped chimneys. Of the newly mapped chimneys only the one on Hill N8 was observed and sampled during an ROV dive and it was inactive. Dredges also sampled sulfide, probably from Hill N6 (Koski et al., 1994); it is unknown if the samples are from the mapped chimneys or lower relief massive deposits. The ROV dives revisited an active vent area at NESCA (Fig. 4C) and discovered several sites with active clam fields (Fig. 4D), but most chimneys observed were inactive (Fig. 4E). The open hole at ODP site 1038A was found to be discharging hydrothermal fluids at a low rate and to support a microbial community (Fig. 4B). Outside the AUV mapped area, Cu-rich sulfide was also recovered during *Alvin* dive 2039 on the east flank of uplifted hill Edifice REX (Zierenberg et al., 1994).

No sulfide chimneys were imaged at MESCA (Fig. 13) and no water column temperature anomalies were detected, despite recovery of sulfide-bearing sands in a core on Hill MC (Zierenberg et al., 1994). The incomplete coverage of AUV data may account for their apparent absence.

At SESCA, sulfide chimneys are particularly abundant on the broad, low uplifted Type 3 Hill S2a (Figs. 16D, 4F), with most on the southwest portion and rarer, more scattered, examples on the northeast part. The chimneys tend to occur in clusters, and none are taller than about 5 m (Fig. 17A). Chimneys also occur on the low-relief uplifted hills of the Type 3 Hills S3 and S4 complexes farther south, but are fewer in number and are only several m tall. However, a small water column temperature anomaly was detected on the west side of Hill S4 (Fig. 14). On the AUV-mapped portions of Hills S3a, S3b, and S4a, most are near the edges whereas those on Hill S2a tend to be on top. The taller, more rugged, uplifted Type 2 Hills S4 revealed no chimneys in the AUV mapping, unlike Type 2 Hills East, North, and 3170 where prior exploration found

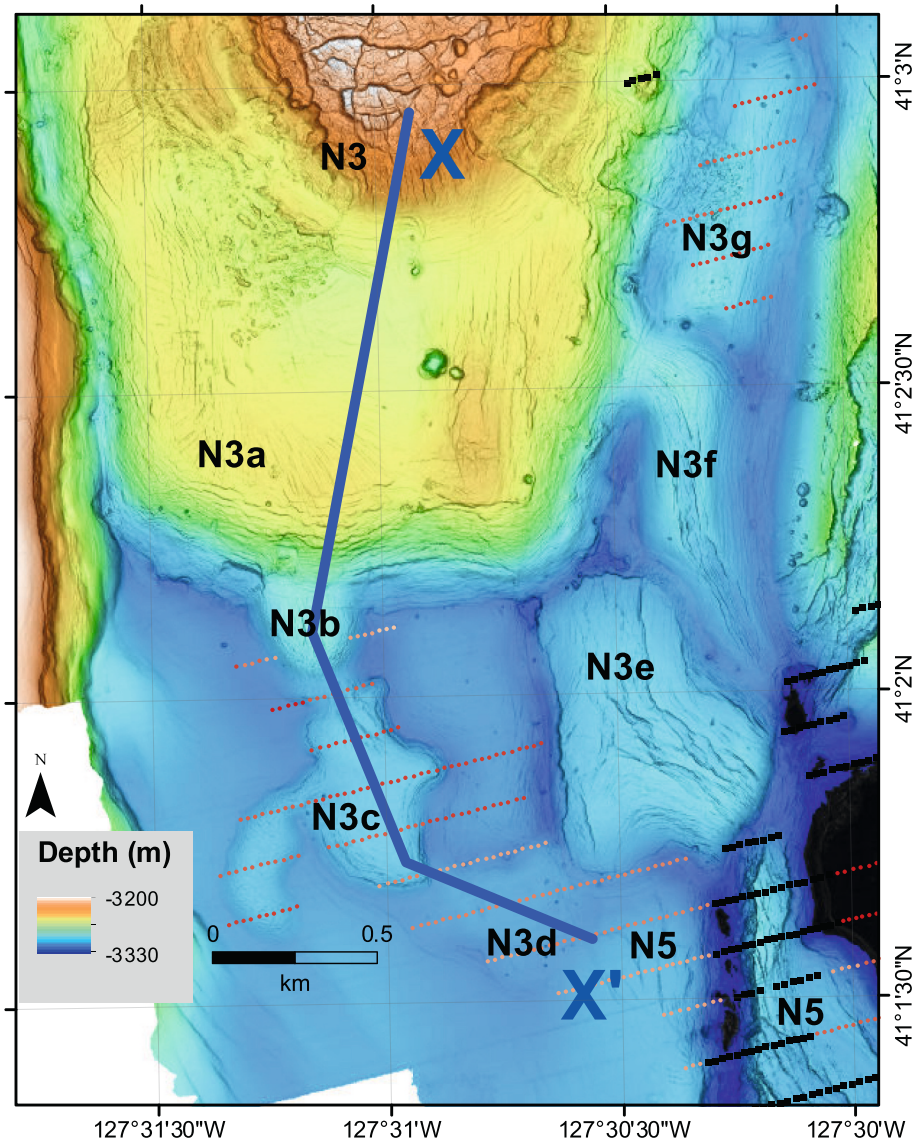

Fig. 11. Close-up of the southern portion of Hill N3 showing relations of uplifted hills and shallow sills. The bold line shows the location of a cross section constructed from bathymetry and SBP data (Fig. 20). Shallow uplifted hill names as in Table 1 and Fig. 2 with surface lava flows in black and depth of sill upper surfaces colour-coded as indicated in Fig. 12B.

sulfides (Zierenberg et al., 1994). ROV dive T200 crossed the northern low-relief uplifted Hill S2a (Fig. 12) and observed and sampled a number of the mapped chimneys in the northeast part. The observed chimneys are inactive and small, as also seen in the mapping data, which shows 156 chimneys (Fig. 16D). If the entire SESCA region were mapped at high-resolution, the population of chimneys would likely double.

4.2.3. Pockmarks and hydrocarbons

Small shallow circular to ellipsoidal craters in the sediment are abundant at NESCA, where the AUV mapped region has 320 (Fig. 12E) and at SESCA, where the more limited mapped area has 286 (Fig. 16E). Fourteen also occur on the single zig-zag track of data collected at MESCA (Fig. 13). These pits were unrecognized prior to the collection of the high-resolution AUV bathymetry, despite the number of submersible and ROV dives done in the area (Morton et al., 1994). They resemble pockmarks observed on continental margins (e.g., Nelson et al., 1979; Hovland et al., 1984; Vogt et al., 1984; Cathles et al., 2010; Kelley et al., 2010) as they lack elevated rims; they are referred to as pockmarks through the remainder of this paper. Pockmarks are located on the flanks and tops of uplifted hills and above sills shallower than ~60 m mapped in the SBP. Pockmarks are absent in undisturbed sediment fill of the Escanaba Segment. The pockmarks mapped at MESCA by the zig-zag track (Fig. 13) are mostly on the edges of the five uplifted hills (M1, MC, M4, M5 and M6) crossed by the AUV, although a cluster of them occurs between Hills MC (Zierenberg et al., 1994) and M2 (Fig. 13).

At NESCA, the pockmarks are 3 to ~100 m in diameter and the deepest and largest is 24 m deep. The largest occur on the flanks of large uplifted hills such as Central Hill (Fig. 3A). The four largest pockmarks at NESCA are 62, 70, 72, and 100 m in diameter. At SESCA, pockmarks are 3 to 150 m in diameter, the largest is also 24 m deep. Pockmarks on Hill S3 are arranged in a distinct crescent along the margin (Fig. 17B). One pockmark on the north flank of Central Hill has bacterial mats and a clam community in the eastern part of the pockmark that were observed during two ROV dives.

Hydrocarbons, in the form of tar mounds or layers on the sediment surface were observed during several ROV dives at NESCA (Figs. 4G and 12E) and several push cores had a distinct diesel aroma. The tar samples are similar to materials from NESCA described previously by

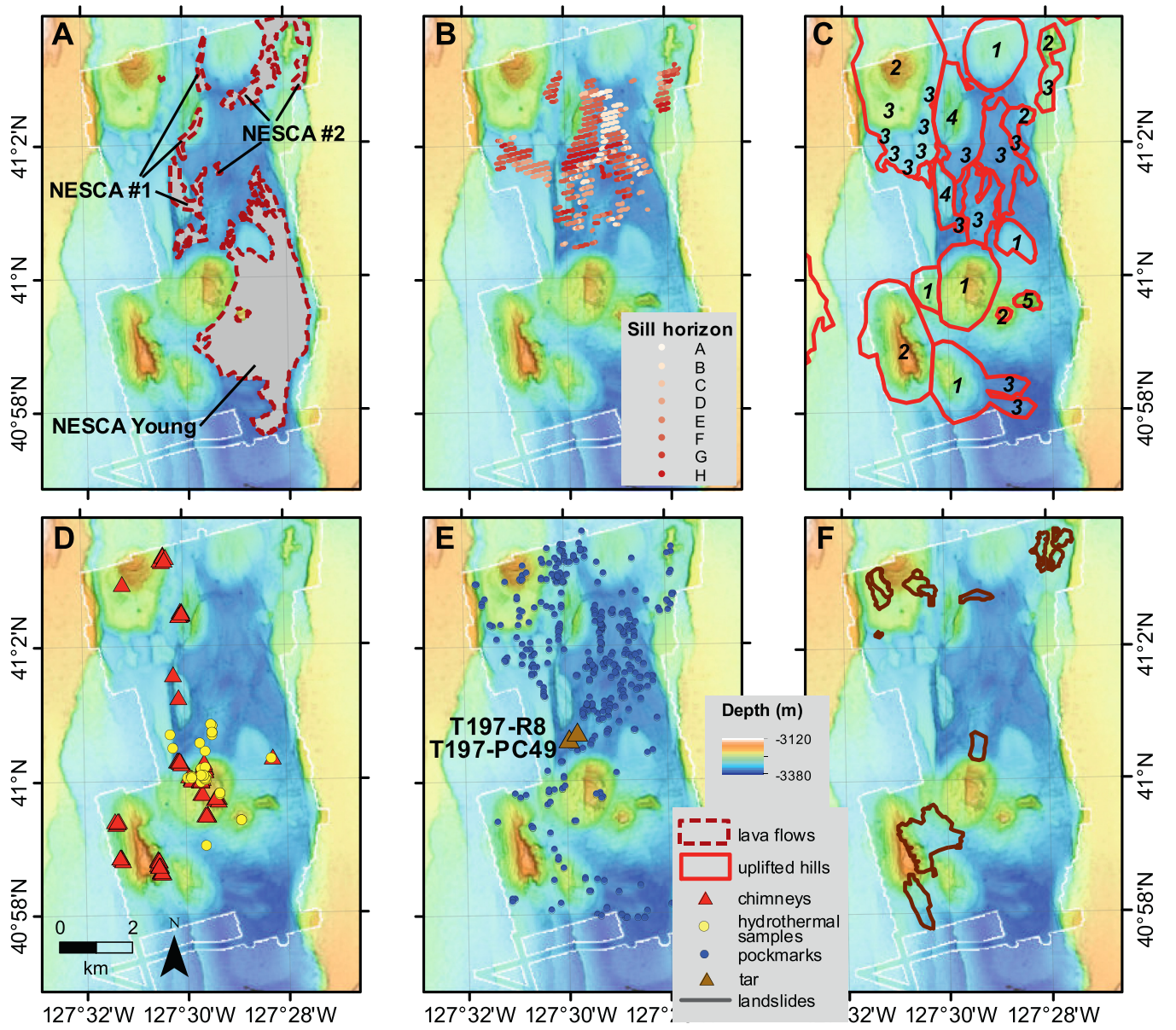

Fig. 12. Maps of NESCA showing: A) Distribution of lava flows identified as NESCA Young, NESCA #1, and NESCA #2. Chemistry of the flows given in Table 2 and Supplemental Tables S1 to S4. B) Distribution and depths of sills shallower than ~60 m determined from the SBP lines. C) Uplifted hills interpreted to mark locations of underlying sills; numbers indicate interpreted hill types. D) Mapped hydrothermal chimneys and locations where hydrothermal deposits were sampled. E) Pockmarks and location of tar mound (T197-R8) and core T197-PC49 with diesel smell (Fig. 4G). F) Secondary landslides.

Kvenvolden et al. (1994), based mainly on dredged samples. One tar sample had elongate flow lobes and had built a 30-cm tall mound, now inactive, around a central discharge point. Tar outcrops host abundant benthic animals, mainly anemones.

4.2.4. *Landslides*

Landslides modify the slopes on many of the uplifted hills, especially the taller hills such as N1 and Southwest Hill at NESCA (Figs. 3B and 12F), and S4 at SESCA (Figs. 16F and 17C). A ~400 m wide slump extends 600 m from the north flank of Central Hill (Fig. 3A). Slides also occur on the outer slopes of lower-relief uplifted hills such as N4, N5, and Central Hill at NESCA (Fig. 12F). The outer margins of the shallowest part of the Hill N3 shed landslides to the south-southeast and the southwest, that emplaced debris fields on the surfaces of surrounding Hill N3a, which in turn shed debris east onto Hill N3g (Fig. 3C).

Most of the slides are debris avalanches that deposited scattered blocks downslope of the headwall scarps. Several have headwalls that are semi-circular and resemble part of a pockmark with the downslope portion having slid away, leaving an amphitheater, scalloped sidewalls, and debris at the base. Southwest Hill (Fig. 3B) displays these features in a series of overlapping semi-circular headwalls on the east side and one on the south side. The distal slide blocks on the east side are uplifted with the seafloor during emplacement of the sill beneath Central Hill, consistent with the inferred older age of Southwest Hill hydrothermal deposits compared to those at Central Hill (Zierenberg et al., 1994). The north flank of Central Hill (Fig. 3A) is ~400 m wide slump that extends 600 m to the north.

At SESCA (Figs. 16F and 17C), Hill S4 is surrounded to the south and southwest by landslides that heavily scalloped the margins of the hill. Other steep hills at SESCA likely have landslides as well, but high-resolution mapping to illuminate them is lacking.

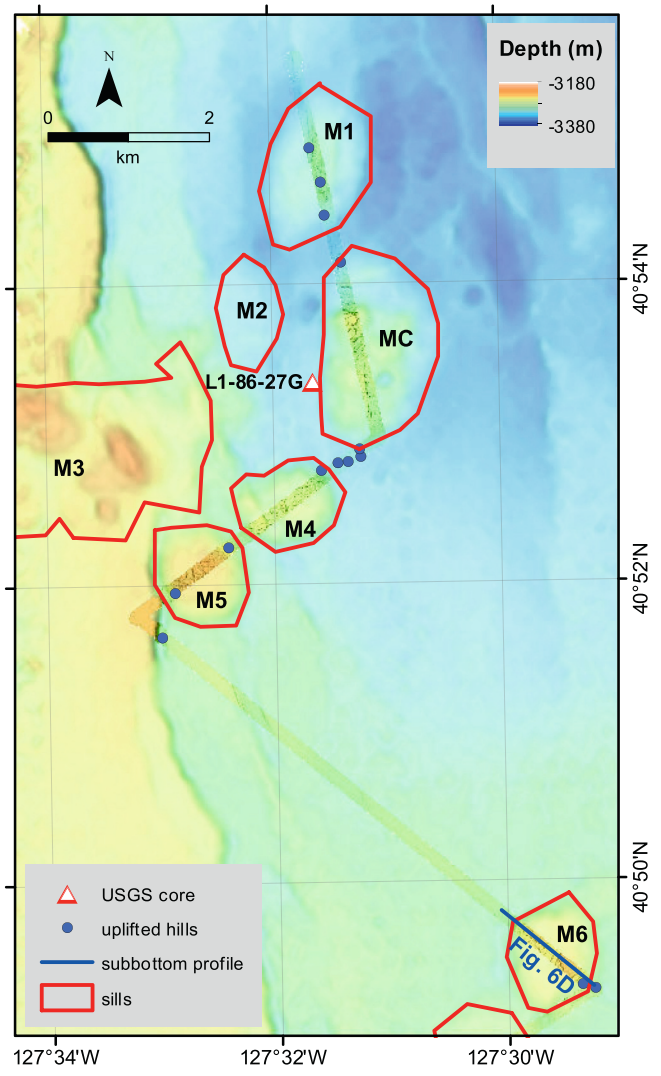

Fig. 13. AUV bathymetric map for MESCA region between NESCA and SESCA on top of faded EM300 shipboard bathymetry. Pockmarks mapped from the limited AUV data are shown as blue dots. Uplifted hills are outlined in red and the SBP in Fig. 6D is shown as a bold dark blue line. The labeled core recovered 25 cm of sulfide breccia under 50 cm of hemipelagic sediment (Zierenberg et al., 1994). (For interpretation of the references to colour in this figure legend, the reader is referred to the web version of this article.)

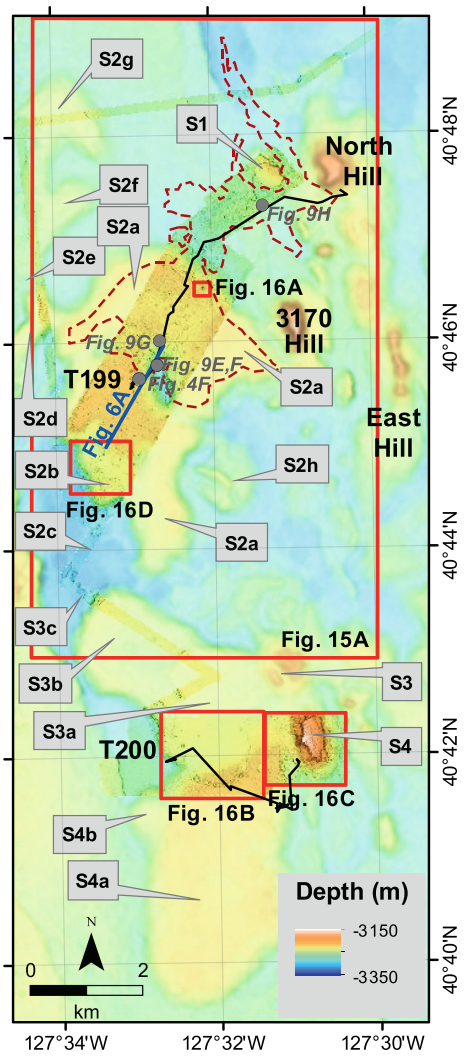

Fig. 14. SESCA AUV 1-m bathymetry superposed on faded ~60 m resolution EM300 ship bathymetry. Tracks for ROV *Tiburon* dives T199 and T200 are black lines. Names of Hills S1 to S8, North, 3170, and East are used in Table 1 and the text. Large red box indicates extent of Fig. 15A. Small red boxes show extents of detailed maps in Fig. 16A to 16D. Lava flow is outlined with red dashed line. Location of chirp line shown in Fig. 6A is bold dark blue straight line whose eastern end overlaps with dive track for T199. Locations of video framegrab images in Figs. 4 and 9 are indicated by gray dots and gray italics font. (For interpretation of the references to colour in this figure legend, the reader is referred to the web version of this article.)

4.2.5. *Hydrothermal cementation of sediment*

Dive T194 explored a region of elevated backscatter (Ross and Zierenberg, 2009) on the floor of the axial graben near 41°7.5′N, 127°33′W (southeastern end of dive T194 track shown on Fig. 18). The axial graben floor was entirely sediment covered with no lava and no hydrothermal deposits cropping out. The source of the higher backscatter remains unknown. The dive, however, continued up the western fault bounding the axial graben and encountered talus at the base of the scarp overlain by >79 m of horizontally bedded, silica-cemented siltstone turbidites. These sediments were lithified and formed vertical to overhanging outcrop (Fig. 4H) and were mistaken to be a stack of dense sills during the dive, as they have pseudo-columnar joint patterns. The silicified sediment crops out below >455 m of basalt flows in the upper portion of the western graben-bounding fault. Most of the talus at the base of the slope consists of multi-m scale blocks of the lithified siltstone, but several small lava fragments from higher in the stratigraphy were also recovered. Such lithification and complete cementation with hydrothermal silica in Pleistocene sediment is unknown elsewhere in the Escanaba Segment and shows the rapidity of hydrothermal alteration in the Escanaba Trough.

4.3. *Northernmost Escanaba Segment lava flows*

The northern Escanaba Segment overlaps with the southern Phoenix Segment to the east. The axial graben of the Escanaba Segment near this overlap is characterized by a cluster of small flat-topped cones explored during ROV dives T196 and T451 (Fig. 18A); most with shallow summit craters. Thirty-one samples from ten of these cones are primitive N-MORBs with 8.34 ± 0.23 wt% MgO and K_2O/TiO_2 of 0.066 ± 0.008 (Tables S1 to S4). The depth of the axial graben at this northern end of the Escanaba Segment is shallower than that of the overlapping Phoenix Segment and the turbidite sediment flowed northeast into the Phoenix Segment so these cones are not surrounded or partly buried by thick turbidite sediment and are buried by sediment thin enough to be

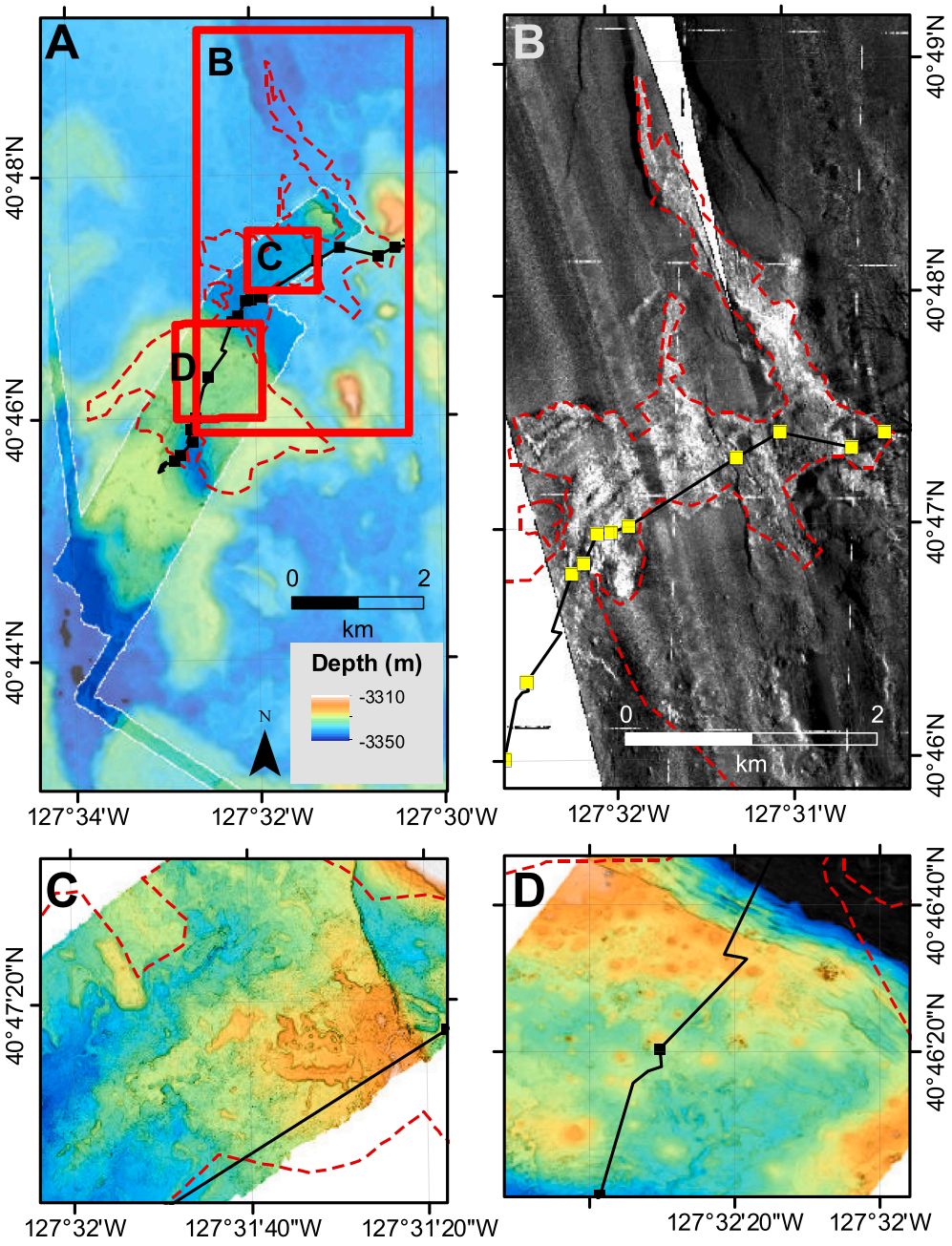

Fig. 15. A). Detailed maps of SESCA lava flow. Red boxes show extents of Figs. 16B to 16D. Dive T199 track is shown as black line and lava sample locations are indicated by black squares. Red dashes indicate extent of the SESCA lava flow. B). Sidescan from Ross and Zierenberg (2009) is shown with dive T199 track and sample locations, as yellow squares. C). The middle portion of the channelized flow that flowed from NE to SW and was disrupted by later faulting and uplift of Hill S2a. D). The NE margin and top of uplifted Hill S2a showing lava on steep fractured slope with open crevices. The top of Hill S3a is characterized by numerous low lava mounds. Features similar to these low lava mounds have not been mapped elsewhere. These low mounds are located near the terminus of a flow emplaced on top of thick flat-lying sediment. (For interpretation of the references to colour in this figure legend, the reader is referred to the web version of this article.)

sampled using 30-cm pushcores. They represent the only axial lavas on the Escanaba Segment that did not erupt through sediment.

To the north of the AUV mapped area at NESCA, a single lava sample collected during *Alvin* dive 2039 at 41°0.5′N, 127°28.5′W is the southernmost E-MORB lava flow on the Juan de Fuca-Gorda Ridge system. The extent of this flow is uncertain, but the sample has K_2O/TiO_2 of 0.25 and the glass contains 7.52% MgO (Davis et al., 1994). This lava is similar to abundant pyroclastic glass shards on the western axial graben fault scarp of the Escanaba Segment sampled by pushcores during MBARI dive T194 near 41°7.5′N, 122°33′W (Clague et al., 2003, 2009; Supplemental Table S4, Fig. 10A). Most shards in the push-cores have E-MORB compositions that are a close chemical match to the E-MORB flow, and are inferred to have erupted there and been transported westward to the core locations. Other shards are N-MORB and T-MORB compositions, similar to lavas erupted on the adjacent Phoenix Segment (Davis et al., 1994).

Lavas erupted on the Escanaba Segment before the formation of the present axial graben are exposed in the fault bounding the axial graben on the west side of the axis (Fig. 18B). Lava flows that crop out in the west fault scarp are T-MORBs with K_2O/TiO_2 of 0.116 to 0.120 and variable MgO of 7.61 to 8.37% (Fig. 10A).

5. Discussion

5.1. Lava flows

5.1.1. Identification and chemistry

The lava compositions allow us to map the extents of the individual flows, thereby enabling identification of where and how magma ascended through the thick sediment to eventual eruption. Density considerations alone indicate that magma should not ascend through the thick accumulation of lower-density sediment, but should spread out

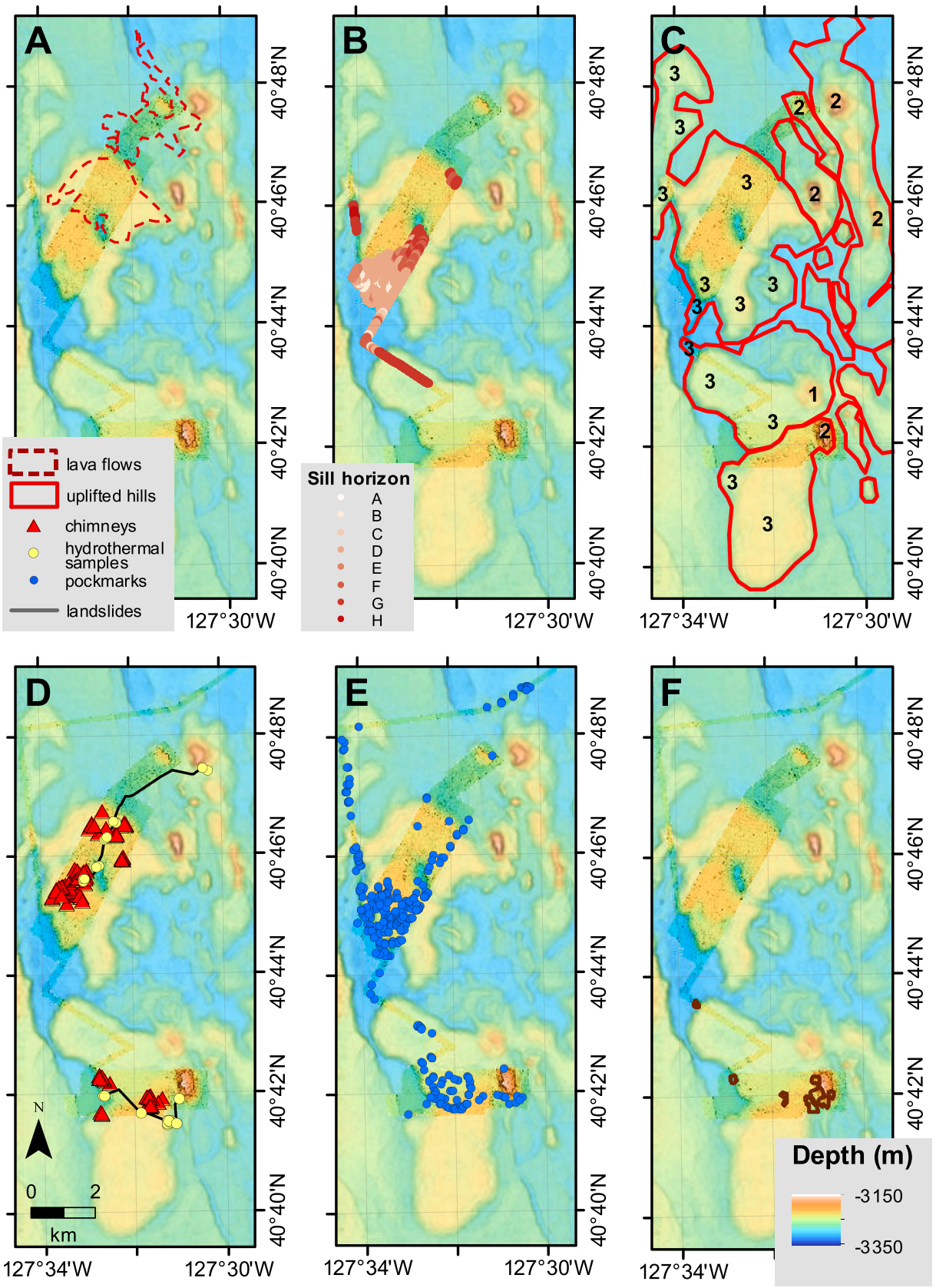

Fig. 16. Maps of AUV bathymetry of SESCA region showing: A) Distribution of SESCA lava flow. B) Distribution of sills <60 m deep (colored dots) imaged in the SBP data. C) Uplifted hills above deeper intrusions; numbers are hill types as in Table 1. D) Inactive chimneys and collected sulfide samples (yellow dots). E) Pockmarks, some in arcuate arrays (blue dots) F). Secondary landslides. (For interpretation of the references to colour in this figure legend, the reader is referred to the web version of this article.)

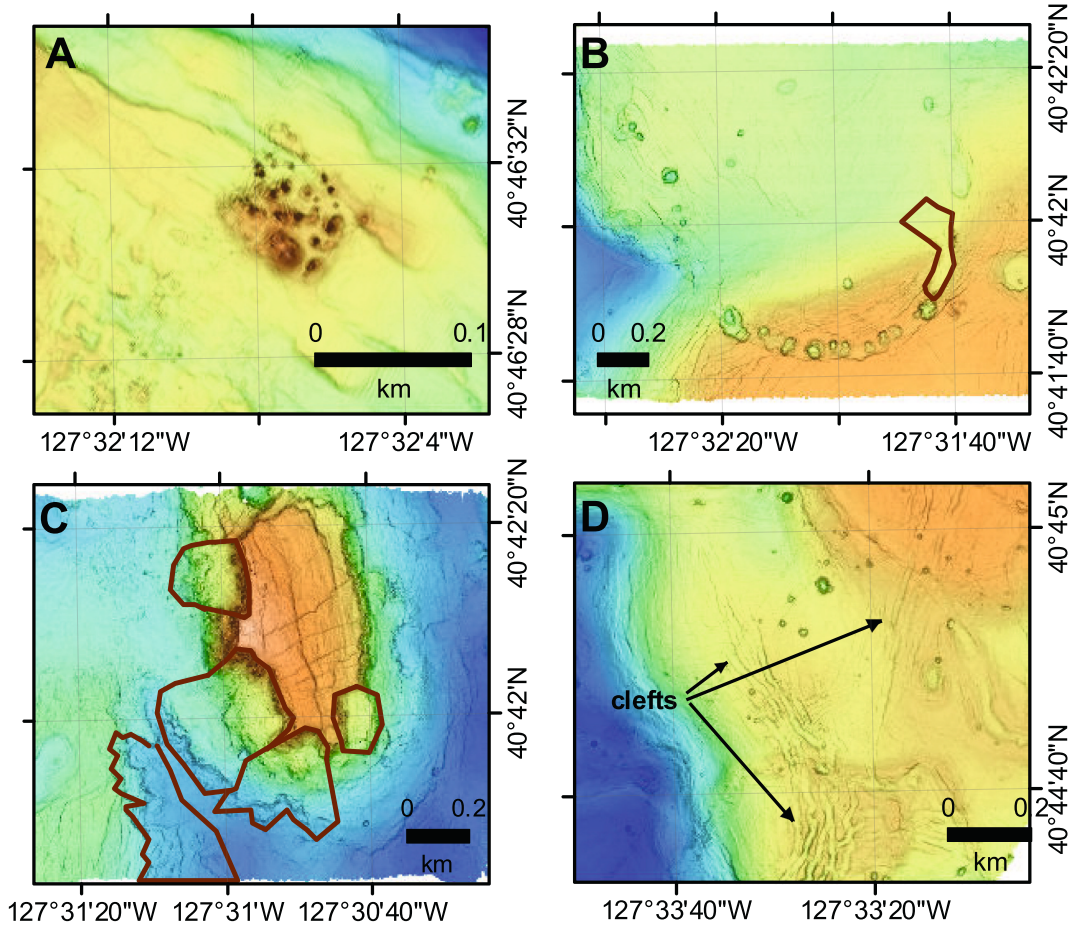

Fig. 17. Maps showing: A) Hydrothermal chimneys in cluster near margin of Hill S2a. Colour ramp is -3240 m in blue and − 3215 m in orange. B) Arcuate array of pockmarks that define the southern margin of Hill S3a. The S3a sill was uplifted with the sediment by the later emplacement of Hill S4a. Colour ramp is −3290 m in blue to −3190 m in orange. C) Hill S4 showing four landslide headwalls creating a cuspate edge around the hill top. The southwestern slide is a broad rotational slump on the NE margin of Hill S4a. Colour ramp is −3280 m in blue and − 3140 m in orange. D) Sediment-filled clefts near margin of sill that uplifted Hill S2a. Colour ramp is −3305 m in blue and − 3195 m in orange. SESCA hill locations shown in Fig. 14. (For interpretation of the references to colour in this figure legend, the reader is referred to the web version of this article.)

within or at the base of the sediment. These density constraints were identified by Lonsdale and Lawver (1980) to model the intrusion of sills that uplifted sediment hills in the Guaymas Basin. However, none of the Guaymas intrusions ascended to supply surface lava flows. In Escanaba Segment, four lava flows erupted through and are on top of the >508 m of sediment filling the axial graben. These lava flows provide an opportunity to assess the conditions that allow magma to ascend through the surrounding lower-density sediment.

Fortunately, each flow has distinctive chemistry and can be mapped unequivocally. The distribution and flow morphologies of the NESCA Young flow show it erupted from a ring fault surrounding Type 2 Hill N12 (Fig. 2), not from the Type 5 Hill N11 (suggested as the source by Ross and Zierenberg, 2009) or from a fault on the NE side of Central Hill (implied by Ross and Zierenberg, 1994). NESCA #2 flow can be traced back to the base of Type 2 Hill N1. This flow has nearly total sediment cover making outcrops rare. The two SESCA flows, as mapped by Ross and Zierenberg (1994), are a single continuous flow based on the new mapping and sampling. The flow erupted from a ring fault at the base of Type 2 North Hill and is assumed to be contemporaneous with the uplift of the hill, as proposed by Ross and Zierenberg (1994) and Zierenberg et al. (1994). Therefore, magma for three of the four lava flows in the sediment-filled axial graben of the Escanaba Segment ascended along ring faults surrounding Type 2 uplifted hills. The unmapped flow sampled during *Alvin* dive 2039 (Davis et al., 1994) may also have erupted from a ring fault around Edifice REX (Zierenberg et al., 1994).

The final mapped lava flow is distinctive in that the magma apparently did not ascend along a ring fault around a Type 2 hill. Flow NESCA #1 is chemically similar to the NESCA Young flow, but is covered by thicker sediment and so is older, and is more fractured and faulted. The broken character of the observed part of the flow is likely related to subsequent uplift of Central Hill, combined with extension across the ridge axis that split Hill N7 and likely Hill N4 (Fig. 2). We propose that NESCA #1 flow ascended along a fissure that mainly bisects three uptilted Type 4 hills near the center of the ridge axis.

The single glass analysis of the top of the laccolith (sample ODP1038I-43-2, Table 2 and Supplemental Table S1) that uplifted Central Hill at NESCA is compositionally similar to the NESCA Young and NESCA #1 lava flows, especially in being a T-MORB (Table 2). The composition is more primitive (Mg# = 65.4) than either flow (Mg#s of 59.5 ± 0.3 and 61.1 ± 0.9) raising the possibility that it might be parental and related to one or the other by crystal fractionation of plagioclase and olivine. However, elevated K_2O/TiO_2 of 0.193 (Fig. 10A) compare to average $K_2O/TiO_2 = 0.150 \pm 0.008$ and 0.141 ± 0.005 (Fig. 10A, Table 2) for the two flows, suggests that this represents a third T-MORB delivered to the NESCA region.

These Escanaba flows range from primitive N-MORB (NESCA #2 flow) to primitive T-MORB (SESCA flow), to moderately evolved T-MORBs (NESCA Young and NESCA #1 flows), to moderately primitive T-MORB (ODP1038I-43-3), to the only known E-MORB (*Alvin* 2039–2, Davis et al., 1994) along the entire Gorda Ridge (Davis and Clague,

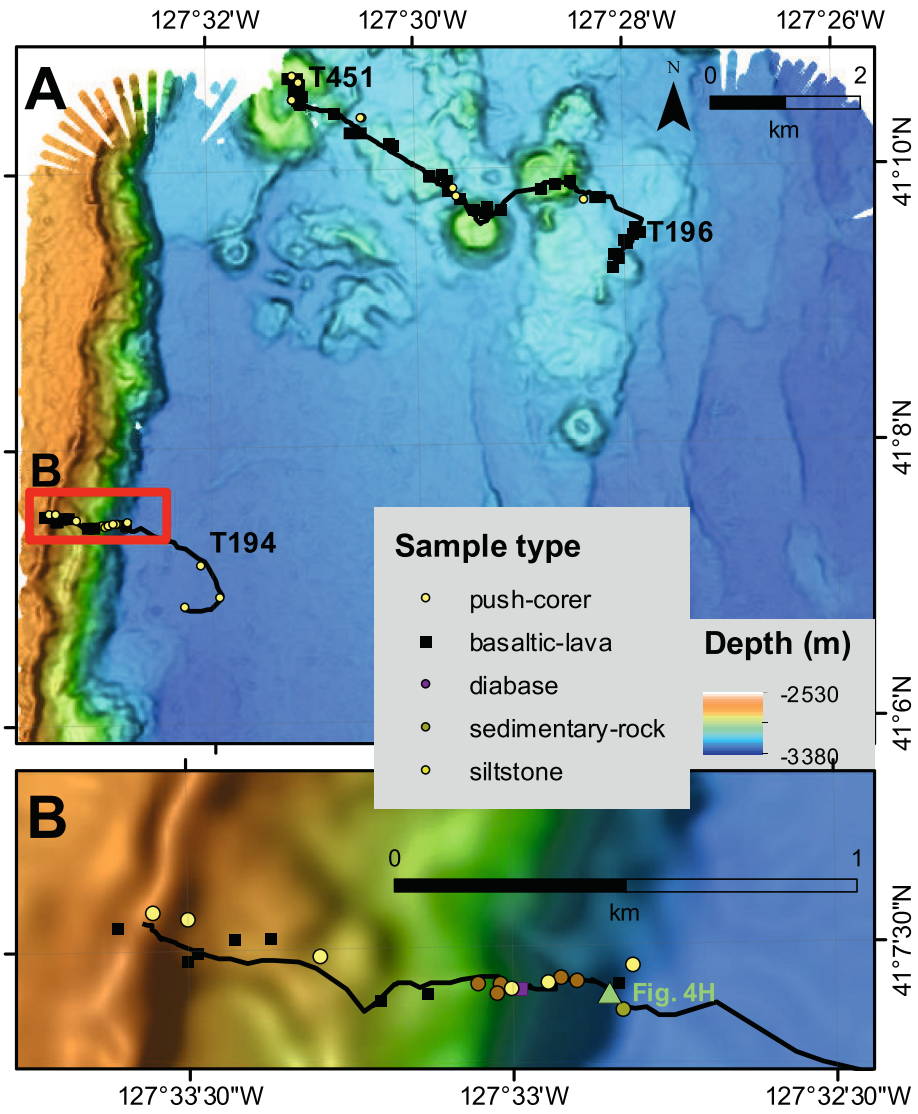

Fig. 18. A) Bathymetric map of northern Escanaba Segment based on Simrad EM300 data showing a cluster of volcanic cones, some with summit craters, and the tracks of *Tiburon* ROV dives T196 and T451 at distal north end of the Escanaba Segment and T194 on the west fault bounding the axial graben. Box shows extent of enlarged map of ROV *Tiburon* dive T194 in B. (B) Dive T194 observed and sampled the western bounding fault of the axial graben after landing in a region of elevated backscatter on the axial floor (Ross and Zierenberg, 2009). No lava flow was observed in the axial graben. The lower 145 m of the normal fault is mainly talus covered and unsampled except for two collected likely talus fragments of basalt and diabase. The talus underlies 87 m of quartz-cemented turbidite sediment (Fig. 4H) that in turn underlies 484 m of basalt flows. The talus covered section is also likely turbidites, making the turbidite unit at least 232 m thick.

1987; Davis et al., 1994; Clague et al., 2020). Their ascent through lower density sediment, to be discussed below, is unrelated to magma temperatures or volatile contents inferred from their major-element compositions or their degree of enrichment or depletion.

5.1.2. Ages of flows

The 3200–3300 m depth of the axis of the Escanaba Segment precludes use of radiocarbon dating on planktic foraminifera (which have dissolved) in basal sediment on top of the flows as done at the summit of Axial Seamount (Clague et al., 2013), Endeavour Segment of the Juan de Fuca Ridge (Clague et al., 2014), or along the Alarcon Rise (Clague et al., 2018). However, relative ages can be inferred from sediment thicknesses on flows and rough absolute ages from sediment thickness and accumulation rates. The NESCA Young flow is the youngest flow and Edifice REX flow north of the mapped NESCA area is the oldest with NESCA #2 and SESCA flows next oldest and NESCA #1 flow older than the NESCA Young flow and younger than the others.

The NESCA Young flow and the Edifice REX flow were accompanied by mild pyroclastic activity that produced abundant shards of glass (Clague et al., 2009, Supplemental Table S4). The maximum amount of glass from the NESCA Young eruption occurs in push cores on top of Central Hill at about 2–3 cm depth and the sediment on top of the NESCA Young flow (Clague et al., 2009) is estimated at about 5 cm, also from push cores. Since sediment is preferentially deposited around hills and eroded, or deposited less efficiently, at the tops of hills, we approximate that ~4 cm of hemipelagic sediment has accumulated since the NESCA Young flow erupted. Karlin and Zierenberg (1994) estimated Holocene sedimentation rates in Escanaba Trough of between 5 and 14 cm/kyr and somewhat less than obtained from ODP site 1038B which yield a calibrated radiocarbon age of 8762 years. at 1.56 m depth, for an average sediment accumulation rate of 17.8 cm/kyr (Zuffa et al., 2000). The larger sedimentation rate of 17.8 cm/kyr from Zuffa et al. (2000) is used for the following age estimates, but if sediment rates were lower, then the estimated ages would be older.

All flows have significantly <1.56 m of sediment on them, so all are younger than this dated horizon (Zuffa et al., 2000). Based on sediment thicknesses on top of flows and the 17.8 cm/kyr sedimentation rates, the NESCA Young flow is ~225-years. old and the SESCA flow, with ~20–30 cm of sediment, is between ~1125–1685 years. old, NESCA #2 flow has a similar amount of sediment to the SESCA flow so is similar in age. NESCA #1 flow is between the NESCA Young and the NESCA #2 flow, but closer in age to the NESCA Young flow. The laccolith that uplifted Central Hill was intruded between eruption of the NESCA Young flow (which surrounds the uplifted Central Hill) and the NESCA #1 flow, which was shattered and deformed by uplift of Central Hill under its southern margin. These relative ages indicate that the Central Hill

laccolith intruded between ~450 to ~1685 years ago, which also indicates that the presently waning hydrothermal venting on Central Hill began at that time. The Edifice REX flow is perhaps several thousand years old (although sediment thickness on top is poorly constrained), because the flow is totally buried by sediment and only exposed along a fault.

To narrow the uncertainty when the lava flows erupted, as well as when the intrusion under Central Hill occurred and hydrothermal activity started will require better measurements of the thickness of sediment on top of the various flows (with the exception of NESCA Young flow), using pushcores or a calibrated rod inserted through the sediment. The more difficult task will be refining sediment accumulation rates during the last 1.56 m of hemipelagic sedimentation.

5.1.3. Flow emplacement

Flows in the axial graben of the Escanaba Segment that erupted on top of sediment are channelized sheet flows (using the map-scale flow nomenclature of Clague et al., 2017). The NESCA Young flow evolved from channelized sheet flows to inflated hummocky flows, to hummocky flows of pillow lava as observed by facies changes away from the vent. Each eruption began with high-effusion rates and the NESCA Young flow evolved during the eruption to lower and lower eruption rates (e.g., Chadwick Jr et al., 2013) with the resultant flows emplaced closer and closer to the eruptive vents (Fig. 7B). Considering the high to moderate rates of eruption inferred from the flow morphologies, the eruptions on Escanaba Segment produced flows with volumes comparable to or greater than the 0.007 to 0.048 km^3 for 1996 N. Gorda, 1993 CoAxial, CoAxial 1981–1990, and 1984 North Cleft (Yeo et al., 2013) or 0.024–0.155 km^3 for the three historical eruptions at Axial Seamount (Clague et al., 2017). The SESCA flow advanced rapidly as thin channelized sheet flows to the southwest with one lobe advancing to the northwest from North Hill (Fig. 19).

Lava flows that erupted from circumferential faults surrounding Type 2 hills are NESCA flow #2 from Hill N1, NESCA Young flow from Hill N12, and SESCA flow from North Hill (Figs. 2 and 14). Magma utilized steeply dipping reverse faults that provide permeable pathways for hydrothermal fluid migration, which results in hydrothermal mineral deposits (Denlinger and Holmes, 1994). At Escanaba, hydrothermal fluids mainly followed the faults used during lava emplacement. Lava flows did not erupt at all Type 2 tall hills, for example Southwest Hill at NESCA, or Hills 3170, East, S3, or S4 at SESCA. These hills were all uplifted by intrusions emplaced deeper than the ~60 m depth imaged by the AUV's SBP. The NESCA flow #1 erupted from a dike that intruded and deformed hills N4 and N7 (Figs. 2 and 12A). Neither of these hills is underlain sills shallower than ~60 m depth (Fig. 12B), either.

The rare lava flows in the sediment-covered Escanaba Trough all appear to have been erupted rapidly, implying significant vesiculation of the magma to decrease its bulk density, but a high vesicle content was not observed in eruption products nor expected for magmas as depleted as N-MORB. Overpressure is likely required for the magma to ascend through sediment that has a density of ~1.9 g/cm^3 (Fouquet et al., 1998a) compared to a magma density of ~2.7 g/cm^3. The same paradox of dense magma ascending through less dense surrounding sediment has been interpreted to indicate that sills and laccoliths are not emplaced at levels of neutral buoyancy within the sediment section (e.g., Thomson, 2007; Thomson and Schofield, 2008; Wilson et al., 2016).

The cones at the north end of the Escanaba Segment (Fig. 18A) are symmetrical small-volume cones that commonly have summit craters or flat tops. Such cones are morphologically similar to cones on the flanks of Hawaiian volcanoes (Clague et al., 2000a) and others mapped along mid-ocean rift zones that are interpreted to be erupted from point sources. The Escanaba cones formed during moderate-effusion rate eruptions that were relatively long-lived, as proposed to form flat-topped much larger near-ridge volcanoes in linear arrays adjacent to mid-ocean ridges (Clague et al., 2000b).

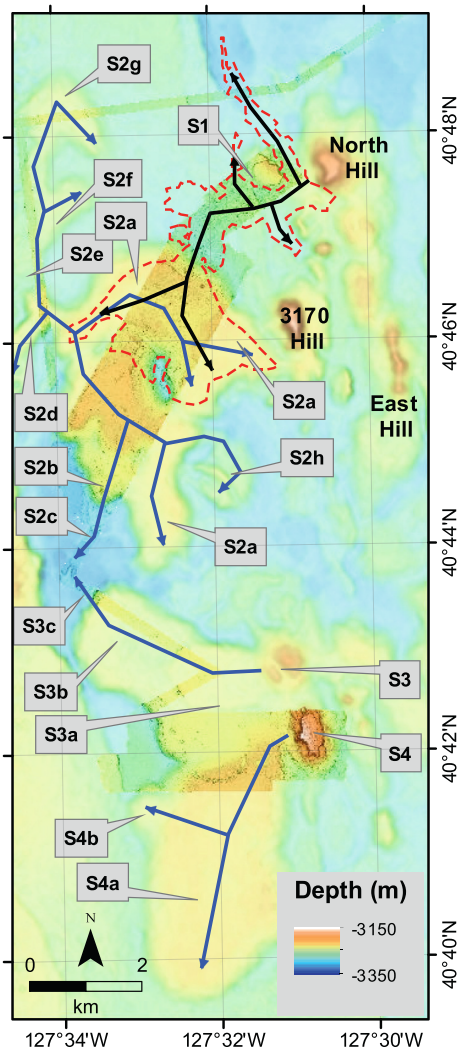

Fig. 19. The SESCA region showing interpretation of the advance (black arrows) of the SESCA lava flow (red dashes) from its inferred source vent at the base of North Hill. Interpretation of the advance of sills that originated from subsurface cone sheets partially surrounding Hills S3 and S4 shown as blue arrows. Sill S2a does not originate from 3170 Hill, which, based on visual observations, is much older than North Hill and the SESCA lava flow (Zierenberg et al., 1994), but sill S2a disrupted the overlying lava flow, so must be younger. (For interpretation of the references to colour in this figure legend, the reader is referred to the web version of this article.)

5.1.4. Compositions of lavas

Gorda-Juan de Fuca Ridge magma genesis has been the focus of numerous petrologic studies (e.g., Cousens et al., 1984, 1995, 2017; Davis and Clague, 1987; Davis et al., 1994, 1998; Michael et al., 1989; Karsten et al., 1990; von Wagoner and Leybourne, 1991; Cousens, 1996; Chadwick et al., 2005, 2014; Stakes et al., 2006; Gill et al., 2016; Clague et al., 2020). The Axial Segment erupts lavas generated by mixing melts derived from the enriched Cobb hot-spot and depleted mantle sources (Chadwick et al., 2005, 2014). Lavas on the northern portions of the ridge system, including West Valley Segment (von Wagoner and Leybourne, 1991; Cousens et al., 1995), Explorer (Michael et al., 1989; Cousens et al., 2017), and Endeavour Segments (Karsten et al., 1990; Gill et al., 2016) are proposed to be formed by mixing melts derived from enriched (FOZO or HIMU sources, using nomenclature of Stracke et al., 2005) and depleted (DMM) mantle sources (Cousens et al., 2017). Previous work on lavas from the northern Gorda Ridge (Davis and Clague, 1987; Davis and Clague, 2003; Rubin et al., 1998; Clague et al., 2020)

and Escanaba Segment (Davis et al., 1994, 1998) also called for a range of depleted to enriched sources. The new lava compositions presented here highlight that enriched mantle sources occur throughout the region, not only from the Endeavour Segment and north. The isotopic data also suggest that the enriched mantle component as far south as Escanaba Segment has HIMU characteristics, since $^{206}Pb/^{204}Pb$ ranges from 18.1 to 19 with most samples >18.4 (Supplemental Table S3, Fig. 10D). The reader is referred to Gill et al. (2016) and Cousens et al. (2017) which both evaluate petrogenesis of lavas in the northeast Pacific.

Analysis of the homogeneity of the Escanaba lavas flows (e.g., Rubin et al., 2001) was not undertaken as analyses were generated in several different laboratories, despite using the same standards for glass analyses. The standard deviations for most elements (Table 2) are close to the analytical precision for those elements for the SESCA, NESCA Young, and NESCA #1 flows, indicative of relatively homogeneous flows. On the other hand, the standard deviations for the nine cones sampled at the northern end of the Escanaba Segment are higher for most elements than the analytical precision, indicating that the cones did not erupt homogeneous lavas, as might be expected for a suite of monogenetic cones.

The nearly identical compositions of the NESCA Young flow and the older NESCA #1 flow (see averages and standard deviations in Table 2), and the similar T-MORB characteristics of the Central Hill laccolith (sample ODP1038I-43-3 in Table 2 and Supplemental Table S1) demonstrate that magma production and evolution are not random along the ridge. A similar relation was observed at the Northern Gorda Ridge where the lava flows erupted in 1996 are compositionally similar to older underlying flows (Clague et al., 2020) in their degree of depletion and their degree of crystallization prior to eruption. That a location along a ridge produces such similar lavas over several hundreds to thousands of years indicates that at least some mantle heterogeneities are long lived, and presumably shaped more like vertical filaments or streaks (e.g., Graham et al., 2006) than blobs and that residence times in subaxial magma reservoirs are relatively uniform between eruptions.

5.2. Intrusions

5.2.1. Emplacement of intrusions

The emplacement of sills and laccoliths have been discussed at length in the literature (e.g., Corry, 1988; Elliot and Fleming, 2018; Hunt, 1953; Leaman, 1975, 1995; Seymour et al., 2007; Thomson, 2007; Thomson and Schofield, 2008; Wilson et al., 2016). Three main models have been proposed and are illustrated in Fig. 1 in Schmiedel et al. (2017a): 1) simultaneous growth by radial expansion and increasing thickness, 2) 2-stage growth by radial expansion at constant thickness followed by inflationary increase in thickness, and 3) bulldozing by radial growth at constant thickness. The various types of hills described here provide support for all three models. Type 1 dome-like hills such as Central Hill at NESCA and hills at MESCA overlie deep domed laccoliths that grew by simultaneous expansion and thickening of the laccolith. Type 2 hills overlie deep inflated laccoliths that punched through the sediment. Type 3 hills grew by sills bulldozing within the sediment sequence and forming monoclinal folds in the overlying sediment (e.g., Koch et al., 1982). Type 4 and Type 5 hills are modified surface lava flows but appear to have grown by 2-stage growth of intrusions shallower than uplifted the Type 1 and 2 hills.

There is a well-documented, although rough, relation between the thickness of large mafic sills and laccoliths and their lateral extent (Bunger and Cruden, 2011), in which both become thicker the larger their extent, but large mafic sills are one-to-two orders of magnitude thinner than laccoliths of similar extent. Unless an uplifted sediment hill is heavily modified by secondary landslides that removed the top of the hill, the heights of the hills provide a rough measure of the thicknesses of the sills or laccoliths that uplifted the hill (e.g., Galland, 2012). Hill heights range from ~5 m to over 150 m, so the sills and laccoliths are inferred to have roughly the same range in thickness. The heights of the hills are not straightforward to measure as the depth varies around the margins of the hills for a variety of reasons including pre-existing topography, adjacent emplacement of subsequent sills, and deposition of landslide debris. In Table 1, margins modified by such processes were avoided, but the heights listed are still subject to such geological errors. Type 3 hills generally have disparate width compared to lengths, so the errors in estimating extent is increased. The Escanaba sills and laccoliths, however, plot along the correlation lines proposed by Bunger and Cruden (2011) and extend their correlations to somewhat smaller thicknesses and extents for both sills and laccoliths. Likewise, the estimated volumes of the Escanaba intrusions are also relatively small, certainly in comparison to sill and laccolith intrusions in the geologic record.

The sediment thickness above the intrusions or depths of the intrusion can be quantified for shallow sills imaged in the AUV SBPs using the depths of the A-I series of reflectors, and at Central Hill by ODP drill core. The smaller hills, with the thinnest sills and least uplift, are among the shallowest: Type 3 hills in the northern part of NESCA and at SESCA include sills emplaced at shallow depths that truncate the reflectors at depths as shallow as reflector A (at ~5 m depth) to reflector H (at ~48 m depth, Figs. 12B and 16B). The sills at NESCA Hills N3c and N3d, and elsewhere are about 3 times as deep as the sill thickness inferred from the height of the uplifted hill. This simple relation of sill depth (from the SBPs) being equal to ~3 times sill thickness (from the height of uplifted hills) is not as robust at SESCA, where some Type 3 sills (S2a, S2b, S3b, and S3c) appear to be shallower than expected based on the height of the uplifted hill (Table 1).

The taller hills, uplifted therefore by thicker intrusions, all have sill depths deeper than the AUV chirp sonar penetration depth. The ODP drill cores at Central Hill sites 1038G, 1038H, and 1038I (Fig. 3A), encountered and recovered basalt that provides a single data point for a deeper, thicker laccolith. Basalt was first encountered at 135.2 to 161.1 mbsf in the three holes and again at 403.2 mbsf at site 1038I (Fouquet et al., 1998c). The upper buried basalt flow is present or imaged on 4 single channel seismic lines and extends at least 5 km N-S (Zierenberg et al., 1994), and was encountered in the three site 1038 drill holes that penetrate deeper than 114.5 mbsf. This shallower basalt, encountered at ~135 to 161 mbsf at sites 1037G, H and I is too thin (<2 m thick, Fouquet et al., 1998b) to have uplifted Central Hill, which stands ~120 m above the regional depth, and most likely is a surface flow erupted about 16 kyr ago (interpolated age from radiocarbon age data in Zuffa et al., 2000) before Central Hill was uplifted by the laccolith whose top is interpreted to be at 403 mbsf. The 120 m height of the hill is difficult to measure as regional depths vary around the hill, and 120 m may be a maximum thickness of the laccolith. The apparent height of Central Hill implies intrusion along the basalt/sediment interface at ~523 mbsf, slightly deeper than the basement depth determined at nearby reference site 1037B. The ratio of intrusion depth to intrusion thickness is 3.4, so similar to that determined from Type 3 hill heights and SBP data. This ratio of sill depth to thickness of ~3–3.4 may be related to the density contrast between lava in the intrusions and the surrounding sediment.

At SESCA, Type 3 Hills S3a-3c and S4a-4b appear to have originated around Type 2 punched laccolith Hills S3 and S4 (Figs. 14 and 19). The directions these sills advanced within the sediment is illustrated in Fig. 19. In contrast, sills uplifting Hills S2a-2h have no identified source location (Fig. 15B) since adjacent Type 2 Hill 3170 is older than North Hill (Zierenberg et al., 1994), the known source of the SESCA lava flow, which is uplifted and disrupted by the inflation of S2a (Fig. 15D). Type 3 hills show the complexity of sill advancement as the sill under Hills S2a-2h advanced in multiple directions. Outcrops of sills on land commonly form stacked sequences (e.g., Leaman, 1975, 1995; Seymour et al., 2007; Elliot and Fleming, 2018), but there is only a single example of overlapping sills. This example at SESCA shows Hill S3a and a semi-circle of pockmarks around its margin uplifted by a second thicker, deeper sill that uplifted Hill S4a (Fig. 17B).

Most of the sills shallow enough (<~60 m depth) to be imaged in the chirp data occur under broad, low-relief Type 3 hills (Figs. 9F and 16B).

Most of the shallow imaged sills also advanced along a single sediment horizon for up to several km, but some crosscut reflectors.

5.2.2. Intrusion shapes and bounding structures

The uplifted hills provide information about the shape of the intrusion that uplifted the hills (e.g., Galland, 2012) despite those that uplifted all Type 1, all Type 2, and most Type 3 sediment hills being emplaced too deep to be imaged with the AUV chirp sonar. Type 1 hills, like Central Hill, are dome shaped and reflect dome-shaped laccolith intrusions that uplifted them (see Fig. 1 in Schmiedel et al., 2017a). At Escanaba Trough these are generally nearly circular to slightly ellipsoidal in shape, with their thickest part near the center. The laccoliths under a few Type 1 hills, such as Central Hill, inflated to the point that they grade into Type 2 hills and their margins or some of their margins become small-offset reverse faults more typical of Type 2 hills.

Some of the tallest hills are Type 2 hills, such as N1, N12, and Southwest Hill at NESCA (Fig. 2) and North Hill at SESCA (Figs. 14 and 16C). These are piston-like uplifts (punched laccoliths, see Fig. 1 in Schmiedel et al., 2017a) that are either circular (such as N12) or elongate parallel to the ridge axis (such as Hill N1 and Southwest Hill). These hills are surrounded by steeply dipping reverse faults whose headwalls collapsed in multiple landslides (Figs. 12F and 16F). Intrusions that uplifted all Type 2 hills are too deep to be imaged in the SBP. The eruption of lava from the bounding faults at several of these Type 2 hills indicates that these thick laccoliths are most likely the deepest of all the intrusions, although their basal depth is limited to the ~546 m of sediment drilled at ODP reference site 1037 (Fouquet et al., 1998b) and their thicknesses are <140–150 m (the height of Southwest Hill, the tallest Type 2 hill). These sills have small lateral dimensions relative to their thickness and form by vertical inflation with little lateral advance as the sill puffs up. The process is analogous to inflation of pahoehoe flows (Hon et al., 1994) or to the formation of thick inflated sheet flows on the seafloor, such as mapped in the central caldera on Axial Seamount (Clague et al., 2013). Denlinger and Holmes' (1994) model was used to construct cross sections by Morton and Fox (1994) of the uplift of Central Hill. The cross sections were intended to show how Type 1 Central Hill was uplifted, but the model is more appropriate for Type 2 Hills N1, N12, and Southwest Hill at NESCA and North, 3170, East, and S4 at SESCA.

Type 3 hills overlie sills that range from too deep to image with the AUV SBP system (>~60 m) to only a few m below the sediment surface. These sills expand laterally by bulldozing the sediment to form monoclines above their advancing margins and then inflate in place (Wilson et al., 2016). Most of these have the form of thick, flat-topped lava flows. At several of these Type 3 hills, such as N3, North, S3 and S4, after a period of inflation, the sill again advanced laterally by climbing up low-angle faults in the sediment surrounding the initial sill. This process is illustrated in Fig. 20 that shows a constructed cross section through the southern half of Hill N3 to Hill N3d (shown in map view in Fig. 11). The sea floor is the profile determined from the high-resolution AUV bathymetry and the sill thickness is the height above a regional depth, and the sill depth is calculated as three times the thickness of the sill. Another example of climbing sills is observed in the southern part of SESCA (Figs. 14 and 16B). The SBP image the top of the sill under Hill S3b at horizon H, but not the top of one under Hill S3a, so the more distal Hill S3b is both thinner and shallower than the more proximal Hill S3a. To the northwest of Hill S3b, even thinner and shallower sills S3c advanced to the north-northwest, but the sills are not well defined because the area is incompletely mapped by a single zig-zag AUV line. These examples of climbing sills produce the classic saucer shape observed in many sills (e.g., those imaged in 3-D seismic surveys by Thomson, 2007; and Thomson and Schofield, 2008).

The margins of sills in Escanaba are simple in contrast to some sills described on land. Pollard et al. (1975) describes complex fingers of lava at the margins of a sill fed from the Shonkin Sag laccolith. Another example is the Golden Valley sill in the Karoo Basin described by

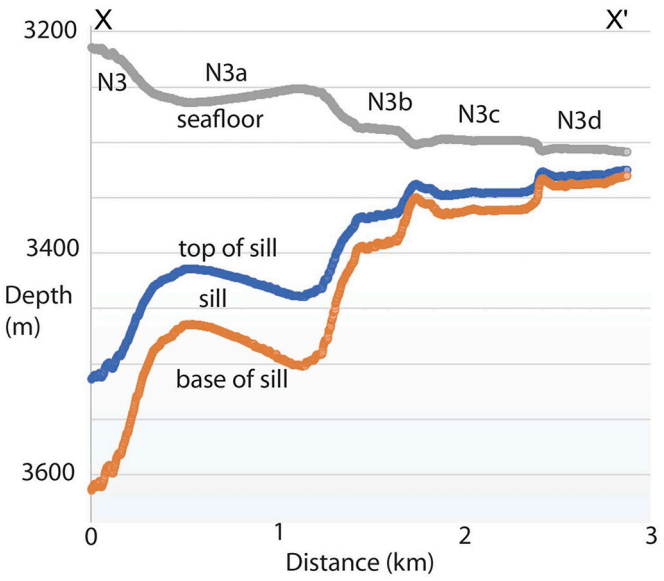

Fig. 20. Interpretation of the structure of the sill under Hill N3 (Fig. 11). The height of the hills above regional depth was used as a measure of sill thickness and depth to the top of the sill was determined from SBP data for depths of the upper surface less than ~60 m for sills under Hills N3c and N3d. The depths to the top of deeper (central) parts of the sill (Hills N3, N3a, N3b) were calculated using a ratio of sill depth to sill thickness of 3 as discussed in the text.

Schofield et al. (2010) who attributed the complex fingered margin to flash boiling of host sediment pore water. The Escanaba sills are at water depths greater than the critical point of seawater where flash boiling should not occur and is consistent with the lack of such complex sill margins in the Escanaba Segment.

Sills and laccoliths commonly occur in stacks and considerable effort has gone into trying to determine if shallower intrusions predate or postdate deeper intrusions (e.g., Hobart Sills in Tasmania, Leaman, 1975, 1995; Seymour et al., 2007: or the Ferrar Large Igneous province in Antarctica, Elliot and Fleming, 2018; or sills in the Faeroe Scotland Basin, Thomson, 2007). Shoaling or deepening intrusion levels inform whether neutral buoyancy is the primary control on sill or laccolith depth. In Escanaba Trough, intrusions, mostly of nearly aphyric mid-ocean ridge basalts with similar densities can occur at depths below the seafloor ranging from around 500 m to several m, supporting the view that other factors such as lithologic or rheologic differences between ductile shale and more brittle sandy layers control depth of intrusion, as argued by Thomson (2007) and explored experimentally (e.g., Kavanagh et al., 2006; Scheibert et al., 2017, and Schmiedel et al., 2017b), among others. In addition, variations in the intrusion overpressures may result in irregular distribution of sill depths with respect to age. The graded turbidites that comprise the sediment section in Escanaba (Zuffa et al., 2000; Normark and Serra, 2001) provide a wide range of sediment lithologies with different physical properties. The shale layers are likely to be the ductile horizons where sills and laccoliths spread laterally. In Escanaba, there are only a few examples where sequence of intrusions can be determined. At SESCA, the uplift of Type 2 North Hill by a deep laccolith predates the emplacement of shallower Type 3 lobate sills nearby. Likewise, the uplift of Type 1 Hill S3 by a domed laccolith predates the emplacement of Type 3 shallower sills under Hills S3a, S3b and even shallower thinner sills under Hill S3c to the northwest of Hill S3. At NESCA, the domed laccolith that uplifted Central Hill predates the deep punched laccolith that uplifted Hill N12, as the NESCA Young flow erupted from the circumferential faults around Hill N12 surround Central Hill (Figs. 3A and 7B). The observations generally support the concept that emplacement proceeds from deeper to shallower, as inferred by Leaman (1975, 1995) for the Hobart sills.

5.3. Secondary effects of intrusions

5.3.1. Distribution of hydrothermal deposits

Denlinger and Holmes (1994) inferred hydrothermal fluids migrated to the surface along permeable fault zones on steeply dipping reverse faults above the edges of Type 2 hills above domed laccoliths and precipitated hydrothermal sulfide deposits at the sea floor. Exploration on Southwest and N8 Hills at NESCA and North and 3170 Hills at SESCA (Zierenberg et al., 1994) show the distribution of hydrothermal deposits on the steep slopes around the hills as predicted by their model. However, the new map coverage shows that chimneys are not restricted to such marginal sites, but occur above deeper, thicker intrusions (Figs. 12D and 16D). The Type 1 hills such as Central Hill and Hill N6 also have more widely distributed chimneys inconsistent with fluid migration only along steeply dipping reverse faults. At Central Hill the distribution of chimneys is consistent with widespread doming and cracking of the sediment (Fig. 3A) allowing escape of fluids from hydrothermal circulation cells overlying the laccoliths. Near the margin of Guaymas Basin in the Gulf of California, chimneys occur on the edges of a pockmark to form deposits at the Ring Vent (Teske et al., 2019). This juxtaposition of hydrothermal chimneys and pockmarks has not been observed at Escanaba Segment, although fluids that support chemosynthetic bacterial mats and clams are discharged in the inner slope of a large pockmark on the north side of Central Hill (observed on ROV dive D83, Fig. 2).

The deposits at the margins of uplifted Type 2 hills (such as Southwest Hill, North Hill, Hill 3170, and East Hill; Zierenberg et al., 1994) and on top of Type 1 hills, such as Central Hill (Fig. 4E), are predominantly polymetallic Cu- and Zn-rich. Von Damm et al. (2005) argued that hydrothermal fluids at Escanaba have undergone phase separation by condensation of a brine at temperature in excess of the supercritical point of seawater during interaction with basaltic rocks. Interaction with basaltic basement is also required based on the isotopic composition of Li and B (James et al., 1999) and He and C (Ishibashi et al., 2002). High concentrations of alkali metals, B, and thermogenic gas, including methane, are clear indications of interaction of the fluid with sediment (Campbell et al., 1994; Von Damm et al., 2005). Elevated levels of elements such Pb, As, Sb, Bi, and Pb isotopic ratios in massive sulfide are consistent with a sedimentary source in addition to basalt (Zierenberg et al., 1993; Koski et al., 1994). Magmatic degassing of volatile metals (Rubin, 1997) could produce some, but not all, these metal enrichments and should not fractionate Pb isotopes. The model for Escanaba Trough polymetallic sulfide deposits is similar to those proposed for Middle Valley (e.g. Zierenberg et al., 1998; Cousens et al., 2002) or Pescadero Basin (Paduan et al., 2018), which envision circulation of high temperature hydrothermal fluid in the relatively more permeable basaltic basement followed by fluid-sediment interaction in a hydrothermal upflow zone. The deeply emplaced laccoliths that uplift Type 1 and Type 2 hills appear to be able to focus fluid up-flow from the igneous basement and to provide a sufficient opportunity to leach metals from the sediment column above the deep sills.

In contrast, deposits on the margins of and on top of Type 3 hills (e.g. Hills S2a, S3a, and perhaps S4a) are predominantly small pyrrhotite-rich chimneys (Figs. 4F and 17A), often associated with hydrothermal tar. These more isolated chimneys may form by thermally-induced flushing of reduced pore fluids from the thin sediment overlying the sills, mobilizing iron, reduced sulfur and thermally altered organic matter from the sediment, but does not tap into higher temperature (and lower pH?) fluids circulating in the underlying igneous crust that are capable of transporting significant quantities of base and precious metals. We caution that many of the recently mapped chimneys remain unsampled, so this apparent bimodal distribution of sulfide types remains speculative. This correlation, if it is verified by more thorough sampling of the many newly mapped chimneys, suggests that deeper and thicker laccoliths support longer-lived and higher temperature hydrothermal fluid circulation than thinner and shallower sill-driven systems.

A key question about hydrothermal activity is the duration of active venting. At NESCA, the only known active chimneys are on Central Hill. The uplift of Central Hill by an underlying laccolith is constrained to have been before emplacement of the NESCA Young flow, since the flows surround the hill (Fig. 2). On the other hand, uplift of Central Hill shattered the NESCA #1 flow just north of Central Hill, indicating that the NESCA #1 flow was present when Central Hill was uplifted. It therefore seems most likely that the sill beneath Central Hill that provides the heat to drive the still-active discharge of hydrothermal fluids has been active for at least 225 years (the minimum age of the NESCA Young flow) and more likely for several times that long based on the ~1685-year age of the disrupted NESCA #1 flow.

The numerous chimneys on Central Hill could all have begun to form as the laccolith intruded and uplifted the hill and have died out one by one over the ensuing years as the laccolith cooled and supported less convective cooling. On the other hand, there may only be a few active chimneys at any time, and as their stockwork infills with sulfide mineral precipitates, new chimneys form at nearby locations as fluids find a path of lower resistance to the surface. Ra—Ba dating of barite-bearing chimneys might clarify which model is correct, or if the correct interpretation is between these two extremes.

Other observed hydrothermal deposits, such as those at SESCA, were inactive, which suggests that the heat from intrusive laccoliths and sills has been extracted in the case of intrusions related to NESCA #1 flow or to SESCA. The sampled chimneys and deposits at SESCA are deeply weathered, which is consistent with their having become inactive perhaps several thousand years ago.

5.3.2. Distribution and formation of pockmarks

Pockmarks are commonly observed in a wide variety of geologic settings and are particularly abundant in areas of methane venting from submarine sediments. The abundant pockmarks observed at SESCA and NESCA have similar distribution to that of shallow sills imaged with the AUV chirp sonar system and to the taller hills uplifted by emplacement of laccoliths. The pockmarks are therefore formed by processes related to emplacement of intrusions, as also noted by Karaket et al. (2021) for pockmarks seismically imaged adjacent to strong reflectors interpreted as sills in the New Zealand Basin. Rare pockmarks in Guaymas Basin (Teske et al., 2019), on the Pescadero Transform (Clague et al., 2018), and in Pescadero Basin (Paduan et al., 2018) are associated with hydrothermal activity and have been inferred to have formed during emplacement of sills/laccoliths. Similar pockmarks, though less common, also occur along the Pescadero Transform near sill-uplifted sediment hills in the southern Gulf of California (Clague et al., 2018), and were also observed in the Guaymas Basin in high-resolution mapping data (Teske et al., 2019, 2021; Ondréas et al., 2018).

Several hypotheses have been proposed for the origin of pockmarks, but most invoke the advection of fluids and(or) gases through unconsolidated surface sediment. Similar pockmarks are generally attributed to venting of biogenic or thermogenic methane, pore fluids, fresh water, or oil from sediment (e.g., King and MacLean, 1970; Nelson et al., 1979; Hovland et al., 1984; Berndt, 2005; Judd and Hovland, 2007). Paull et al. (2015), based on comparable AUV mapping data, showed an array of landforms produced by shallow methane venting from gas hydrates, but pockmarks are not among the landforms produced. Expulsion of fluids aligned along sill margins (e.g., Ring Vent in Guaymas Basin, Teske et al., 2019) is another mechanism postulated to form pockmarks.

The abundant pockmarks on the Escanaba Segment (Figs. 12E and 16E) have no upraised rims of expelled sediments, and therefore did not form by vigorous gas expulsion, although at least some of the larger pockmarks include chemosynthetic clam beds indicative of fluid flow. The low contents of buried carbon in Escanaba sediment (Fouquet et al., 1998c) is one reason that methane is not produced abundantly. Hydrothermal vent fluids at Escanaba Trough are still enriched in methane relative to seafloor hydrothermal system developed at bare-rock spreading centers (Campbell et al., 1994; Von Damm et al., 2005;

Paduan et al., 2018). Elevated methane and hydrothermal hydrocarbons have been well documented at Escanaba Trough (Kvenvolden et al., 1994). However, saturation of methane gas to form bubbles is extremely unlikely in this setting, and bubble plumes have not been observed exiting the seafloor. At the depth of the Escanaba Trough, methane hydrates are stable up to approximately 20 °C (Tishchenko et al., 2005; Wallmann et al., 2012), but bottom simulating reflectors indicative of gas hydrates are absent. The extrapolated end member methane concentration in 220 °C hydrothermal fluid is 16.5 mmole/kg (Von Damm et al., 2005). Pore fluid methane concentrations and isotope ratios are similar to those measured in hydrothermal vent fluids (Ishibashi et al., 2002), and are well below concentrations needed to saturate gas bubbles or methane hydrate at seafloor pressures. The sediments filling Escanaba Trough contain <1% organic carbon which is dominantly refractory kerogen derived from terrigenous plant material (Kvenvolden et al., 1994). Methane in head space gas samples from the upper 100 m of sediment cored at Site 1037, a reference site drilled for comparison to the hydrothermally active areas, is below detection limits (Fouquet et al., 1998c). Head space gas samples from Site 1038 where hydrothermal activity is ongoing have elevated, but relatively low concentrations of thermogenic methane in near surface (<100 m) sediment, consistent with the low abundance and refractory nature of the terrigenous organic matter in Escanaba Trough sediment (Fouquet et al., 1998a). Pockmark formation at Escanaba Trough does not appear to be caused by methane discharge. Alternatively, we propose that compaction due to pore space reduction caused by thermally driven fluid advection is the most reasonable explanation for their form and distribution in Escanaba Trough.

The abundance of pockmarks associated with intrusions in Escanaba Segment, especially to Type 3 uplifted hills above shallow sills (Fig. 17B), suggests that their distribution is more widespread than previously thought. In Escanaba, their abundance likely reflects the very low recent sedimentation rates that have yet to fill and bury inactive pockmarks, compared to those in the Gulf of California, where sedimentation rates are high and older pockmarks are rapidly filled.

5.3.3. Post-uplift instability of hills

The uplift of hills along steep reverse faults leads to creation of slopes that can exceed the angle of repose of 15–30° for water-saturated sand (Beakawai Al-Hashemi and Baghabra Al-Amoudi, 2018). These oversteepened sediments fail along these faults as debris flows or avalanches. This style of uplift in Escanaba Segment accompanies emplacement of domed and punched laccoliths that form Type 1 and Type 2 hills, respectively (e.g., Fig. 17C). Less commonly, small landslides originated on the margins of Type 3 hills (Fig. 16F) above shallower thinner sills, which had inflated to produce low-angle reverse faults on their margins. The landslides also attest to the unconsolidated nature of the turbidite sediment. There are several landslides that provide stratigraphic control on the sequence of uplift of sediment hills. An example is slide debris from Southwest Hill at NESCA that was then uplifted when Central Hill uplifted as the laccolith intruded.

5.3.4. Silicification of turbidite sediment

Silica-cemented turbidite sediment was observed and sampled during dive T194 on the western bounding axial graben fault near the north end of the Escanaba Segment (Figs. 4H and 18B). Similar deposits were not recovered during ocean drilling in Escanaba Trough at Sites 75 (Vallier et al., 1973), 1037 or 1038 (Zierenberg and Miller, 2000). However, drilling on the west and east flanks of the Bent Hill Massive Sulfide deposit at sites 1035A and 1035D in Middle Valley recovered similar cemented turbidite sands that were weakly veined with pyrrhotite (Zierenberg and Miller, 2000). They proposed that the silica cemented turbidite sands formed an impermeable caprock that ponded hydrothermal fluid underneath and facilitated silica deposition during slow conductive cooling of the silica saturated fluids (Janecky and Seyfried, 1984). Such conductive cooling at the Bent Hill Massive Sulfide deposit also led to precipitation of isocubanite solid solution, the least soluble of the sulfides in the deposit. The similarity of the silica-cemented turbidite sands in the northern Escanaba Segment to those at Bent Hill suggests that Cu-rich replacement mineralization may also underlie the silicified caprock observed during dive T194.

6. Conclusions

High-resolution AUV bathymetry and closely spaced SBP data, accompanied by observations and sampling during 16 ROV dives support a new analysis of the distribution and emplacement of lava flows and sills in the Escanaba Segment of the Gorda mid-ocean ridge. The high-resolution data show the intimate association of hydrothermal chimneys, sediment deformation and landslides, maturation of hydrothermal petroleum, and pockmarks to shallow sill and deeper laccolith emplacement. Four of five mapped lava flows erupted through ring faults surrounding sediment hills uplifted by intrusion of deep laccoliths. For the aphyric MORB lavas of the Escanaba Trough, magmatic overpressure likely contributes to rise of the magma through lower density hemipelagic sediments.

The relationship between depth and thickness of the intrusions can be extracted for many of the sills because sediment accumulation after intrusion emplacement has been low enough that the height of the uplifted hills is a proxy for the sill or laccolith thickness. Most of the shallow sills are at subbottom depths roughly three times the thickness of the sills, as is the deep laccolith underlying Central Hill that was drilled at ODP site 1038. The type of sulfide deposits produced, polymetallic or pyrrhotite-dominant, appears to be a function of the depth and thickness of the intrusion, which therefore correlates with the length of the fluid pathway through the overlying sediment. The polymetallic sulfide deposits are considerably larger and formed from protracted periods of focused fluid flow, whereas the isolated pyrrhotite chimneys may be sourced entirely from sediment pore fluids mobilized above shallowly emplaced sills. Active venting at NESCA's Central Hill began between ~225 and ~1685 years ago, the inferred ages of lava flows that bracket when the laccolith that uplifted the hill was intruded. Such long duration of active venting contrasts with much shorter-lived activity on basalt-paved portions of the mid-ocean ridge system. The inactive chimneys at SESCA are consistent with the far greater age of volcanic, and presumably intrusive activity there. It is tempting to compare intrusions at the Escanaba Trough with those observed in continental areas. There are important differences such as complexity at sill margins at low pressures (e.g. continental surfaces) that may result from pore fluid boiling. High pressure due to the great depth of the Escanaba Segment (>2936 m, the critical point for seawater in the northeast Pacific, Clague et al., 2003) limits seawater heated by magma to supercritical fluids. Lacking a vapor phase, the sill margins are much less complex.

Data availability

The AUV data have been deposited in the Marine Geoscience Data System and are available online at https://www.marine-geo.org/tools/search/entry.php?id=EscanabaTrough_MBARI (Clague et al., 2021). The geochemical data, in addition to being complete in the Supplemental Tables, are posted in PetDB at https://search.earthchem.org.

Funding

RAZ and JM were supported by a grant from NOAA/NURP. The ship operations, post-cruise data processing, most geochemical analyses, and salaries for DAC, JBP, DWC, and ASD were supported by annual grants from the David and Lucile Packard Foundation to MBARI.

Author statement

None of the authors has conflicts of interest nor stands to gain financially from this work.

Declaration of Competing Interest

The authors declare that they have no known competing financial interests or personal relationships that could have appeared to influence the work reported in this paper.

Data availability

All data are publicly posted and available, or are included in the paper.

Acknowledgements

A study of this magnitude does not happen without contributions from many more people than become coauthors. This study is built on the support and professionalism of captains, crews, and ROV and AUV technical teams for the R/V *Western Flyer*, R/V *Zephyr*, R/V *Rachel Carson*, ROVs *Tiburon* and *Doc Ricketts*, and the Mapping AUVs, all from MBARI. Each dive program benefitted from the hard work of the entire scientific party who assisted with the dives and, at the end of long dive days, in describing, subsampling, and curating the samples recovered. A subset of glass compositions were determined at the microprobe laboratory at UC Davis by Nick Botto. We thank Jeff Alt and Damon Teagle for their assistance in locating and providing the ODP basalt sample from the bottom of hole 1038I on Central Hill and Bill Chadwick and Ken Rubin for helpful feedback on a draft of the manuscript. We thank Isobel Yeo and Ken Rubin for helpful reviews that clarified and improved the manuscript.

Appendix A. Supplementary data

Supplementary data to this article can be found online at https://doi.org/10.1016/j.jvolgeores.2022.107701.

References

Appelgate, B., Embley, R.W., 1992. Submarine tumuli and inflated tube-fed lava flows on Axial Volcano, Juan de Fuca Ridge. Bull. Volcanol. 54 (6), 447–458.

Beakawai Al-Hashemi, H.M., Baghabra Al-Amoudi, O.S., 2018. A review on the angle of repose of granular materials. Powder Technol. 330, 397–417.

Beresford, S.W., Cas, R.A.F., 2001. Komatiitic invasive lava flows, Kambalda, Western Australia. Can. Mineral. 39 (2), 525–535.

Berndt, C., 2005. Focused fluid flow in passive continental margins. Philos. Trans. R. Soc. A Math. Phys. Eng. Sci. 363 (1837), 2855–2871.

Bohlke, J.K., Shanks III, W.C., 1994. Stable isotope study of hydrothermal vents at Escanaba Trough: Observed and calculated effects of sediment-seawater interaction. In: Morton, J.L., Zierenberg, R.A., Reiss, C.A. (Eds.), Geologic, Hydrothermal, and Biologic Studies at Escanaba Trough, Gorda Ridge, Offshore Northern California. U. S. Geological Survey Bulletin, 2022, 253–239.

Brunner, C.A., Normark, W.R., Zuffa, G.G., Serra, F., 1999. Deep-sea sedimentary record of the late Wisconsin cataclysmic floods from the Columbia River. Geology 27, 463–466.

Bunger, A.P., Cruden, A.R., 2011. Modeling the growth of laccoliths and large mafic sills: role of magma body forces. J. Geophys. Res. 116, B02203. https://doi.org/10.1029/2010JB007648.

Byerly, G., Swanson, D.A., 1978. Invasive Columbia River basalt flows along the northwestern margin of the Columbia Plateau, north-central Washington. Geol. Soc. Am. Abstr. Programs 10 (3), 98.

Campbell, A.C., German, C.R., Palmer, M.R., Gamo, T., Edmond, J.M., 1994. Chemistry of hydrothermal fluids from the Escanaba Trough, Gorda Ridge. In: Morton, J.L., Zierenberg, R.A., Reiss, C.A. (Eds.), Geologic, Hydrothermal, and Biologic Studies at Escanaba Trough, Gorda Ridge, Offshore Northern California. U.S. Geological Survey Bulletin, 2022, pp. 201–221.

Caress, D.W., 2010. Some Comments on the Signal Processing used by Chirp Subbottom Profilers. In: http://www3.mbari.org/products/mbsystem/sonarfunction/SubbottomProcessing/subbottomdataprocessing.html.

Caress, D.W., Chayes, D.N., 2011. MB-System: Open-Source Software for the Processing and Display of Swath Mapping Sonar Data. Lamont-Doherty Earth Observatory of Columbia University, Palisades, NY. Retrieved from. http://www.mbari.org/products/research-software/mbsystem/.

Caress, D.W., Clague, D.A., Paduan, J.B., Martin, J.F., Dreyer, B.M., Chadwick Jr., W.W., Denny, A., Kelley, D.S., 2012. Repeat bathymetric surveys at 1-metre resolution of lava flows erupted at Axial Seamount in April 2011. Nat. Geo. 5 (7), 483–488. https://doi.org/10.1038/NGEO1496.

Caress, D.W., Thomas, H., Kirkwood, W.J., McEwen, R., Henthorn, R., Clague, D.A., Paull, C.K., Paduan, J.B., Maier, K.L., 2008. High-resolution multibeam, sidescan, and subbottom surveys using the MBARI AUV D. In: Allan, B., Reynolds, J.R., Greene, H.G. (Eds.), Marine Habitat Mapping Technology for Alaska. University of Alaska Fairbanks, Fairbanks, pp. 47–70. https://doi.org/10.4027/mhmta.2008.04.

Cathles, L.M., Su, Z., Chen, D., 2010. The physics of gas chimney and pockmark formation, with implications for assessment of seafloor hazards and gas sequestration. Mar. Pet. Geol. 27, 82–91.

Chadwick Jr., W.W., Clague, D.A., Embley, R.W., Perfit, M.R., Butterfield, D.A., Caress, D.W., Paduan, J.B., Martin, J.F., Sasnett, P., Merle, S.G., Bobbitt, A.M., 2013. The 1998 eruption of Axial Seamount: New insights on submarine lava flow emplacement from high-resolution mapping. Geochem. Geophys. Geosyst. https://doi.org/10.1002/ggge.20202.

Chadwick Jr., W.W., Embley, R.W., Shanks, T.M., 1998. The 1996 Gorda Ridge eruption: geologic mapping, sidescan sonar, and SeaBeam comparison results. Deep-Sea Res. II 45, 2547–2569. https://doi.org/10.1016/s0967-0645(98)00083-6.

Chadwick, J., Perfit, M., Ridley, I., Jonasson, I., Kamenoc, G., Chadwick, W., Embley, R., le Roux, P., Smith, M., 2005. Magmatic effects of the Cobb hot spot on the Juan de Fuca Ridge. J. Geophys. Res. 110 (B03101), 1–16.

Chadwick, J., Keller, R., Kamenow, G., Yogodzinski, G., Lupton, J., 2014. The Cobb hot-spot DMM-HIMU mixing and melting controlled by a progressively thinning lithosphere lid. Geochem. Geophys. Geosyst. 15, 3107–3122.

Chadwick, W.W., Rubin, K.H., Merle, S.G., Bobbitt, A.M., Kwasnitschka, T., Embley, R. W., 2019. Recent eruptions between 2012 and 2018 discovered at West Mata Submarine Volcano (NE Lau Basin, SW Pacific) and characterized by new ship, AUV, and ROV data. Front. Mar. Sci. 6 https://doi.org/10.3389/fmars.2019.00495 article 495, pp25.

Clague, D.A., Holmes, M.L., 1987. Geology, petrology, and mineral potential of the Gorda Ridge. In: Scholl, D.W., Grantz, A., Vedder, J.G. (Eds.), Geology and Resource Potential of the Continental Margin of Western North America and Adjacent Ocean Basins—Beaufort Sea to Baja California, Circum-Pacific Council for Energy and Mineral Resources, Earth Science Series, 6, pp. 563–580. Houston.

Clague, D.A., Moore, J.G., Reynolds, J.R., 2000a. Formation of submarine flat-topped volcanic cones in Hawaii. Bull. Volcanol. 62, 214–233.

Clague, D.A., Reynolds, J.R., Davis, A.S., 2000b. Near-ridge seamount chains in the northeastern Pacific Ocean. J. Geophys. Res. 105, 16,541–16,561.

Clague, D.A., Zierenberg, R.A., Davis, A.S., Goffredi, S.K., McClain, J.S., Maher, N.A., Olson, E.J., Orphan, V.J., Ross, S.L., Von Damm, K.L., 2001. MBARI's 2000 expedition to the Gorda Ridge. Ridge Events 11, 5–12.

Clague, D.A., Davis, A.S., Dixon, J.E., 2003. Submarine strombolian eruptions on the Gorda Mid-Ocean Ridge. In: White, J.D.L., Smellie, J.L., Clague, D.A. (Eds.), Explosive Subaqueous Volcanism, Geophysical Monograph, 140. American Geophysical Union, pp. 111–128.

Clague, D.A., Paduan, J.B., Davis, A.S., 2009. Widespread strombolian eruptions of mid-ocean ridge basalt. J. Volcanol. Geotherm. Res. 180, 171–188.

Clague, D.A., Dreyer, B.M., Paduan, J.B., Martin, J.F., Chadwick Jr., W.W., Caress, D.W., Portner, R.A., Guilderson, T.P., McGann, M.L., Butterfield, D.A., Thomas, H., Embley, R.W., 2013. Geologic history of the summit of Axial Seamount, Juan de Fuca Ridge. Geochem. Geophys. Geosyst. https://doi.org/10.1002/ggge.20240.

Clague, D.A., Dreyer, B.M., Paduan, J.B., Martin, J.F., Caress, D.W., Gill, J.B., Kelley, D. S., Thomas, H., Portner, R.A., Guilderson, T.P., McGann, M.L., 2014. Eruptive and tectonic history of the Endeavour segment of the Juan de Fuca Ridge based on AUV mapping and lava flow ages. Geochem. Geophys. Geosyst. 15 https://doi.org/10.1002/2014GC005415, 1-28.

Clague, D.A., Paduan, J.B., Caress, D.W., Chadwick Jr., W.W., Le Saout, M., Dreyer, B., Portner, R.A., 2017. High-resolution AUV mapping and targeted ROV observations of three historical lava flows at Axial Seamount. Oceanography 30 (4), 82–99. https://doi.org/10.5670/oceanog.2017.426.

Clague, D.A., Caress, D.W., Dreyer, B.M., Lundsten, L., Paduan, J.B., Portner, R.A., Spelz-Madero, R., Bowles, J.A., Castillo, P.R., Guardado-France, R., Le Saout, M., Martin, J. F., Santa Rosa-del Río, M.A., Zierenberg, R.A., 2018. Geology of the Alarcon Rise. Geochem. Geophys. Geosyst. 19 https://doi.org/10.1002/2017GC007348.

Clague, D.A., Paduan, J.B., Caress, D.W., McClain, J., Zierenberg, R., 2020. Lava flows erupted in 1996 on North Gorda Ridge Segment and the geology of the nearby Sea Cliff hydrothermal vent field from 1-m resolution AUV mapping. Front. Earth Sci. https://doi.org/10.3389/fmars.2020.00027.

Clague, D.A., Caress, D.W., Paduan, J.B., 2021. Escanaba Trough, Gorda Ridge: AUV Mapping Missions 20140823m1, 20140824m1, 20140825m1, 20140826m1, 20160809m1, 20160809m2, 20160810m1, and 20160810m2 in the Northern, Middle and Southern Escanaba Trough (NESCA, MESCA and SESCA), MGDS. https://www.marine-geo.org/tools/search/entry.php?id=EscanabaTrough_MBARI.

Corry, C.E., 1988. Laccoliths: mechanics of emplacement and growth. Geol. Soc. Am. Spec. Pap. 200, 110 pp.

Cousens, B.L., 1996. Depleted and enriched upper mantle sources for basaltic rocks from diverse tectonic environments in the northeast Pacific Ocean: the generation of oceanic alkaline vs. tholeiitic basalts. In: Basu, A., Hart, S. (Eds.), Earth Processes: Reading the Isotopic Code, American Geophysical Union, Geophysical Monograph, 95, pp. 207–231.

Cousens, B.L., Chase, R.L., Schilling, J.-G., 1984. Basaltic geochemistry of the Explorer Ridge area, northeast Pacific Ocean. Can. J. Earth Sci. 21, 157–170.

Cousens, B.L., Allen, J.F., Leybourne, M.I., Chase, R.L., von Wagoner, N., 1995. Mixing of magmas from enriched and depleted mantle sources in the northeast Pacific: West Valley segment, Juan de Fuca Ridge. Contrib. Mineral. Petrol. 120, 337–357.

Cousens, B.L., Blenkinsop, J., Franklin, J.M., 2002. Lead isotope systematics of sulfide minerals in the Middle Valley hydrothermal system, northern Juan de Fuca. Geochem. Geophys. Geosyst. 3, 1–16. https://doi.org/10.1029/2001GC000257.

Cousens, B.L., Weis, D., Constantin, M., Scott, S., 2017. Radiogenic isotopes in enriched mid-ocean ridge basalts from the Explorer Ridge, northeast Pacific Ocean. Geochem. Cosmochem. Acta 213, 63–90. https://doi.org/10.1016/j.gca.2017.06.032.

Currier, R.M., Forsythe, P., Grossmeier, C., Laliberte, M., Yagle, B., 2017. Experiments on the evolution of laccolith morphology in plan-view. J. Volcanol. Geotherm. Res. 336, 155–167.

Davis, A.S., Clague, D.A., 1987. Geochemistry, mineralogy, and petrogenesis of lava from the Gorda Ridge between latitude 43°N and 41.4°N. J. Geophys. Res. 92, 10,467–10,483.

Davis, A.S., Clague, D.A., 2003. Got glass? Glass from sediment and foraminifera tests contribute clues to volcanic history. Geology 31, 103–106.

Davis, A.S., Clague, D.A., Friesen, W.B., 1994. Petrology and mineral chemistry of basalt from Escanaba Trough. In: Morton, J.L., Zierenberg, R.A., Reiss, C.A. (Eds.), Geologic, Hydrothermal, and Biologic Studies at Escanaba Trough, Gorda Ridge, Offshore Northern California. U.S. Geological Survey Bulletin, 2022, pp. 153–170.

Davis, A.S., Clague, D.A., White, W.M., 1998. Geochemistry of basalt from Escanaba Trough: evidence for sediment contamination. J. Petrol. 39, 841–858.

Denlinger, R.P., Holmes, M.L., 1994. A thermal and mechanical model for sediment hills and associated sulfide deposits along the Escanaba Trough. In: Morton, J.L., Zierenberg, R.A., Reiss, C.A. (Eds.), Geologic, Hydrothermal, and Biologic Studies at Escanaba Trough, Gorda Ridge, Offshore Northern California. U.S. Geological Survey Bulletin, 2022, pp. 65–75.

Duffield, W.A., Bacon, C.R., Delaney, P.T., 1986. Deformation of poorly consolidated sediment during emplacement of a mafic sill, Coso Range, California. Bull. Volcanol. 48, 97–107.

Dziak, R.P., Fox, C.G., Bobbitt, A., Goldfinger, C., 2002. Bathymetric map of the Gorda Plate: structural and geomorphological processes inferred from multibeam surveys. Mar. Geophys. Res. 22, 235–250.

Einsele, G., Gieskes, J.M., Curray, J., Moore, D.M., Aguayo, E., Aubrey, M.-P., Fornari, D. J., Guerrero, J., Kastner, M., Kelts, K., Lyle, M., Matoba, Y., Molina-Cruz, A., Niemitz, J., Rueda, J., Saunders, A., Schrader, H., Simoneit, B., Vacquier, V., 1980. Intrusion of basaltic sills into highly porous sediments and resulting hydrothermal activity. Nature 283, 441–445.

Elliot, D.H., Fleming, T.H., 2018. The Ferrar Large Igneous Province: Field and geochemical constraints on supra-crustal (high-level) emplacement of the magmatic system. In: Sensarma, S., Storey, B.C. (Eds.), Large Igneous Provinces from Gondwana and Adjacent Regions, Geological Society of London, Special Publications, 463, pp. 41–58.

Fouquet, Y., Zierenberg, R.A., Miller, D.J., et al., 1998a. Introduction: Investigation of hydrothermal circulation and genesis of massive sulfide deposits at sediment-covered spreading centers at Middle Valley and Escanaba Trough. In: Proceedings of the Ocean Drilling Program, Initial Reports, 169. Ocean Drilling Program, College Station, Texas, 5927–16.

Fouquet, Y., Zierenberg, R.A., Miller, D.J., et al., 1998b. Escanaba Trough: Central Hill (site 1038). In: Proceedings of the Ocean Drilling Program, Initial Reports, 169. Ocean Drilling Program, College Station, Texas, pp. 253–298.

Fouquet, Y., Zierenberg, R.A., Miller, D.J., et al., 1998c. Escanaba Trough: Reference Site (site 1037). In: Proceedings of the Ocean Drilling Program, Initial Reports, 169. Ocean Drilling Program, College Station, Texas, pp. 205–251.

Galland, O., 2012. Experimental modeling of ground deformation associated with shallow magma intrusions. Earth Planet. Sci. Lett. 317, 145–156. https://doi.org/10.1016/j.epsl.2011.10.017.

Galland, O., Bertelsen, H.S., Eide, C.H., Guldtrand, F., Haug, O.T., Leanza, H.A., Mair, K., Palma, O., Planke, S., Rabbel, O., Rogers, B., Schmiedel, T., Souche, A., Spacapan, J. B., 2018. Storage and transport of magma in the layered crust—Formation of sills and related flat-lying intrusions. In: Burchardt, S. (Ed.), Volcanic and Igneous Plumbing Systems. Elsevier, pp. 111–136.

Garcon, M., Boyet, M., Carlson, R.W., Horan, M.F., Auclair, D., Mock, T.D., 2018. Factors influencing the precision and accuracy of Nd isotope measurements by thermal ionization mass spectrometry. Chem. Geol. 476, 493–514. https://doi.org/10.1016/j.chemgeo.2017.12.003.

Gill, J., Michael, P., Woodcock, W., Dreyer, B., Ramos, F., Clague, D., Kela, J., Scott, S., Konrad, K., Stakes, D., 2016. Spatial and temporal scale of mantle enrichment at the Endeavour Segment, Juan de Fuca Ridge. J. Petrol. 1-33 https://doi.org/10.1093/petrology/egw024.

Graham, D.W., Blichert-Toft, J., Russo, C.J., Rubin, K.H., Albarede, F., 2006. Cryptic striations in the upper mantle revealed by Hf isotopes in southeast Indian ridge basalts. Nature 440 (9), 199–202. https://doi.org/10.1038/nature 04582.

Henkart, P., 2006. Chirp sub-bottom profiler processing—A review: Chirp signals may be recorded as correlates, analytic, or envelope. In: Sea Technology, October 2006, pp. 35–38.

Hon, K., Kauahikaua, J., Denlinger, R., Mackay, K., 1994. Emplacement and inflation of pahoehoe sheet flows: observations and measurements of active lava flows on Kilauea Volcano, Hawaii. Geol. Soc. Am. Bull. 106, 351–370.

Hovland, M., Judd, A.G., King, L.H., 1984. Characteristic features of pockmarks on the North Sea Floor and Scotian Shelf. Sedimentology 31, 47–480.

Hunt, C.B., 1953. Geology and geography of the Henry Mountains Region, Utah. U.S. Geol. Surv. Prof. Pap. 228, 234 pp.

Ishibashi, J.-I., Sato, M., Sano, Y., Wakita, H., Gamo, T., Shanks III, W.C., 2002. Helium and carbon rich gas geochemistry of pore fluids from the sediment-rich hydrothermal system in Escanaba Trough. Appl. Geochem. 17, 1457–1466.

James, R.H., Rudnicki, M.D., Palmer, M.R., 1999. The alkali element and boron geochemistry of the Escanaba Trough sediment hosted sulfide system. Earth Planet. Sci. Lett. 171, 157169.

Janecky, D.R., Seyfried, W.E., 1984. Formation of massive sulfide deposits at oceanic ridge crests: incremental reaction models for mixing between hydrothermal solutions and seawater. Geochim. Cosmochim. Acta 48, 2723–2738.

Judd, A., Hovland, M., 2007. Seabed Fluid Flow: The Impact on Geology, Biology, and the Marine Environment. Cambridge University Press, Cambridge, UK.

Karaket, A., Chenrai, P., Huuse, M., 2021. Seismic characteristics of paleopockmarks in the Great South Basin, New Zealand. Front. Earth Sci. 9 https://doi.org/10.3389/feart.2021.683617.

Karlin, R.E., Zierenberg, R.A., 1994. Sedimentation and neotectonism in the SESCA area, Escanaba Trough, southern Gorda Ridge. In: Morton, J.L., Zierenberg, R.A., Reiss, C. A. (Eds.), Geologic, Hydrothermal, and Biologic Studies at Escanaba Trough, Gorda Ridge, Offshore Northern California. U.S. Geological Survey Bulletin, 2022, pp. 131–141.

Karsten, J.L., Delaney, J., Rhodes, J.M., Lias, R.A., 1990. Spatial and temporal evolution of magmatic systems beneath the Endeavour Segment, Juan de Fuca Ridge: tectonic and petrologic constraints. J. Geophys. Res. 95, 19235–19256.

Kavanagh, J.L., Menand, T., Sparks, R.S.J., 2006. An experimental investigation of sill formation and propagation in layered elastic media. Earth Planet. Sci. Lett. 245, 799–813.

Kelley, J.T., Dickson, S.M., Belknap, D.F., Barnhardt, W.A., Henderson, M., 2010. Giant Sea-bed pockmarks: evidence for gas escape from Belfast Bay, Maine. Geology 22, 59–62.

King, L.H., MacLean, B., 1970. Pockmarks on Scotian Shelf. Geol. Soc. Am. Bull. 81, 3141–3148.

Koch, F.G., Johnson, A.M., Pollard, D.D., 1982. Monoclinal bending of strata over laccolithic intrusions. Tectonophysics 74, T21–T31.

Koski, R.A., Benninger, L.M., Zierenberg, R.A., Jonasson, I.R., 1994. Composition and growth history of hydrothermal deposits in Escanaba Trough, southern Gorda Ridge. In: Morton, J.L., Zierenberg, R.A., Reiss, C.A. (Eds.), Geologic, Hydrothermal, and Biologic Studies at Escanaba Trough, Gorda Ridge, Offshore Northern California. U. S. Geological Survey Bulletin, 2022, pp. 293–324.

Kvenvolden, K.A., Rapp, J.B., Hostettler, F.D., 1994. Hydrocarbons in sediment from Escanaba Trough. In: Morton, J.L., Zierenberg, R.A., Reiss, C.A. (Eds.), Geologic, Hydrothermal, and Biologic Studies at Escanaba Trough, Gorda Ridge, Offshore Northern California. U.S. Geological Survey Bulletin, 2022, pp. 279–292.

Leaman, D.E., 1975. Form, mechanism, and control of dolerite intrusions near Hobart, Tasmania. J. Geol. Soc. Aust. 22 (2), 175–186. https://doi.org/10.1080/00167617508728886.

Leaman, D.E., 1995. Mechanics of sill emplacement: comments based on Tasmanian dolerites. Aust. J. Earth Sci. 42 (2), 151–155. https://doi.org/10.1080/08120099508728188.

Lonsdale, P., Lawver, L.A., 1980. Immature plate boundary zones studied with a submersible in the Gulf of California. Geol. Soc. Am. Bull. 91, 555–569.

Magee, C., Bastow, I.D., van Wyk de Vries, B., Jackson, C.A.-L., Hetherington, R., Hagos, M., Hoggett, M., 2017. Structure and dynamics of surface uplift induced by incremental sill emplacement. Geology 45, 431–434. https://doi.org/10.1130/G38839.1.

Magenheim, A.J., Geiskes, J.M., 1994. Evidence for hydrothermal fluid flow through surficial sediments, Escanaba Trough. In: Morton, J.L., Zierenberg, R.A., Reiss, C.A. (Eds.), Geologic, Hydrothermal, and Biologic Studies at Escanaba Trough, Gorda Ridge, Offshore Northern California. U.S. Geological Survey Bulletin, 2022, pp. 241–255.

MBARI Mapping Team, 2001. Seamounts and Ridges Multibeam Survey, Monterey Bay Aquarium Research Institute Digital Data Series No. 7, 1-CD.

Michael, P.J., Chase, R.L., Allen, J.J., 1989. Petrologic and geologic variations along the Southern Explorer Ridge, northeast Pacific Ocean. J. Geophys. Res. 94, 13895–13918.

Morton, J.L., Fox, C.G., 1994. Structural setting and interaction of volcanism and sedimentation at Escanaba Trough – Geophysical results. In: Morton, J.L., Zierenberg, R.A., Reiss, C.A. (Eds.), Geologic, Hydrothermal, and Biologic Studies at Escanaba Trough, Gorda Ridge, Offshore Northern California. U.S. Geological Survey Bulletin, 2022, pp. 21–43.

Morton, J.L., Zierenberg, R.A., Reiss, C.A., 1994. Geologic, hydrothermal, and biologic studies at Escanaba Trough – An introduction. In: Morton, J.L., Zierenberg, R.A., Reiss, C.A. (Eds.), Geologic, Hydrothermal, and Biologic Studies at Escanaba Trough, Gorda Ridge, Offshore Northern California. U.S. Geological Survey Bulletin, 2022, pp. 1–18.

Murch, A.P., Portner, R.A., Rubin, K.H., Clague, D.A., 2022. Deep subaqueous implosive volcanism at West Mata seamount, Tonga. Earth Planet. Sci. Lett. 578 https://doi.org/10.1016/j.epsl.2021.117328.

Nelson, H., Thor, D.R., Sandstrom, M.W., Kvenvolden, K.A., 1979. Modern biogenic gas-generated craters (sea-floor pockmarks) on the Bering Shelf, Alaska. Geol. Soc. Am. Bull. 90, 1344–1352.

Normark, W.R., Serra, F., 2001. Vertical tectonics in northern Escanaba Trough as recorded by thick late Quaternary turbidites. J. Geophys. Res. 106, 13,793–13,802.

Normark, W.R., Gutmacher, C.E., Zierenberg, R.A., Wong, F.L., Rosenbauer, R.J., 1994. Sediment fill of Escanaba Troughc. In: Morton, J.L., Zierenberg, R.A., Reiss, C.A. (Eds.), Geologic, Hydrothermal, and Biologic Studies at Escanaba Trough, Gorda Ridge, Offshore Northern California. U.S. Geological Survey Bulletin, 2022, pp. 91–129.

Ondréas, H., Scalabrin, C., Fouquet, Y., Godfry, A., 2018. Recent high-resolution mapping of Guaymas hydrothermal fields (Southern Trough). BSGF-Earth Sci. Bull. 189, 6. https://doi.org/10.1051/bsgf/2018005.

Paduan, J.B., Zierenberg, R.A., Clague, D.A., Caress, D.W., Thomas, H., Troni, G., Lundsten, L., Martin, J.F., Wheat, G., Lilley, M., Lupton, J., Spelz-Madero, R., Neuman, F., Santa Rosa-del Rio, M., 2018. Hydrothermal vent fields on Alarcon Rise and in the southern Pescadero Basin, southern Gulf of California. Geochem. Geophys. Geosyst. 19 (12) https://doi.org/10.1029/2018GC007771.

Paull, C.K., Caress, D.W., Thomas, H., Lundsten, E., Anderson, K., Gwiazda, R., Reidel, M., McGann, M., Herguerra, J.C., 2015. Seafloor geomorphic manifestations of gas venting and shallow subbottom gas hydrate occurrences. Geosphere 11, 491–513. https://doi.org/10.1130/GES01012.1.

Pegler, S.S., Ferguson, D.J., 2021. Rapid heat discharge during deep-sea eruptions generates megaplumes and disperses tephra. Nat. Commun. 12, 2292. https://doi.org/10.1038/s41467-021-22439-y.

Pollard, D.D., Muller, O.H., Duckstader, D.R., 1975. Form and growth of fingered sheet intrusions. Geol. Soc. Am. Bull. 86, 351–363.

Richard, P., Shimizu, N., Allègre, J.C., 1976. $^{143}Nd/^{146}Nd$, a natural tracer: an application to oceanic basalts. Earth Planet. Sci. Lett. 31, 269–278.

Ross, S.L., Zierenberg, R.A., 1994. Volcanic geomorphology of the SESCA and NESCA sites, Escanaba Trough. In: Morton, J.L., Zierenberg, R.A., Reiss, C.A. (Eds.), Geologic, Hydrothermal, and Biologic Studies at Escanaba Trough, Gorda Ridge, Offshore Northern California. U.S. Geological Survey Bulletin, 2022, pp. 143–151.

Ross, S.L., Zierenberg, R.A., 2009. Sidescan Sonar Imagery of the Escanaba Trough, Southern Gorda Ridge, Offshore Northern California. U.S. Geological Survey, Scientific Investigations Map 2907.

Rubin, K.H., 1997. Degassing of metals and metalloids from erupting seamount and Mid-Ocean Ridge volcanoes: Observations and predictions. Geochim. Cosmochim. Acta 61, 3525–3542.

Rubin, K.H., Smith, M.C., Perfit, M.R., Christie, D.M., Sacks, L.F., 1998. Geochronology and geochemistry of lavas from the 1996 north Gorda Ridge eruption. Deep-Sea Res. II 45, 2571–2597. https://doi.org/10.1016/s0967-0645(98)00084-8.

Rubin, K.H., Smith, M.C., Bergmanis, E.C., Perfit, M.R., Sinton, J.M., Batiza, R., 2001. Geochemical heterogeneity within mid-ocean ridge lava flows: insights into eruption, emplacement and global variations in magma generation. Earth Planet. Sci. Lett. 188, 349–367. https://doi.org/10.1016/s0012-821x(01) 00339-9.

Scheibert, J., Galland, O., Hafner, A., 2017. Inelastic deformation during sill and laccolith emplacement: insights from an analytic elasto-plastic model. J. Geophys. Res. 122, 923–945. https://doi.org/10.1002/2016JB013754.

Schmiedel, T., Galland, O., Breitkreutz, C., 2017a. Dynamics of sill and laccolith emplacement in the brittle crust: role of host rock strength and deformation mode. J. Geophys. Res. 122, 8860–8871. https://doi.org/10.1002/2017JB014468.

Schmiedel, T., Kjoberg, S., Planke, S., Magee, C., Galland, O., Schofield, N., Jackson, C. A.-L., Jerram, D.A., 2017b. Mechanisms of overburden deformation associated with the emplacement of the Tulipan sill, mid-Norwegian margin. Interpretation 5 (3), SK23–SK38. Society of Exploration Geophysicists and American Association of Petroleum Geologists. https://doi.org/10.1190/INT-2016-0155.1.

Schofield, N., Stevenson, C., Reston, T., 2010. Magma fingers and host rock fluidization in the emplacement of sills. Geology 38. https://doi.org/10.1130/G30142.1.

Seymour, D.B., Green, G.R., Calver, C.R., 2007. The geology and mineral deposits of Tasmania: A summary. In: Tasmanian Geological Survey Bulletin, 72, Mineral Resources Tasmania ISBN 0–7246–4017-7.

Stakes, D.S., Perfit, M.R., Tivey, M.A., Caress, D.W., Ramirez, T.M., Maher, N., 2006. The Cleft revealed: geologic, magnetic, and morphologic evidence for construction of upper oceanic crust, southern Juan de Fuca Ridge. Geochem. Geophys. Geosyst. 7 https://doi.org/10.1029/2005GC001038.

Stracke, A., Hofmann, A.W., Hart, S.R., 2005. FOZO, HIMU, and the rest of the mantle zoo. Geochem. Geophys. Geosyst. 6 https://doi.org/10.1029/2004GC000824.

Teske, A., McKay, L.J., Ravelo, A.C., Aiello, I., Mortera, C., Nunez-Useche, F., Canet, C., Chanton, J.P., Brunner, B., Hensen, C., Ramirez, G.A., Sibert, R.J., Turner, T., White, D., Chambers, C.R., Buckley, A., Joye, S.B., Soule, S.A., Lizarralde, D., 2019. Characteristics and evolution of sill-driven off-axis hydrothermalism in Guaymas Basin - the Ringvent site. Nat. Sci. Rep. 9, 13847. https://doi.org/10.1038/s41598-019-50200-5.

Teske, A., Lizarralde, D., Höfig, T.W., Expedition 385 Scientists, 2020. Expedition 385 Preliminary Report: Guaymas Basin Tectonics and Biosphere. International Ocean Discovery Program. https://doi.org/10.14379/iodp.pr.385.2020.

Teske, A., Wegener, G., Chanton, J.P., White, D., MacGregor, B., Hoer, D., de Beer, D., Zhuang, G., Sexton, M.A., Joye, S.B., Lizarralde, D., Soule, S.A., Ruff, S.E., 2021. Microbial communities under distinct thermal and geochemical regimes in axial and off-axis sediments of Guaymas Basin. Front. Microbiol. 12 www.frontiersin.org. Article 633649.

Thomson, K., 2007. Determining magma flow in sills, dykes, and laccoliths and their implication for sill emplacement mechanisms. Bull. Volcanol. 70, 183–201. https://doi.org/10.1007/s00445-007-0131-8.

Thomson, K., Schofield, N., 2008. Lithological and structural controls on the emplacement and morphology of sills in sedimentary basins. Geol. Soc. Lond. Spec. Publ. 302, 31–44. https://doi.org/10.1144/SP302.3.

Tishchenko, P., Hensen, C., Wallmann, K., Wong, C.S., 2005. Calculation of the stability and solubility of methane hydrate in seawater. Chem. Geol. 219, 37–52.

Todt, W., Cliff, R.A., Hanser, A., Hofmann, A.W., 1996. Evaluation of a ^{202}Pb-^{205}Pb double spike for high-precision lead isotope analysis. In: Basu, A., Hart, S.R. (Eds.), Earth Processes: Reading the Isotopic Code, Geophysical Monograph 95. American Geophysical Union, Washington, DC, pp. 429–437.

Vallier, T.L., Harold, P.J., Gerdley, W.A., 1973. Provenance and dispersal patterns of turbidite sand in Escanaba Trough, northeastern Pacific Ocean. Mar. Geol. 15, 67–87.

Vogt, P.R., Crane, K., Sundvor, W., Max, M.D., Pfirman, S.L., 1984. Methane-generated (?) pockmarks on young, thickly sedimented ocean crust in the Arctic: Vestnesa Ridgem Fram strait. Geology 22, 255–258.

Von Damm, K.L., Parker, C.M., Zierenberg, R.A., Lilley, M.D., Olsen, E.J., Clague, D.A., McClain, J.S., 2005. The Escanaba trough, Gorda Ridge hydrothermal system: temporal stability and seafloor complexity. Geochem. Cosmochem. Acta 69, 4971–4984.

Von Wagoner, N.A., Leybourne, M.I., 1991. Evidence for magma mixing and a heterogeneous mantle on the West Valley Segment of the Juan de Fuca Ridge. J. Geophys. Res. 96, 16295–16318.

Wallmann, K., Pinero, E., Burwicz, E., Haeckel, M., Hensenn, A.D., Rupke, L., 2012. The global inventory of methane hydrate in marine sediment: a theoretical approach. Energies 5, 2449–2498. https://doi.org/10.3390/en5072449.

Weis, D., Kieffer, B., Maerschalk, C., Barling, J., de Jong, J., Williams, G.A., Hanano, D., Pretorius, W., Mattielli, N., Scoates, J.S., Goolaerts, A., Friedman, R.M., Mahoney, J. B., 2006. High-precision isotopic characterization of USGS reference materials by TIMS and MC-ICP-MS. Geochem. Geophys. Geosyst. 7 (8), Q08006. https://doi.org/10.1029/2006GC001283.

Wilson, D.S., 1989. Deformation of the so-called Gorda plate. J. Geophys. Res. 94, 3065–3075.

Wilson, P.I.R., McCaffrey, K.J.W., Wilson, R.W., Jarvis, I., Holdsworth, R.E., 2016. Deformation structures associated with the Trachyte Mesa intrusion, Henry Mountains, Utah: implications for sill and laccolith emplacement mechanisms. J. Struct. Geol. 87, 30–46. https://doi.org/10.1016/j.jsg.2016.04.001.

Yeo, I.A., Clague, D.A., Martin, J.F., Paduan, J.P., Caress, D.W., 2013. Pre-eruptive flow focusing in dikes feeding historic pillow ridges on and Juan de Fuca and Gorda Ridges. Geochem. Geophys. Geosyst. 14 (9), 3586–3599. https://doi.org/10.1002/ggge.20210.

Zierenberg, R.A., Miller, D.J., 2000. Overview of Ocean Drilling Program Leg 169 – Sedimented Ridges II. In: Zierenberg, R.A., Fouquet, Y., Miller, D.J. (Eds.), Proceedings of the Ocean Drilling Program, Scientific Results Volume 169, pp. 1–39.

Zierenberg, R.A., Shanks III, W.C., 1994. Sediment alteration associated with massive sulfide formation in Escanaba Trough, Gorda Ridge: The importance of seawater mixing and magnesium metasomatism. In: Morton, J.L., Zierenberg, R.A., Reiss, C.A. (Eds.), Geologic, Hydrothermal, and Biologic Studies at Escanaba Trough, Gorda Ridge, Offshore Northern California. U.S. Geological Survey Bulletin, 2022, pp. 257–277.

Zierenberg, R.A., Koski, R.A., Morton, J.L., Bouse, R.M., Shanks III, W.C., 1993. Genesis of massive sulfide deposits on a sediment-covered spreading center, Escanaba Trough, 41° N, Gorda Ridge. Econ. Geol. 88, 2069–2098.

Zierenberg, R.A., Morton, J.L., Koski, R.A., Ross, S.L., 1994. Geologic setting of massive sulfide mineralization in the Escanaba Trough. In: Morton, J.L., Zierenberg, R.A., Reiss, C.A. (Eds.), Geologic, Hydrothermal, and Biologic Studies at Escanaba Trough, Gorda Ridge, Offshore Northern California. U.S. Geological Survey Bulletin, 2022, pp. 171–197.

Zierenberg, R.A., Fouquet, Y., Miller, D.J., et al., 1998. The deep structure of a sea-floor hydrothermal deposit. Nature 392, 485–488.

Zierenberg, R.A., Fouquet, Y., Miller, D.J., Normark, W.R. (Eds.), 2000. Proceedings of the Ocean Drilling Program, ODP Scientific Results, 169. Texas A&M University, College Station, Tex, 169, [CD-ROM].

Zuffa, G.G., De Rosa, R., Normark, W.R., 1997. Shifting sources and transport paths for the late Quaternary Escanaba Trough sediment fill (northeast Pacific). Giorn. Geol. 59, 35–53.

Zuffa, G.G., Normark, W.R., Serra, F., Brunner, C.A., 2000. Turbidite megabeds in an oceanic rift valley recording jökulhlaups of late Pleistocene glacial lakes of the Western United States. J. Geol. 108, 253–274.